TENSEGRITY-INSPIRED NANOCOMPOSITE STRUCTURES

A Dissertation
Presented to
The Academic Faculty

by

Ji Hoon Lee

In Partial Fulfillment
of the Requirements for the Degree
Doctor of Philosophy in the
School of Materials Science and Engineering

Georgia Institute of Technology
August 2012

TENSEGRITY-INSPIRED NANOCOMPOSITE STRUCTURES

Approved by:

Dr. Meisha L. Shofner, Advisor
School of Materials Science and Engineering
Georgia Institute of Technology

Dr. Yonathan Thio
School of Materials Science and Engineering
Georgia Institute of Technology

Dr. Anselm Griffin
School of Materials Science and Engineering
Georgia Institute of Technology

Dr. Donggang Yao
School of Materials Science and Engineering
Georgia Institute of Technology

Dr. J. Carson Meredith
School of Chemical and Biomolecular Engineering
Georgia Institute of Technology

Date Approved: June 27, 2012

ACKNOWLEDGEMENTS

I would like to thank my advisor Dr. Meisha L. Shofner for her support, encouragement, and recommendations during my research. Her encouragement always gives me motivation to move forward. I would like to thank Dr. Anselm Griffin, Dr. J. Carson Meredith, Dr. Yonathan Thio, and Dr. Donggang Yao for taking the time to serve as my thesis committee members and their precious suggestions.

I would like to acknowledge my former group member Dr. Jasmeet Kaur for her help and invaluable discussion. I am sincerely thankful to Dr. Il Tae Kim for helping in the analysis of X-ray diffraction. I would also like to thank my current group members Stephanie Lin, Cait Meree, and Prateek Verma for their help. I would also like to thank my former group members Dr. Michelle Schlea, Dr. Tracy Brown, Bradley Johnson and Jae Ik Choi.

Lastly, but certainly not least, I thank my family for their support and encouragement. I am greatly appreciative to my wife Yunkyung Oh and my baby Seohyun for their patience, understanding and love.

TABLE OF CONTENTS

LIST OF TABLES

LIST OF FIGURES

Page

SUMMARY

The main goal of this research is to construct hierarchical microstructures from polymer nanocomposites. Specifically, the research focused on constructing tensegrity-inspired microstructure where the nanoparticles are the compression members and the polymer matrix is tensile web. In order to achieve the tensegrity-inpired microstruture, the research was conducted with the following objectives.

1. Synthesis of Hydroxyapatite (HAp) nanoparticles of controlled shapes using block copolymer templates.
2. Investigation of the effects of particle loadings and shapes on isotropic nanocomposite properties.
3. Construction of HAp building blocks into the tensegrity-inspired microstructures

First, in order to use the nanoparticles for this structure, needle-shaped HAp nanoparticles were synthesized using block copolymer templates. The results indicated that significant amount of polymer remained on particle surface. Since these particles were coated with polymer blocks, the decorated polymer blocks were considered as the interphase material which would be used to prestress the HAp nanoparticles, and the particles would be acted as the building blocks for constructing tensegrity-inspired microstructure. For nanocomposites, polymer coating on HAp nanoparticles promoted particle dispersion. The effect of particle shapes on thermomechanical properties did not show significant differences between the two particle systems due to their low aspect ratios and chemical similarity. However, the polymer crystallinity and crystallization

showed different trend as a function of particle loadings in two particle systems, and the behavior was unified through a common particle spacing of approximately 120 nm. In order to investigate the effect of particle arrangement in the polymer matrix, needle-shaped HAp nanoparticles synthesized with two different block copolymers were mixed with different morphology of polymer matrices and manipulated particle arrangement using the drawing process. Nanocomposites prepared with different matrix morphologies showed the similar dispersion characteristics and reinforcement behavior. The experimental results showed the drawing process influenced the particle arrangement in the polymer matrix, and the particle arrangement and reinforcement behavior were influenced by polymer matrix morphology. The thermomechanical properties of both matrix systems enhanced through the drawing process in the glassy region, but the effect of degree of particle orientation was difficult to distinguish due to low aspect ratios of HAp particles which was not enough to impact on overall microstructure.

CHAPTER 1

INTRODUCTION

Polymer nanocomposites typically exhibit significant improvements in material properties over their neat polymer and conventional composites. These improvements are significantly attributed to the higher surface area associated with the nanoparticles. Since the surface area is varied by particle geometries such as the size, shape and aspect ratio, much of research have been reported that those parameters influenced material properties on polymer nanocomposites. Apart from the particle geometries, the material properties are strongly influenced by the dispersion, loadings, and arrangement of the particle. Especially, controlling particle arrangement in the polymer matrix can provide novel properties such as highly efficient catalysts, nanostructured solar cells and engineered aerospace components. Thus, investigating the effects of those parameters on nanocomposite properties will provide the basic knowledge to understand and design the nanocomposite with functional and structural applications. This research focused on the synthesis of hydroxyapatite (HAp) nanoparticles of controlled shapes using block copolymer templates and the construction of tensegrity-inspired microstructures where the synthesized nanoparticles were used as the compressive components and the polymer matrix was used as the tensile web. The research was conducted with the following objectives:

1. Synthesis of Hydroxyapatite (HAp) nanoparticles of controlled shapes using block copolymer templates.

2. Investigation of the effects of particle loadings, shapes, and polymer crystallinity on nanocomposite properties.

3. Arrangement of HAp nanoparticles into the appropriate microstructure and characterization of nanocomposites to determine processing-structure-property relationships.

General review of literature of nanocomposites, tensegrity structures, HAp, block copolymers, and biocompatible polymers was given in Chapter 2. The synthesis of HAp nanoparticles of controlled shapes using block copolymers was presented in Chapter 3. In this study, poly(ethylene oxide)-*b*-poly(metharylic acid) (PEO-*b*-PMAA) and poly(methyl methacrylate)-*b*-poly(methacrylic acid) (PMMA-*b*-PMAA) were used as block copolymer templates to introduce different moieties on the HAp nanoparticle surface. Needle and spherical shaped HAp nanoparticles were synthesized and the resulting particles were characterized to investigate the effect of block copolymers on the morphology of HAp nanoparticles. The results indicated that morphology of HAp nanoparticles was influenced by the mole ratio of the calcium precursor and the block copolymer, and general morphological behavior was independent of solvents used in synthesis.

In Chapter 4, two different shapes of HAp nanoparticles decorated with a PEO were dispersed in a PEO matrix to form nanocomposites, and those materials were characterized for particle dispersion and nanocomposites properties. The results indicated that the polymer coating promoted particle dispersion above 5 wt.% of particle loadings. The dispersion trends and thermomechanical properties were similar between needle and

spherical particle system. However, the polymer crystallinity and crystallization showed different trends as a function of particle loadings in two particle systems. The experimental results indicated that the surface area and interparticle distance influenced the matrix crystallinity.

In Chapter 5, the arrangement of particles in polymer matrix was manipulated by mechanical drawing process to construct a nanocomposite microstructure. The HAp nanoparticle arrangement in polymer matrix was evaluated using SEM and X-ray diffraction and the results showed that HAp nanoparticles had preferential orientation through the mechanical drawing process. The mechanical drawing process influenced polymer crystallinity and thermomechanical properties in semicrystalline nanocomposite system but did not significantly affect in amorphous nanocomposite system. The relative contribution of particle arrangement on nanocomposite properties was also investigated in both the semicrystalline and amorphous nanocomposite systems. The particle arrangement influenced enhanced mechanical properties, but the effect of the particle orientations from the first and second drawing process was difficult to distinguish due to the error.

In Chapter 6, the conclusion summarizes the results from the different studies and the future works are discussed.

CHAPTER 2

BACKGROUND

2.1. Nanocomposites

Since the pioneering work on nanocomposites performed by the Toyota Central Research in the late 1980s, polymer nanocomposites has generated significant scientific and technological interest over the last decades [1-4]. Polymer nanocomposites containing low volume fraction (1- 10 vol. %) have exhibited improved physical properties compared with neat polymer or conventional composites [5]. These enhancements are attributed to the increase in surface area linked to filler size reduction. The properties are strongly influenced by a number of factors, such as a filler shape and size, loading, dispersion and arrangement of the fillers in the matrix [6-8]. Winey *et al*. explained surface area/filler size relationship with Figure 2.1 which was shown the ratio of interfacial volume to the particle volume ($V_{\text{interface}}/V_{\text{particle}}$) as a function of the particle aspect ratio and the ratio of the interfacial thickness to the particle size [9]. Since interfacial thickness independent of the size of the particle, the relative volume of interfacial material with respect to the volume of the particle increases as the particle size decreases. Thus, controlling particle geometry is very important to design nanocomposites.

To date, much of research has focused on producing well-dispersed nanoparticles systems. The research indicated that well-dispersed particle morphology provided increased interfacial area between fillers and bulk materials, and higher interfacial area

led to enhancement of mechanical properties [10]. Achieving well dispersed nanoparticle morphology is a challenging problem because, most of cases, unfavorable interactions between filler and matrix could be observed. One strategy to facilitate particle dispersion as well as interfacial interaction is to modify the particle surface by using functional coupling agents or a grafted polymer coating enabling favorable interaction between filler and matrix. In polymer/clay nanocomposites, several studies have indicated that nanocomposites prepared via *in situ* polymerization in presence of functional coupling agents, such as moieties containing hydroxyl, carboxylic, or epoxy groups showed enhanced mechanical and thermal properties due to enhanced dispersion of particle and reaction between particle and matrix [11-14].

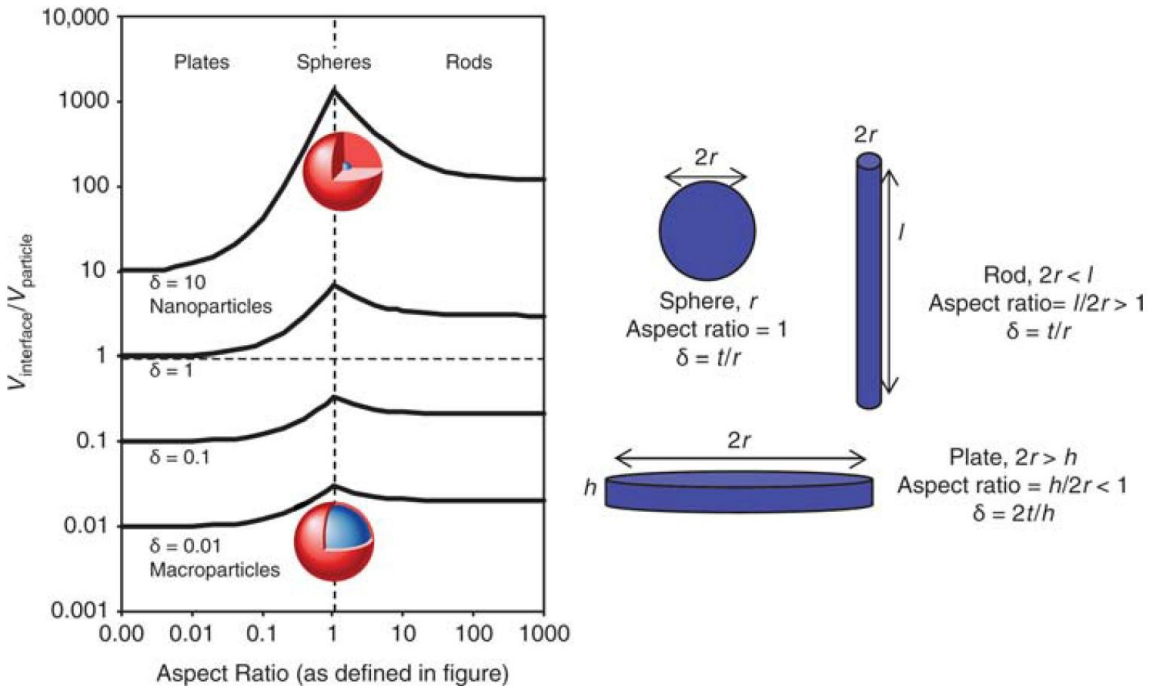

Figure 2.1. The ratio of interfacial volume to the particle volume ($V_{interface}/V_{particle}$) as a function of the particle aspect ratio and the ratio of the interfacial thickness to the particle size [9].

Some research results indicated that polymer grafting on the particle surface could impart an attractive interaction with the polymer matrix. Hong *et al*. reported that the grafting poly (L-lactic acid) (PLLA) on the HAp particle surface improved particle dispersion in chloroform compared to the untreated HAp particles which showed particle agglomeration [15]. The Kumar group has reported controlling the particle dispersion into polymer matrix [16-20]. They used polymer grafted nanoparticles miscible with the matrix polymer, and the resulting nanocomposites showed homogenous particle dispersion as well as self-assembled microstructures. The results indicated that nanoparticle dispersion correlated to the ratio of graft chain length to matrix chain. Homogenous particle dispersion was obtained when the matrix chain length was smaller than the graft chain length, while self-assembled structures were found when the matrix chain length was large. Some research had shown this dispersion transition occurs when the ration of the grafted chain length to the matrix chain length is 1 [21-23]. Thus, the ratio of length of the grafted chain to the length of the matrix chain could influence the morphology of nanoparticle dispersion and interfacial interaction between particle-particle and particle-matrix [16-20].

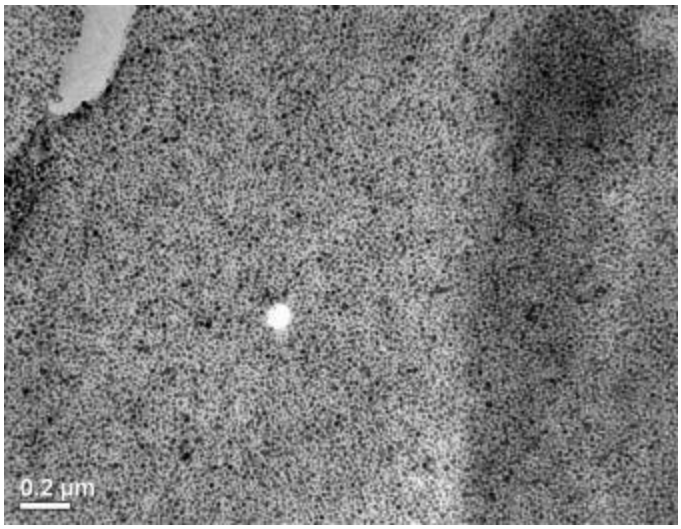

Figure 2.2. Homogenous particle dispersion morphology of SiO2-*g*-PMMA/PEO nanocomposite [20].

Recently, techniques for achieving spatial control of nanoparticles has received much attention since nanocomposites produced with controlled nanoparticle arrangement exhibited optimized electrical, optical and mechanical performance for practical applications [24, 25]. And also, several computational simulation studies have shown that well-controlled particle arrangement could yield significant improvement of mechanical strength [26, 27]. Gusev *et al*. reported a numerical study of elastic property of composite with well dispersed silica nanoparticles in a rubber matrix. The results showed honeycomb and web-like structure had exceptional higher moduli at 0.3 vol. fraction of silica than randomly dispersed particle system. This behavior was attributed to some three-dimensional particulate morphologies of honeycomb and web-like structure [26].

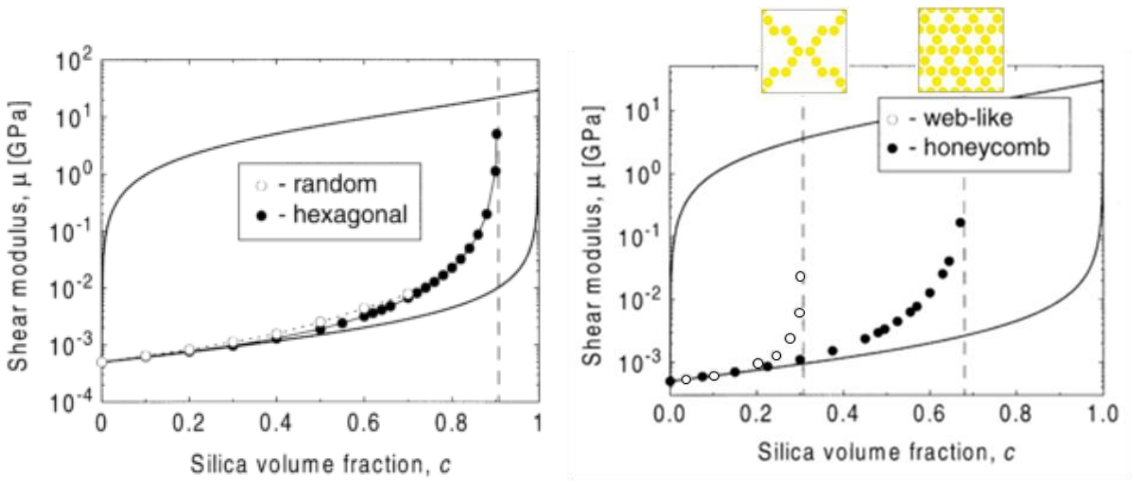

Figure 2.3. Numerical results obtained with random, hexagonal, honeycomb and web-like packing arrays. The two solid lines give the predictions of the Hashin-Shtrikman variation bounds. The vertical dashed lines show the maximum packing density that can be achieved assuming random, hexagonal, web-like and honeycomb packing arrays [26].

In order to control particle arrangement in the polymer matrix, several fabrication techniques have been reported such as shear orientation [28-31], block copolymer templated assembly [32-34], and mechanical drawing [35-38]. The Schmidt group has reported particle ordered structures of PEO-clay nanocomposites using the shear orientation. Natural montomorillonite (MMT) and synthetic laponite clay can be neutralized by complexation with the lone pair electrons on the ether oxygen in PEO backbone [31]. Since the amount of polymer adsorbed onto the clay can be controlled by the layer charge density on the clay, researchers were interested in the fabrication of hierarchically ordered PEO-clay nanocomposites. The hierarchically ordered structure was obtained by shear orientation of polymer-nanoplatelet system and the clay layers in the polymer matrix have highly ordered structure along the spreading direction [28-31].

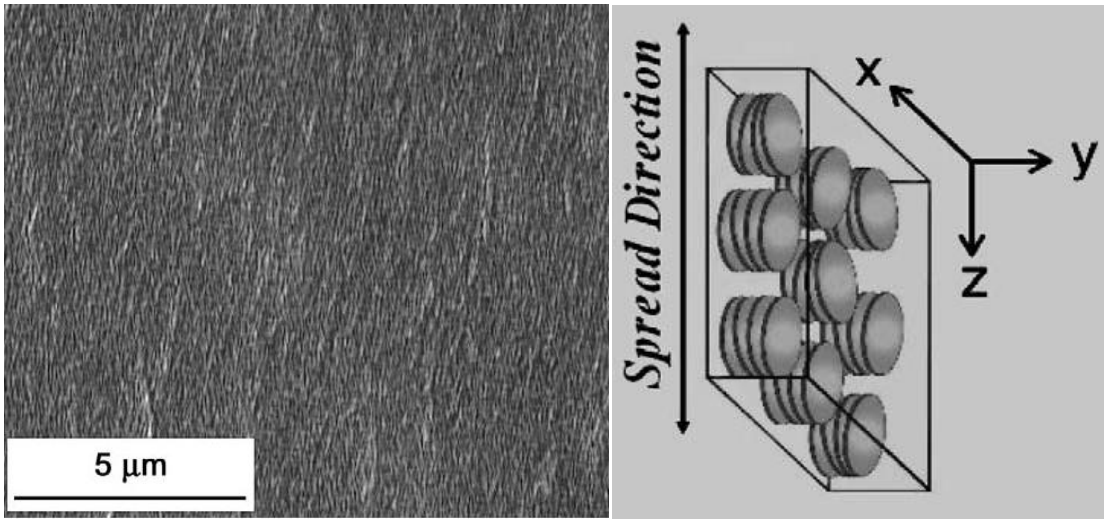

Figure 2.4. SEM image from nanocomposite film of clay 60%-PEO 40 % using shear orientation and the physical picture of general platelet orientation [30]

Koerner *et al*. reported three-dimensional arranged montmorillonite (MMT) composites using a uniaxial external magnetic field which MMTs were composed of two different minerals. The coefficient of thermal expansion (CTE) measurement showed that aligned layered silicates in an epoxy matrix decreased CTE in the direction of MMT alignment compared to the neat epoxy. This behavior was attributed to the three-dimensional reinforcement of aligning layered silicates, specifically compositional heterogeneities on the micrometer scale [39].

Kim *et al*. have investigated particle arrangement in the block copolymer matrix. They prepared polymer coated gold nanoparticles which tethered polymer was miscible with one of the blocks in block copolymer and controlled the location of gold particles in block copolymer domains using phase separation of block copolymers [32-34].

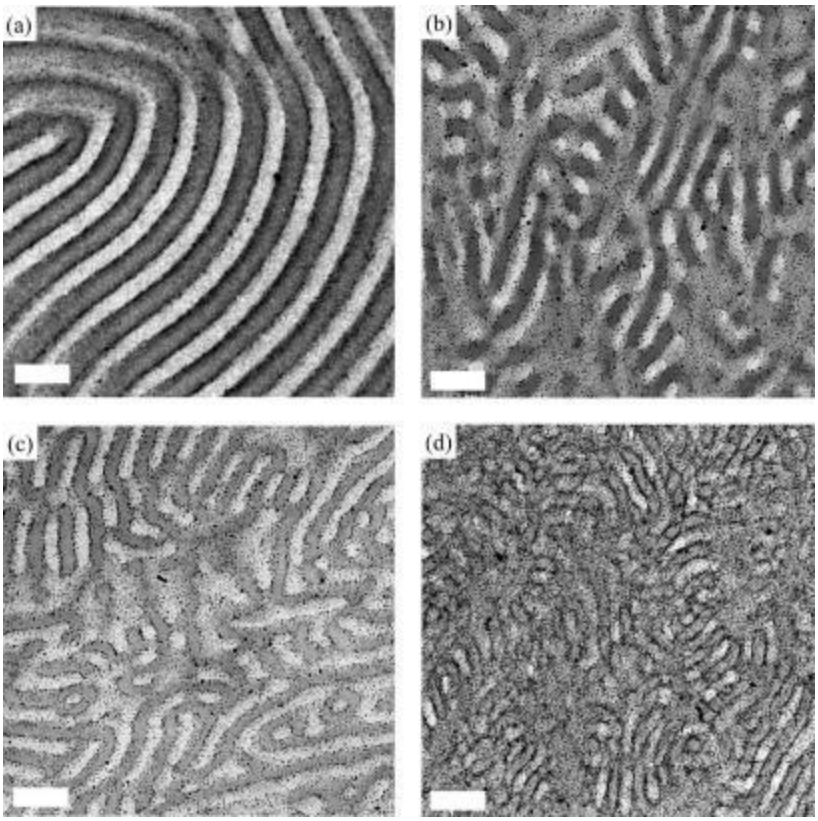

Figure 2.5. TEM images of PS-*b*-P2VP block copolymer containing PS-Au nanoparticles at various volume fractions, (a) 0.054, (b) 0.103, (c) 0.125, and (d) 0.173 [34].

In CNT/polymer nanocomposites, polymer films and fibers that contained oriented carbon nanotubes showed enhanced modulus [40], electrical conductivity [41] and thermal stability [42]. Koganemaru *et al*. reported the gelation/crystallization technique was effective way to produce composites with MWNTs and polyacrylonitrile (PAN). They could prepare the composite films easily by the combination of MWNTs with the gel state PAN matrix and draw the gel films which produce aligned MWNTs along the elongation direction. They showed enhanced storage modulus above 5 wt% MWNT content because CNTs tend to entangled agglomerates at higher MWNT loadings. This enhanced mechanical property was attributed to aligned MWNT [40].

2.2. Tensegrity

The development of stable structures having the optimized strength for a given amount of material is of great interest for material design. Since the tensegrity structure was introduced by Snelson, Fuller and Emmerich in the 1940's, it has been a matter of surprise and fascination. Richard Buckminster Fuller described the tensegrity principle as "islands of compression inside an ocean of tension" [43]. This state can be explained that compression and tension are important components to describe tensegrity structures according to their state of load effect. This concept included that compression is inside tension, and also compressed components compose a discontinuous set and tensioned components are gathered in a continuous set. Overall, the whole system is in the equilibrium state. Based on this concept, tensegrity structure can be explained by the following definition: " A tensegrity system is a system in a stable self-equilibrated state comprising a discontinuous set of compressed components inside a continuum of tensioned components." [44] A network of tensioned components can only carry significant tension whereas a discontinuous set of components can resist any tension, compression, and bending force. As a result, the structure composed of these two components has the ability to maintain an equilibrium state responsive to external mechanical stresses. An example tensegrity structure is shown in Figure 2.6. Thus, the structure can be used to design light-weight and strong materials.

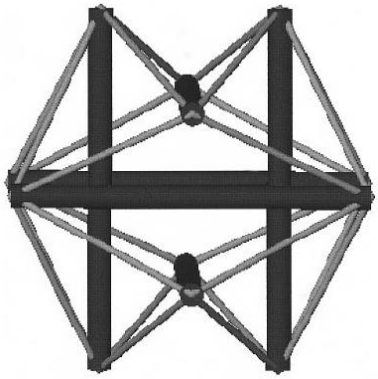

Figure 2.6. A 6-strut and 24-cable tensegrity model in an equilibrium form [Molecular Geodesics Inc.]

Tensegrity structures are found in living cell systems. The Ingber group has hypothesized that many different types of cells use tensegrity for cell shape stability [45-48]. The molecular filaments in living cell consist of microfilaments, microtubules, and intermediate filaments and the mechanism of mechanical behavior of the cell could be explained by tensegrity structure. Contractile microfilaments and intermediate filaments act as a stabilizing tensile stress within the molecular filaments that is controlled the stability by internal microtubules and by extracellular adhesion [49].

Liedl *et al*. have reported nanoscale, prestressed, three-dimensional tensegrity structures made from DNA molecules [50]. They used honeycomb-pleat base targets which could be rolled for controlling DNA structures, and prepared three-dimensional DNA structures. Rigid bundles of DNA double helices underwent compressive forces, and a single strand DNA acted as tension bearing cables. This research showed these DNA structures could self-assemble against up to 14pN, which was a mechanical response similar to those displayed by living cellular systems.

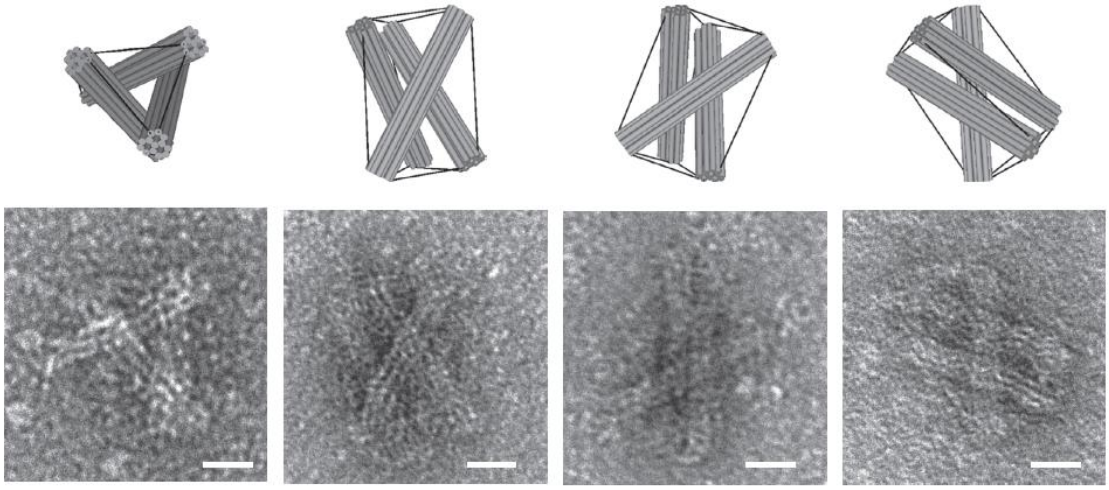

Figure 2.7. Three-dimensional prestressed DNA tensegrity. Perspective views of cylinder models of DNA tensegrity (the first row) and TEM micrographs of typical structures (the second row). Scale bars, 20 nm [50].

In the tensegrity structures research, more attention has been paid so far to simulation modeling to understand their behaviors. Several studies have been reported computational analysis of tensegrity structure dynamics. Sultan *et al*. have investigated the stability of tensegrity structure corresponding equilibrium configuration and stiffness. Based on these theoretical contributions, several applications of tensegrity structures have been proposed such as tensegrity antenna [44], sensors [51], and space telescope [52].

In order to translate this structure to nanocomposites, the structure will be constructed through manipulation of the nanoparticles, interphase material and polymer matrix as shown in Figure 2.8. In this structure, the material containing the nanoparticles and the interphase material will be considered building block and the polymer matrix will be the tensile web for the tensegrity-inspired structure.

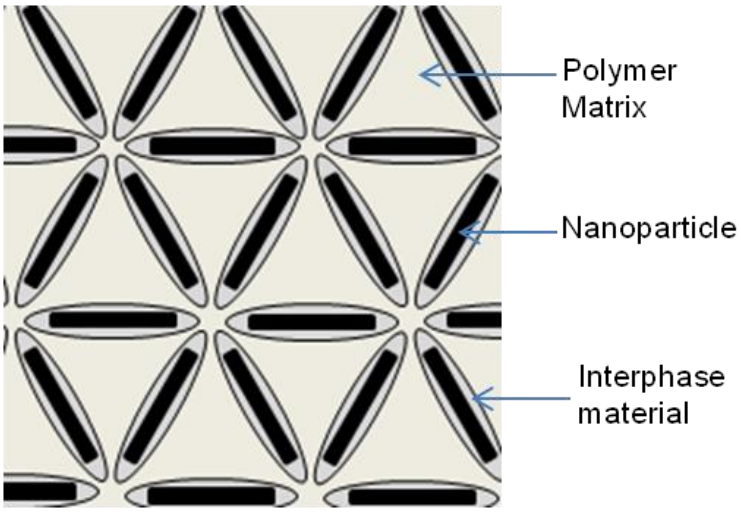

Figure 2.8. Representative model for tensegrity inspired microstructure.

In this research, HAp nanoparticles were synthesized using block copolymer templates. Since these particles were coated with polymer blocks which were same chains as the matrix polymers, the polymer coated HAp particles were considered as the interphase material which would be used to prestress the HAp nanoparticles and could facilitate particle dispersion in the matrix, forming building blocks for constructing tensegrity inspired microstructure. During processing the HAp nanoparticles were introduced into two different polymer matrices and the particle arrangement was controlled by mechanical drawing process. The final samples were characterized and an investigation into how the particle arrangement influenced material properties was performed.

2.3. Hydroxyapatite (HAp)

Hydroxyapatite (HAp) is one of the most widely used bioceramic materials in the field of biomaterials and tissue engineering because it is a major constituent of bone. Thus, HAp has been widely used in biomedical applications such as bone grafting, artificial bone, coating for joint material, and dental fillers and so on in the form of composites [53-55]. The HAp is a member of the apatite family of calcium phosphates that the chemical formula of HAp is $Ca_{10}(PO_4)_6(OH)_2$, and the stoichiometric ratio of Ca/P in HAp is 1.67. Table 2.1 gives a list of the properties of HAp.

Table 2.1. Physiochemical and mechanical properties of hydroxyapatite (HAp) [56][57][58]

Properties	Experimental Data
Density (g/cc)	3.05-3.15
Elastic Modulus (GPa)	7-110 (depends on porosity)
Ultimate tensile strength (MPa)	38-48
Compressive strength (MPa)	350-450
Fracture Toughness (MPa m1/2)	0.7-1.2
Melting point (°C)	1614
Unit cell	Hexagonal
Lattice parameters	a=9.432Å, c= 6.881Å
Poisson's Ratio	0.27

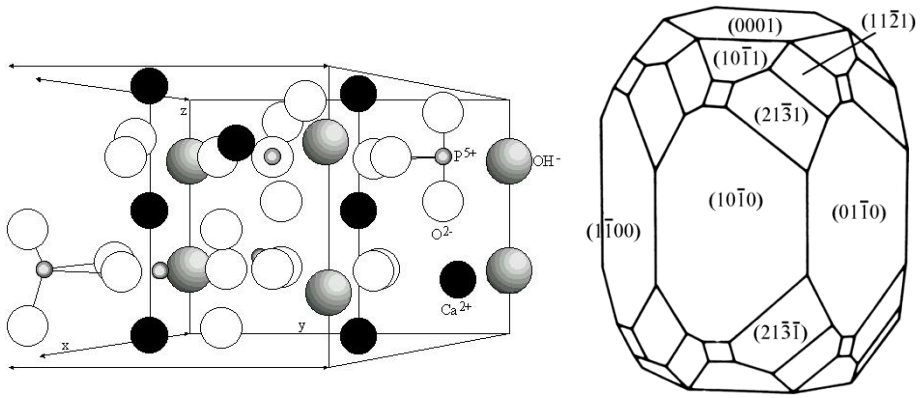

Figure 2.9. Crystal structure of hydroxyapatite (HAp) [sources: boundlessthicket.blogspot.com and web.mit.edu]

Natural and synthetic HAp can have different chemical composition and behavior. It is well known that most synthetic HAps have the chemical composition of $Ca_{10}(PO_4)_6(OH)_2$, whereas human bones do not have pure or stoichiometric HAp. Generally, human bones contain ions such as CO_3^{2-}, Na^+, Mg^{2+}, Fe^{2+}, Cl^-, and F^-. Thus, the Ca/P molar ratio of in bone is lower than 1.67. However, pure HAp is the most stable calcium phosphate salt at normal temperatures and pH between 4-12, and also have biocompatibility in human body. Thus, HAp is considered as a model compound to study biomineralization phenomena and has been a strong interest for synthetic, extra pure, and well defined HAp crystal [59, 60].

Recently, nano-sized HAp has received much attention because of its superior functional properties such as osteoblast adhesion, proliferation, osteointergration, and deposition of calcium-containing minerals on its surface [61]. Several techniques have been used to synthesize nano-sized hydroxyapatite particles, including solid state reactions, wet chemical methods, hydrothermal process and microemulsion processing. Solid state reactions can give a stoichiometric and well-crystallized product, but they

required relatively high processing temperature and long reaction time [62]. Wet chemical methods can also be use to obtain nanometer sized powders. However, their crystallinity and Ca/P ratio depend on the preparation conditions and, in many cases, it is difficult to control Ca/P ratio of HAp crystals [63, 64]. A hydrothermal process can prepare HAp with a high crystallinity and a Ca/P ratio close to crystalline HAp. However, the synthesized HAp showed particle agglomeration in polymer matrix and the size distribution was broad [65, 66]. A hydrothermal microemulsion technique can be used to synthesize nanopowders, nanoneedles and nanowires. Microemulsion can serve as a nano reactor to control the particle size and size distribution in the reactions and also inhibits excessive agglomeration of particles [67, 68]. Zhou *et al*. reported nano-sized spherical carbonated HAp was synthesized by the microemulsion synthesis method. However, the nanoparticles were an amorphous state, thus they were needed calcination steps to obtain high crystallinity [68].

Among the methodologies, HAp nanoparticle synthesis in the presence of double-hydrophilic block copolymers is an attractive route for this research because outer block can prevent the particle agglomeration in a miscible polymer matrix. Poly(ethylene oxide)-based block copolymers where the secondary block is a poly(carboxylate) such as poly(aspartic acid) and poly(methacrylic acid) have been studied for HAp synthesis. Antonietti *et al.* used poly(ethylene oxide)-*b*-poly(methacrylic acid) (PEO-*b*-PMAA) as a dispersed template for the control of HAp growth [69]. At different pH, two different types of discrete nested structures were obtained. Tjandra *et al.* also showed similar results, and this result was attributed to the morphological change of PMAA block at pH 4-6 [70].

In this research, we showed a new synthetic method for preparing nano-sized HAp particles. The nano-sized HAp particles were prepared using block copolymer templates. The block copolymer could control geometry and surface properties of HAp nanoparticles, and the decorated HAp nanoparticles could promote particle dispersion in the polymer matrix. Moreover, the block copolymer on the HAp would act as the interphase between the HAp and the polymer matrix and used as a means to construct tensegrity-inspired microstructures.

2.4. Block Copolymers as Dispersed Templates for Nanoparticle Synthesis

As mentioned in the previous section, the manipulation of nano-sized particles has received much attention because nanocomposites possess unique size-dependent properties. It is also an important issue to modify the surface of nanoparticles to stabilize these particles and arrange them within the microstructures. In recent years, double-hydrophilic block copolymers (DHBC) have been studied for this purpose. A DHBC is a diblock copolymer which consists of two water-soluble blocks of different chemical properties. In many cases, one block promotes dissolution in solvents or polymer solutions, and the other part interacts with the surface of nanoparticles. A DHBC can induce micelle formation by a temperature or pH change, as well as complexation with appropriate molecules. Several studies have shown that DHBCs were efficient growth modifiers for calcium carbonate [71], ZnO [72], and calcium phosphate (CaP) [69, 70, 73].

Recently, Guragain *et al*. have reported two distinct types of micelle structure from PEO-*b*-PMAA in aqueous solutions, one with a PEO-core surrounded by a PMAA corona and the other with a PMAA core surrounded by a PEO-corona as shown in Scheme 2.1 [74]. The PEO-core micelles were prepared by decreasing the cloud point of the PEO block to room temperature by adding phosphate ion. The PMAA-core micelles were prepared by changing the pH of PEO-*b*-PMAA solution. In particular, PMAA underwent a conformational transition at pH 4-6 [75]. PEO-*b*-PMAA can form micelles with a hydrophobic core of PMAA at low pH level, and these micelles start to disintegrate into a linear block copolymer chain when the pH exceeds 5 because the

COOH groups in the block copolymer are ionized to COO^- groups. When Ca^{2+} ions are introduced into block copolymer solutions at high pH level, the COO^- group of PMAA is neutralized by Ca^{2+} ions, and forms insoluble hydrophobic core that is stabilized by a PEO corona. This study also showed the reversibility between PMAA-core and PEO-core by removing the counter ions from the block in PEO-*b*-PMAA.

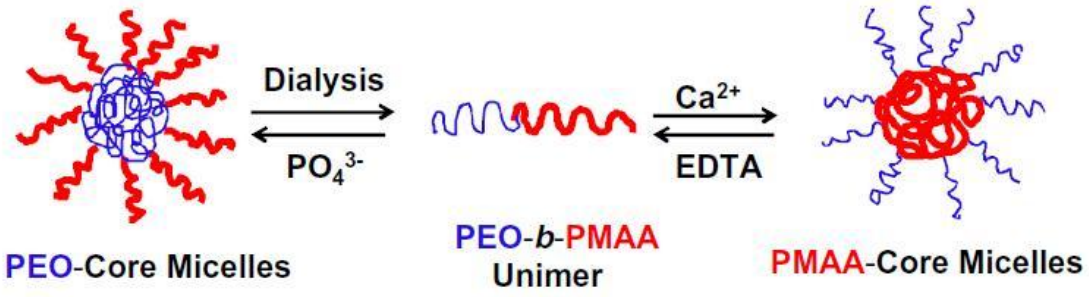

Scheme 2.1. Schematic representation of PEO-b-PMAA behavior [74].

Marentette *et al*. studied about the effect of PEO-*b*-PMAA on the growth of $CaCO_3$ in the calcite modification [71]. They observed extensive morphological changes which could be attributed to the block copolymer structure. In the presence of the DHBCs, the expected rhombohedral calcite crystals were not formed but, instead, elongated rhombohedrons were obtained due to a reduction of the crystal growth rate in directions perpendicular to the c-axis by the adsorption of the block copolymers [71].

Besides the controlled $CaCO_3$ crystallization, PEO-*b*-PMAA was successfully applied to the modification of ZnO [72]. The block copolymer led to a narrow particle size distribution, and the crystal size parallel to the c-axis was restricted. As the block copolymer concentration was increased, the size distribution was narrower and the aspect ratio of the crystal decreased.

Antonietti *et al*. have shown that PEO-*b*-PMAA and some of its derivatives efficiently suppressed the formation of large calcium phosphate (CaP) and preferred the formation of unique nested CaP/DBHC hybrids shown in Figure 2.10. At the initial step, the polymeric aggregate acted as a cage for the crystallization reaction of the CaP crystal modification. The formation of the unusual fibers suggested a local cooperative interaction between precipitated CaP clusters and the polymer, which controlled the highly anisotropic growth of 3 nm thick up to several um long filaments. With increasing time, the individual tangles became inter-linked to give extended neuronal network structures; at a pH level of 4.2, a different growth phenomenon was observed. A more soluble calcium phosphate modification was nucleated, forming star-like hybrid superstructures with thicker and shorter filaments than in the CaP case. After a second, transverse growth process on the filaments, they were destabilized while the dense central core of the colloid developed into an ordered inorganic/organic mesophase [18]. Tjandra *et al.* have reproduced these experiments and proposed a growth model for the formation of these hybrids [70].

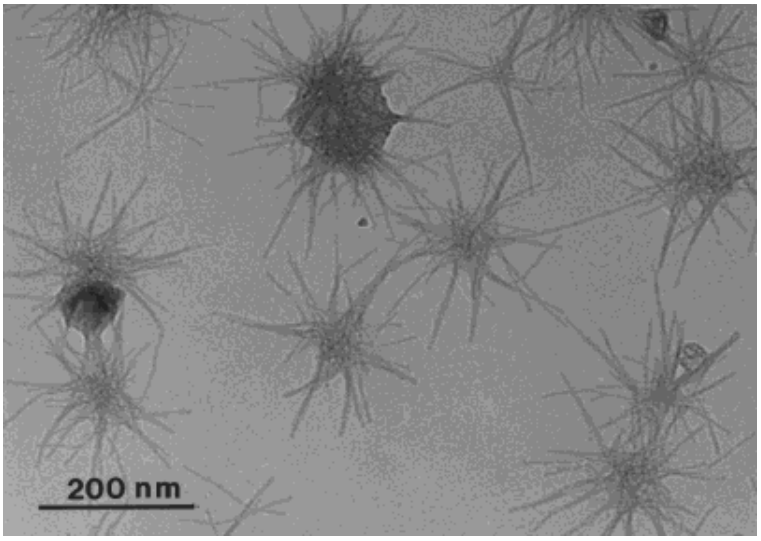

Figure 2.10. TEM image of CaP with a nested structure [18]

Kataoka *et al.* have reported the formation of uniform CaP nanoparticles by mixing calcium/DNA and phosphate/poly(ethylene oxide)-*b*-poly(aspartic acid) PEO-*b*-PAA or PEO-*b*-PMAA solutions [76-78]. The nanoparticles had an interesting core of DNA, CaP, and PAA or PMAA, which was stabilized by PEO shell. The purpose of the block copolymer was to prevent precipitation of CaP nanoparticles and stabilize the final nanoparticles. These particles have been proposed as carriers for gene therapy.

Tjandra *et al.* also reported the controlled synthesis of calcium phosphate using poly(methylmethacrylate)-*b*-poly(methacrylic acid) (PMMA-*b*-PMAA) block copolymer from aqueous solution at different pH levels [79]. At pH 4, nano filament CaP was synthesized due to a weak interaction between calcium ion and unionized MAA segment. An interesting structure of hollow spherical morphologies could observe at higher pH level as shown in Figure 2.11. The shell thickness and pore size were controlled by the block length of PMMA and the degree of ionization.

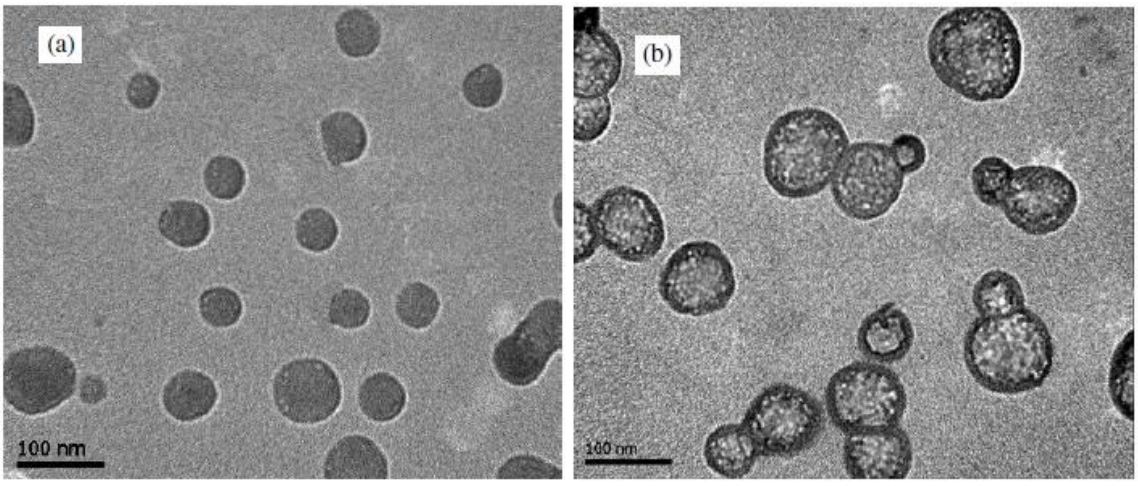

Figure 2.11. TEM image of CaP with PMMA-b-PMAA at pH 9 before calcinations (a), after calcinations (b).

In this research, two different shapes of HAp nanoparticles were synthesized using block copolymer templates. The results indicated that the morphology of HAp nanoparticles was related to the block copolymer concentration. The carboxylic acid group in block copolymers influenced the growth rate of inorganic nanoparticles. This behavior was attributed to restriction of crystal size in directions to the c-axis by the adsorption of the block copolymers.

2. 5. Biocompatible Polymers

Biocompatible materials such as metals, ceramics and polymers have been extensively used for biomedical applications. Metals and ceramics have contributed to major advances in the biomedical field such as orthopedic tissue replacement. However, there were several limitations for using biomedical applications because they are not biodegradable and easily processable. On other hand, polymer materials have been widely used for this application because their biodegradability and processability could be easily controlled. Polymer materials have been used several important uses in biomedical applications. Examples included poly(methyl metacrylate) bone cement, poly(glycolic acid) degradable sutures, poly(glycolic-co-lactic acid) bone screws, and poly(vinyl siloxane) dental materials. In addition, poly(ethylene glycol) was used to extend the circulation half-life of drugs and poly(hydroxyethyl methacrylate) was used to produce soft contact lenses [80, 81].

Poly(ethylene oxide) (PEO) (Figure 2.12) is a non-biodegradable polymer, and it shows excellent physical, chemical and biological properties, including hydrophilicity, solubility both in water and some organic solvents, lack of toxicity. PEO is used to restrict and control the cell and protein attachment on scaffolds. Since the PEO increased the hydrophilicity, antibodies and other proteins are difficult to attach to the scaffolds, and it reduces any adverse immune response. Besides using PEO homopolymer, the using of copolymer with PEO has been studied controlling the cell attachment characteristics of the scaffolds and enhancing the biocompatibility and permeability [81, 82].

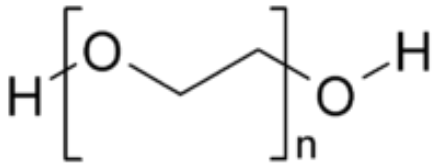

Figure 2.12. Structure of repeat unit of poly(ethylene oxide) (PEO) (Source: Wikipedia)

Poly(methyl metacrylate) (PMMA) (Figure 2.13) or acrylic bone cement has been the most commonly used nonmetallic implant materials for biomedical applications since they have low water absorption, nontoxicity, dimensional stability, appearance, and ease of forming. PMMA was first introduced as a bone cement in the early 1960s by Charnley and Smith [83, 84]. PMMA allowed even distribution of implant loads, and formed a strong mechanical bond with implants. In order to increase adhesion to bone surface and mechanical properties, HAp powders were added to PMMA. Several studies showed addition of HAp promoted the capability of bone regeneration of PMMA and generated synergistic effects to reinforce the mechanical properties [85, 86].

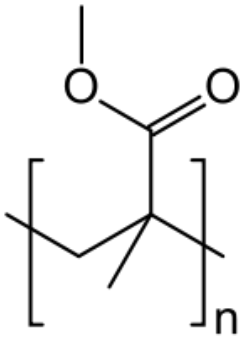

Figure 2.13. Structure of repeat unit of poly(methyl metacrylate) (PMMA) (Source: Wikipedia)

These kind of biocompatible polymers have been used as the matrix of the composites for the application in joint fixation and other long-term implants. The composites had been prepared with HAp and fibers. Webster *et al*. have reported an enhanced function of osteoblast on nano-sized ceramics [61]. In addition, a number of investigations have recently been conducted to determine the mineralization, biocompatibility and mechanical properties of nanocomposites based on various biocompatible polymers. These researches covered HAp/polylactide and its copolymer [15, 87-89], HAp/chitosan [90], HAp/collagen [91, 92], and HAp/gelatin [93, 94].

In this study, HAp nanoparticles synthesized using block copolymer templates were dispersed into two different polymer matrices to investigate their physical properties.

2. 6. Summary and Goal of Dissertation

In previous our group studies from this group, the effects of matrix crystallinity were investigated. The results showed homogenous particle dispersion occurred only at low particle loadings (1 wt.% and below) in relatively high level of matrix crystallinity (70%) [95]. Thus, it was very difficult to obtain isolated particles which could be used for building blocks in tensegrity-inspired microstructure.

In this study, a new method for preparing the building block was investigated. In order to achieve nanoparticles contained interphase material, block copolymers were used for synthesizing HAp nanoparticles, and the synthesis mechanism was investigated. Since the particles were coated by block copolymers, the polymer coating on HAp particle would be used to prestress the particles and formed building blocks for constructing tensegrity inspired microstructure. Nanocomposites prepared by these particles were characterized the effect of particle loadings, shapes and matrix crystallinity on their properties. In order to construct tensegrity-inspired microstructures, the particle arrangement was manipulated using a mechanical drawing process. The effect of drawing processes on the particle arrangement, matrix crystallinity, and nanocomposite properties was also characterized.

CHAPTER 3

SYNTHESIS OF HAp NANOPARTICLES OF CONTROLLED SHAPES USING BLOCK COPOLYMER TEMPLATES

3.1. Introduction

Hydroxyapatite (HAp) is a member of the apatite family of calcium phosphates that the chemical formula is $Ca_{10}(PO_4)_6(OH)_2$, and the stoichiometric ratio of Ca/P in HAp is 1.67. HAp has been used in biomedical applications with many compounds since it is a major constituent of bones and teeth [96, 97]. In biomedical applications, HAp/biocompatible polymer nanocomposites have been extensively studied due to the ability to control biodegradability, bioactivity, and mechanical properties [98-100]. Especially, the composite properties have been influenced by the morphology of nanoparticles [101, 102]. For example, whisker or plate-like HAp particle showed enhanced fracture toughness/strength of HAp [102]. It is also an important issue to modify the surface of nanoparticles to stabilize these particles within the nanostructures [103].

In this research, the effect of DHBC on the morphology of HAp nanoparticles is studied. Specifically, HAp nanoparticles were synthesized using poly(ethylene oxide)-*b*-poly(methacrylic acid) (PEO-*b*-PMAA) and poly(methyl methacrylate)-*b*-poly(methacrylic acid) (PMMA-*b*-PMAA) block copolymers, and the morphology and structure of the nanoparticles were investigated as a function of block copolymer concentration. The results indicated that the synthesis method produced copolymer

coated nanoparticles with different shapes and that morphology of HAp nanoparticles was influenced by the mole ratio of the calcium precursor and the block copolymer used in synthesis. The ability to produce nanoparticles with controlled shape and surface chemistry suggests that this synthesis method is appropriate for composite applications.

3.2. Experimental

3.2.1. Materials.

Calcium nitrate tetrahydrate ($Ca(NO_3)_2.4H_2O$) (Alfa Aeser) and phosphoric acid (H_3PO_4) (Fisher Scientific) were used as the calcium and phosphorous precursor for the synthesis of HAp nanoparticles. PEO-*b*-PMAA and PMMA-*b*-PMAA block copolymer were purchased from Polymer Source, Inc. and used as-received. Based on the manufacturer's product literature, PEO-*b*-PMAA has a PEO block with the average molecular weights (M_n) of 7,500 g/mol and PMMA block with 15,500 g/mol, while PMMA-*b*-PMAA has PMMA block with 8,500 g/mol and PMAA block with 5,100 g/mol, respectively. Ammonium hydroxide (NH_4OH) (Mallinckrodt Chemicals) was used for maintaining pH.

3.2.2. Synthesis of HAp using PEO-*b*-PMAA Template.

The HAp synthesis with a PEO-*b*-PMAA block copolymer was performed in water. A solution of PEO-*b*-PMAA was prepared in deionized (DI) water at pH 11 and sonicated for 10 min using a bath sonicator. Aqueous solutions of the calcium and phosphorus precursors were also prepared using DI water. A 0.5 M aqueous solution of calcium nitrate tetrahydrate was added to the block copolymer solution and stirred mildly with a magnetic stirrer for 10 min. A stoichiometric amount of the 0.3 M aqueous solution of phosphoric acid was then added to achieve a Ca:P ratio of 1.67:1, and the mixture was aged for 24 hr. During the process, the pH was maintained at the initial value

by the addition of acid or base. Finally, the products were washed with DI water using a centrifuge to remove the nitrate and ammonium ions [104].

3.2.3. Synthesis of Hydroxyapatite (HAp) using PMMA-*b*-PMAA Template.

Tetrahydrofuran (THF) (EMD Chemicals) was used as a solvent for the synthesis. In this synthesis, phase separation and precipitation of precursors were not observed since THF is miscible with water, precursors, and NH_4OH. A solution of PMMA-*b*-PMAA was prepared by dissolving the block copolymer in THF and sonicated for 10 min using a bath sonicator. Aqueous solutions of the calcium and phosphorus precursors were prepared using DI water. A 0.5 M aqueous solution of calcium nitrate tetrahydrate was added to the block copolymer solution and stirred mildly with a magnetic stirrer for 10 min. Then, the mixture was adjusted pH to 9-10 using NH_4OH and stirred mildly with a magnetic stirred for 30 min. A stoichiometric amount of the 0.3 M aqueous solution of phosphoric acid was then added to achieve a Ca:P ratio of 1.67:1, and the mixture was aged for 24 hr. During the process, the pH was maintained at 9-10 by the addition of acid or base. Finally, the products were washed several times with DI water and THF using a centrifuge to remove unreacted block copolymer as well as the nitrate and ammonium ions [104].

3.2.4. Characterization of HAp Nanoparticles.

The morphology of the HAp nanoparticles was observed using a LEO 1530 scanning electron microscope (SEM). Particle samples for SEM imaging were dispersed in ethanol by sonication and deposited on lacey carbon coated Cu grids. The amount of block copolymer incorporated with HAp was determined using thermogravimetric

analysis (TGA) with a TA Instruments Q5000 TGA. The HAp nanoparticles were heated from 30 ˚C to 650 ˚C at a rate of 10 ˚C/min under N_2 atmosphere. The weight loss from 100 ˚C to 650 ˚C was attributed to the block copolymer mass. The average weight loss in this temperature range from two TGA experiments was reported as the mass of the copolymer coating for each nanoparticle system. The chemical and crystalline structures of the synthesized HAp nanoparticles were characterized using Fourier transform infrared spectroscopy (FT-IR) and X-ray diffraction (XRD), respectively. FT-IR was performed using a Nicolet Nexus 870 FT-IR spectrometer. The HAp nanoparticles were mixed with KBr (EMD Chemicals) and pressed into pellets for these measurements. The spectra were recorded at room temperature in the range 4000- 400 cm^{-1} using 64 scans and a resolution of 2 cm^{-1}. XRD was performed using a X'Pert PRO Alpha-1 with Cu-Kα radiation (λ = 1.54Å) and XRD peaks were collected 2θ = 10˚ to 50˚ with a step size of 0.02˚.

3.3. Results and Discussion

3.3.1. Synthesis of HAp using PEO-*b*-PMMA Template

3.3.1.1. Morphology of HAp PEO-*b*-PMAA Nanoparticles.

Scheme 3.1 shows the probable route for HAp synthesis using the PEO-*b*-PMAA block copolymer template. In aqueous solution at low pH, the PEO-*b*-PMAA block copolymer formed a micelle structure with a hydrophobic core of PMAA. At pH 4-6, the PMAA block underwent a chain conformational transition, and the micelle started to disintegrate into linear block copolymer chains [75]. The micelle was destroyed when the pH exceeded 5 because the COOH groups in the block copolymer were ionized into COO^- groups. When Ca^{2+} ions were added into block copolymer solutions at high pH level (pH> 9), the COO^- group of PMAA was neutralized by Ca^{2+} ion, and the micelles were formed again. These micelles adopted a similar structure to the previous micelles with the PMAA blocks and precursor materials in the center of the micelle and the PEO blocks forming the outer shell in contact with the water. Then, particle synthesis proceeded inside the micelle.

Since the aim of this study was to synthesize different nanoparticle shapes with HAp, six different synthesis conditions were explored by systematically varying the concentration of the PEO-*b*-PMAA copolymer solution and the amount of precursor solutions used in the synthesis. In all conditions, the calcium to phosphorous ratio was maintained at 1.67. Only the overall amount of precursor was changed. As shown in Figure 3.1, this approach yielded two different HAp nanoparticle shape: needle and

sphere. Similarly, previous research with block copolymer mediated nanoparticle synthesis has shown that the size or shape of HAp nanoparticles could be altered with synthesis conditions [69, 70, 76-78]. In some of those studies, the change in particle size was attributed to the increase in the surface area with an increased concentration of the block copolymer [77, 78]. In this work, another parameter was investigated to support previous conclusions. Analysis of the synthesis conditions used here showed that the morphology of the particle correlated to the Ca^{2+}/COO^- mole ratio as shown in Table 3.1. At lower Ca^{2+}/COO^- mole ratios ($n_{Ca^{2+}}/n_{COO^-} < 3.0$), most of the particles had a spherical morphology, whereas particles with the needle morphology were synthesized at higher Ca^{2+}/COO^- mole ratios ($n_{Ca^{2+}}/n_{COO^-} > 4.9$).

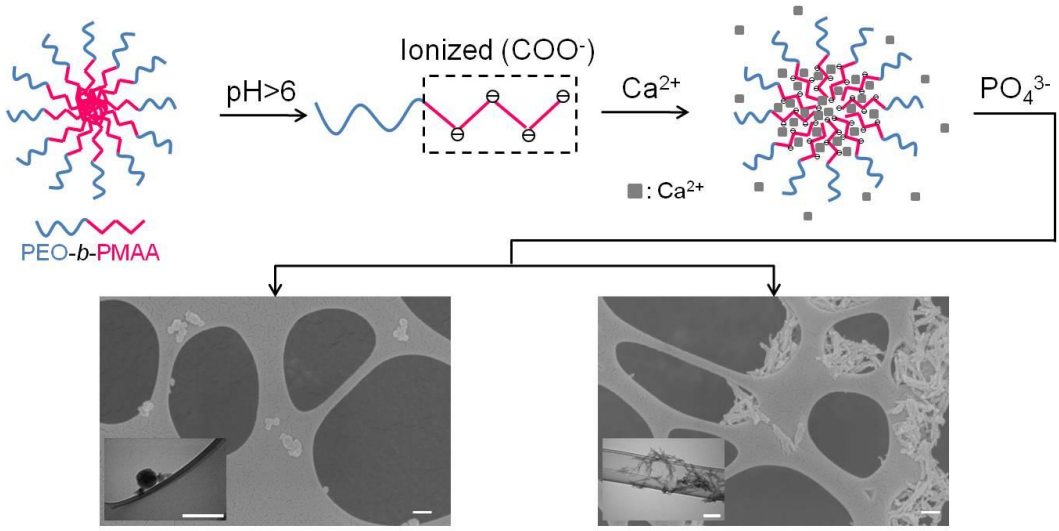

Scheme 3.1. Scheme for synthesis of HAp nanoparticles using PEO-*b*-PMAA block copolymer template and their morphological investigations by SEM and TEM (inset images). The scale bars represent 200 nm.

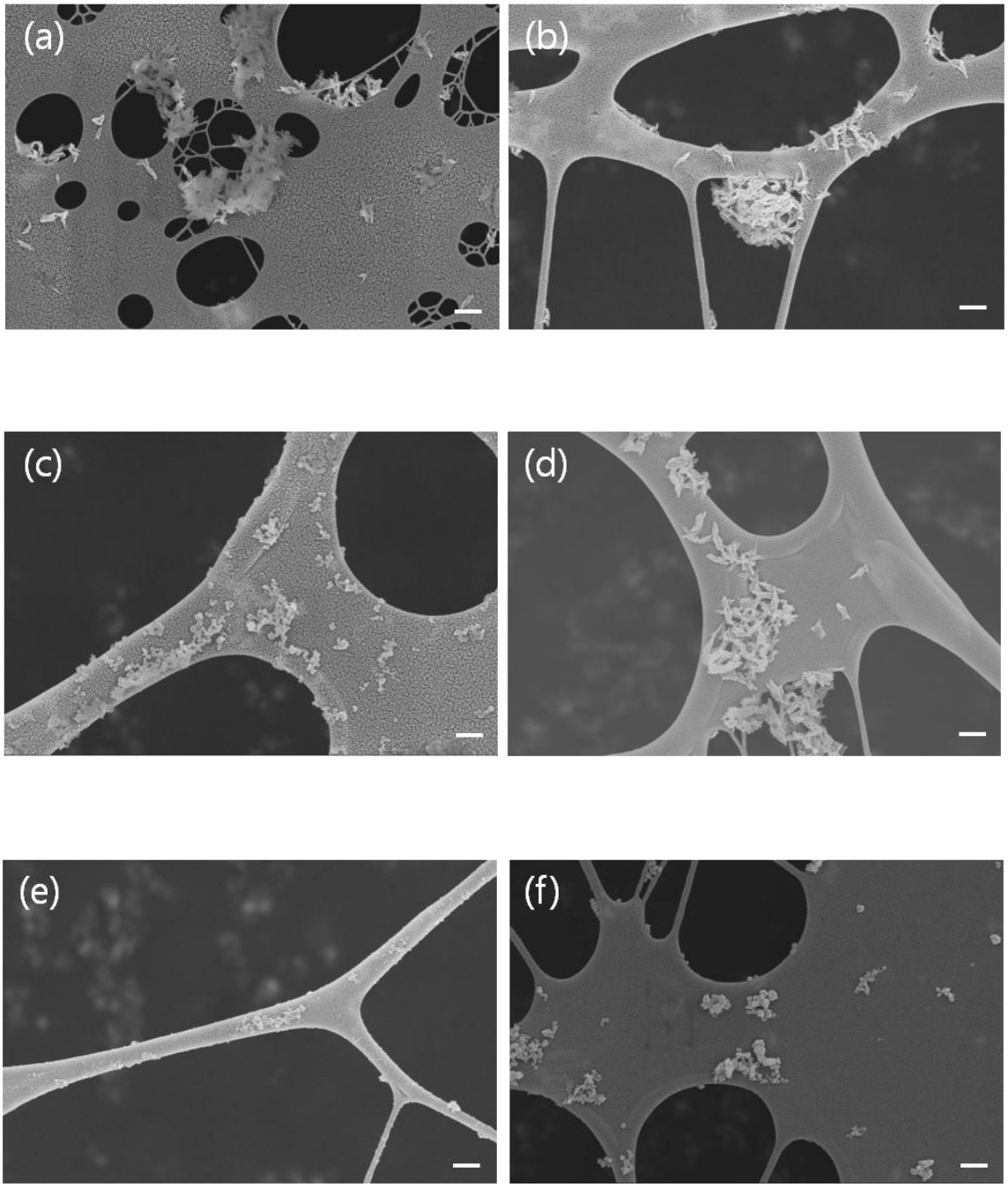

Figure 3.1. SEM micrographs of HAp particles synthesized with PEO-*b*-PMAA solution concentration at 0.5 mg/mL with 200 µL (a), and 500 µL (b) precursors; PEO-*b*-PMAA solution concentration at 1 mg/mL with 200 µL (c), and 500 µL (d) precursors; PEO-*b*-PMAA solution concentration at 2 mg/mL with 200 µL (e), and 500 µL (f) precursors. The scale bars represent 300 nm.

Table 3.1. HAp nanoparticles shapes at different PEO-*b*-PMAA concentrations and calcium precursors.

Calcium precursor (μL)	PEO-*b*-PMAA concentration (mg/mL)	$n_{Ca^{2+}}/n_{COO^-}$ [a]	Particle shape
200	0.5	4.9	needle
	1	2.4	sphere
	2	1.2	sphere
500	0.5	12.2	needle
	1	6.1	needle
	2	3.0	sphere

[a] $n_{Ca^{2+}}$ and n_{COO^-} are the moles of Ca^{2+} ions and COO^- groups in PEO-*b*-PMAA, respectively

In this study, we selected two different morphologies of the synthesized HAp for further characterization. The selected samples are shown in Figure 3.1b and 3.1f. These samples had the largest and smallest aspect ratio, respectively. The amount of block copolymer associated with the two different morphologies of HAp after recovering the particles from synthesis was determined with TGA as the weight loss between 100 °C and 650 °C. The weight of adsorbed block copolymer is shown in Table 3.2 together with the HAp particle dimensions. The amount of adsorbed block copolymer on the recovered particles was greater at higher block copolymer concentration during particle synthesis, but the amount of adsorbed polymer did not scale directly with the amount used in synthesis.

Table 3.2. The contents of PEO-*b*-PMAA on the HAp and the HAp particle size.

Sample	PEO-*b*-PMAA concentration (mg/mL)	$n_{Ca^{2+}}/n_{COO^-}$	PEO-*b*-PMAA (wt. %)[a]	Particle size (nm)[b]
HAp PEO-*b*-PMAA needle	0.5	12.2	11.1 ± 0.8	l[c]: 330 ± 30 d[d]: 55 ± 5
HAp PEO-*b*-PMAA sphere	2.0	3.0	21.8 ± 1.3	d:100 ± 11

[a] The average value from TGA
[b] The average value from SEM images by analyzing at least 50 particles
[c] Particle length
[d] Particle diameter

3.3.1.2. Chemical Structure of HAp PEO-*b*-PMMA Nanoparticles

The FT-IR spectra (Figure 3.2) supported the synthesis mechanism through observation of the carboxyl absorption bands. As stated above, the reaction occurs in the center of a micelle, and this micelle is formed through an association between the ionized PMAA block formed at high pH and the calcium precursor ions. Therefore, changes in the carboxyl absorption bands of the PMAA block may be used to substantiate this mechanism. In the block copolymer spectrum, carboxyl groups were observed at 1705, 1575, and 1410 cm^{-1}. Following nanoparticle synthesis, the peak at 1705 cm^{-1} disappeared, and the other two peaks shifted to 1558 and 1390 cm^{-1}. These changes are consistent with ionization of carboxyl group and stabilization of this ionized state by the calcium ions during synthesis [105]. Also, the positions of phosphate (1096, 1035, 961, 603 and 563 cm^{-1}) and hydroxyl (3566 cm^{-1}) absorption bands in the nanoparticle spectra were similar to standard spectra for HAp, suggesting that the calcium phosphate phase formed during synthesis was HAp [105-108]. Additional absorption bands at 2921 and

1449 cm^{-1} resulted from C-H stretching vibrations in the block copolymer. Overall, the features in the FT-IR spectra indicated that block copolymer coated HAp was synthesized by this method.

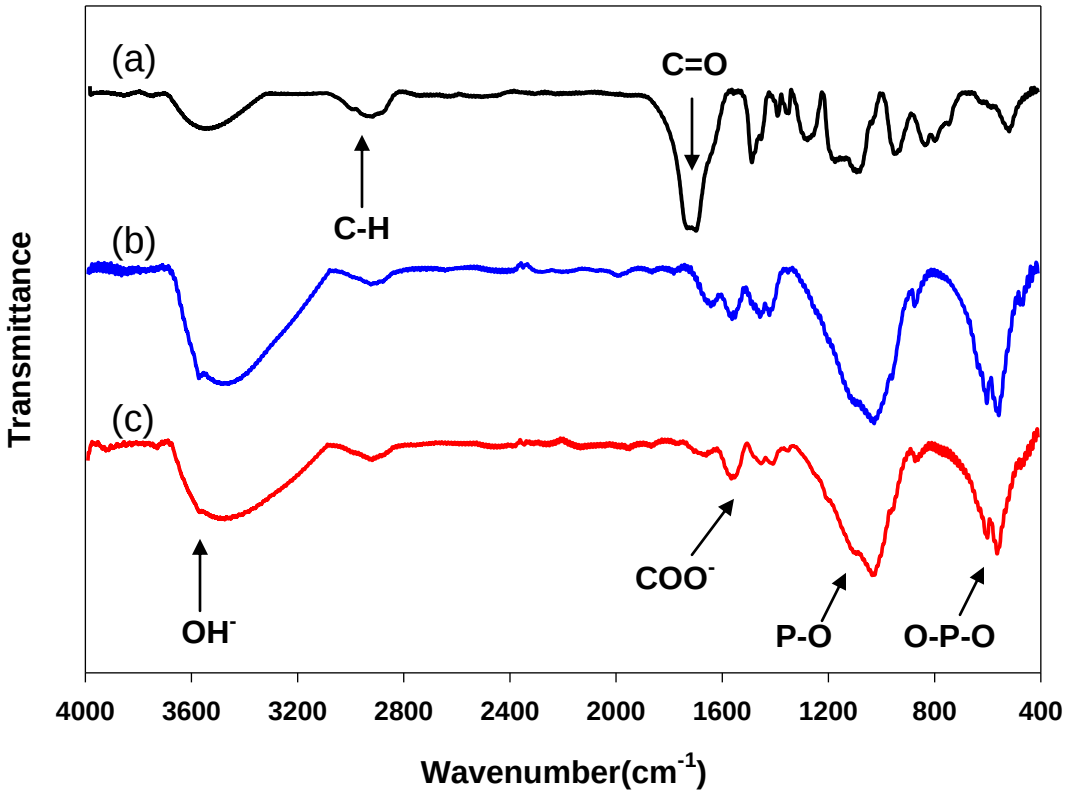

Figure 3.2. FT-IR spectra of the PEO-*b*-PMAA block copolymer (a), HAp PEO-*b*-PMAA needle (b), and HAp PEO-*b*-PMAA sphere (c).

3.3.1.3. Crystal Structure of HAp PEO-*b*-PMMA Nanoparticles

To verify that HAp was the calcium phosphate phase produced by the synthesis method, XRD experiments were performed on the particles. Figure 3.3 shows the powder XRD patterns of two selected HAp nanoparticles synthesized using the PEO-*b*-PMAA block copolymer. The XRD patterns show the presence of two different components. The block copolymer appeared as a broad diffraction peak at 18˚. All other peaks (25.9˚ (002), 28.2˚ (102), 29.2˚ (210), 32.2˚ (112), 34.2˚ (202), 39.9˚ (310), 46.7˚ (222), 48.2˚ (312) and 49.5˚ (213)) were consistent with the standard diffraction pattern for crystalline HAp, and the lattice parameters were similar to the standard file as well [109]. However, the crystallinity of the nanoparticles appeared to be low because the diffraction peaks were broad and diffuse. A lower level of crystallinity was expected since the synthesis was undertaken at low temperature and no additional calcination step was performed [63, 64]. Specifically, the XRD pattern of the synthesized HAp nanoparticles showed a broad peak at 32˚ which should be as three separate peaks at 31.9˚, 32.2˚, and 32.9˚ in highly crystalline HAp. To understand this structural aspect more fully, the crystallite size of the (002) and (310) diffraction were determined by Scherrer's equation [110]. The calculated crystallite sizes are listed in Table 3.3.

$$t = \frac{0.9\,\lambda}{B\cos\theta_B} \qquad (1)$$

where t is the crystallite size, λ is the X-ray wavelength, B is the full-width at half maximum (FWHM), and θ_B is the Bragg angle.

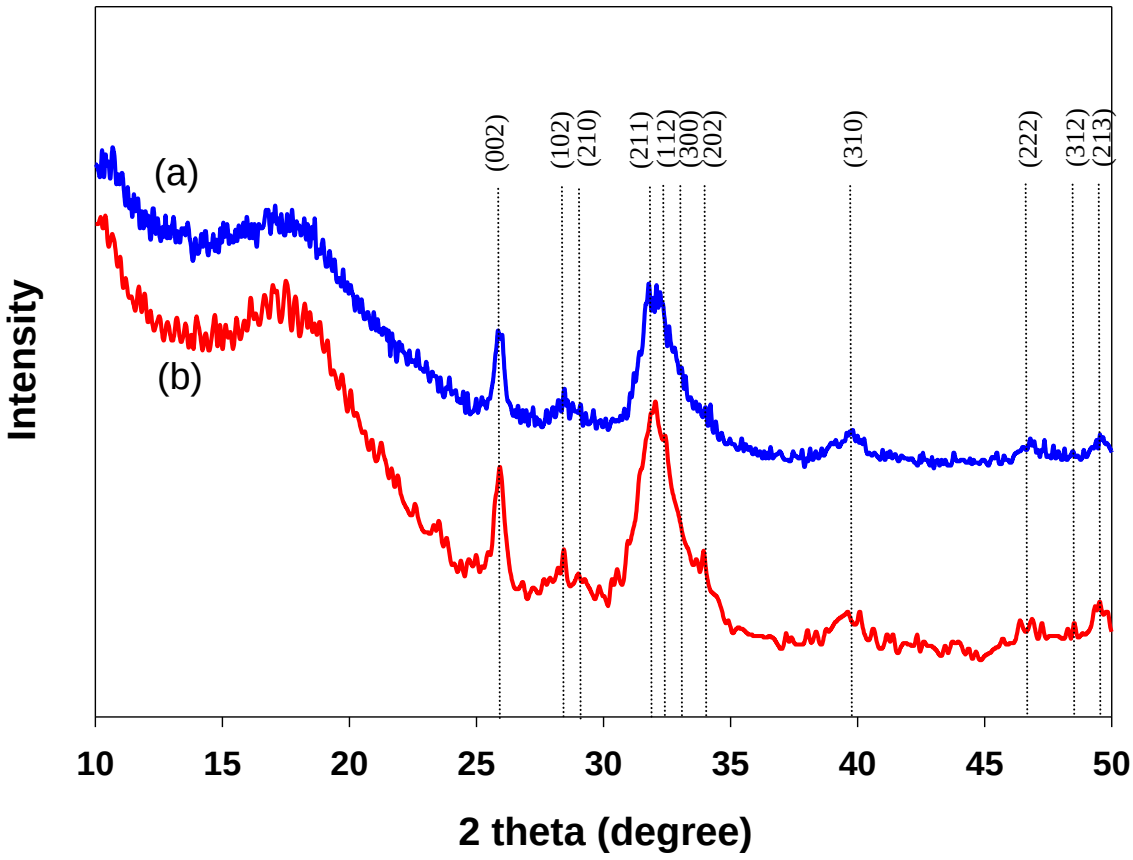

Figure 3.3. X-ray diffraction patterns of HAp PEO-b-PMAA needle (a), and HAp PEO-b-PMAA sphere (b). Lines denote the diffraction peak locations given in A.S.T.M Card no. 9-432 for HAp

Table 3.3. Crystallite sizes of HAp nanoparticles in the direction to 002 and to 310 planes.

Sample	D_{002} (nm)	D_{310} (nm)	D_{002}/D_{310}
HAp PEO-*b*-PMAA needle	21.8	8.0	2.7
HAp PEO-*b*-PMAA sphere	20.0	6.2	3.2

The results indicated that crystallite sizes along both directions decreased slightly as the block copolymer content increased. The value of the ratio of D_{002}/D_{310} for the HAp PEO-*b*-PMAA sphere nanoparticle was greater than that of HAp PEO-*b*-PMAA needle nanoparticles, indicating that the size reduction was greater in the direction orthogonal to the c-axis. This behavior was also observed in $CaCO_3$ and ZnO synthesis using PEO-*b*-PMAA block copolymer and attributed to PMAA preferentially adsorbed to crystal growth direction [71, 72]. In the study performed by Bigi *et al.* regarding HAp synthesis in presence of poly(carboxylates), the COO^- group influenced the HAp crystal growth. The results showed the COO^- group led to a reduction of the D_{002} and D_{310} and the reduction was greater in D_{310} direction. Thus, the COO^- group had interaction with inorganic surface, especially, along the direction orthogonal to the c-axis of HAp [111].

3.3.2. Synthesis of HAp using PMMA-*b*-PMAA Template.

3.3.2.1. Morphology of HAp PMMA-*b*-PMAA nanoparticles

In previous section, a new synthetic route for HAp nanoparticles using PEO-*b*-PMMA block copolymer was introduced. The block copolymer could be formed the micellar structure in water at high pH level (pH>11), and HAp nanoparticle synthesis

proceeded inside the micelle. In addition, the particle morphology was related to the relative concentrations of the calcium precursor and the block copolymer. In this section, the synthesis method was modified in order to use a PMMA-*b*-PMAA block copolymer, which is insoluble in water. Thus, tetrahydrofuran (THF) was used as a solvent for the block copolymer because it is miscible with both blocks. Scheme 3.2 shows the probable route for HAp synthesis using the PMMA-*b*-PMAA block copolymer. First, the aqueous solution of calcium precursor was added into the block copolymer solution and then adjusted pH of the solution to 9-10 using NH_4OH. At pH 9-10, the COOH group in PMAA block ionized into the COO^- group. The COO^- group was neutralized by Ca^{2+} ion, resulting in the complexation of Ca^{2+} with COO^- groups on PMAA blocks. Since the complex was insoluble in THF solution, we presumed micelle structures could be formed a similar structure with previous our research, and the micelle was composed of the PMAA blocks and calcium precursors in the center of the micelle and the PMMA forming the outer shell in contact with the THF. Then, further particle synthesis proceeded inside the micelle.

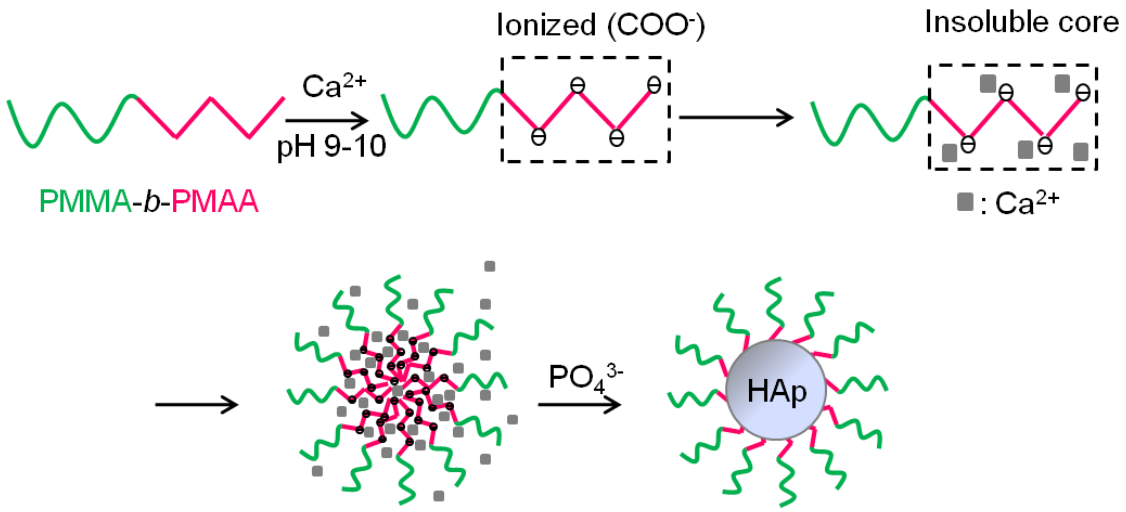

Scheme 3.2. Scheme for synthesis of HAp nanoparticles using PMMA-*b*-PMAA block copolymer template

Results from the previous section showed that the morphology of the HAp nanoparticles was related to the Ca^{2+}/COO^- mole ratio. In order to investigate the morphological change of the HAp nanoparticles in this synthesis system, six different synthesis conditions were examined by systematically changing the concentration of the block copolymer solution and the amount of precursor used in the synthesis. Again, the stoichiometric ratio of Ca/P in the synthesis was 1.67. As shown in Figure 3.4, two different shapes of HAp nanoparticle were synthesized from this synthesis scheme.

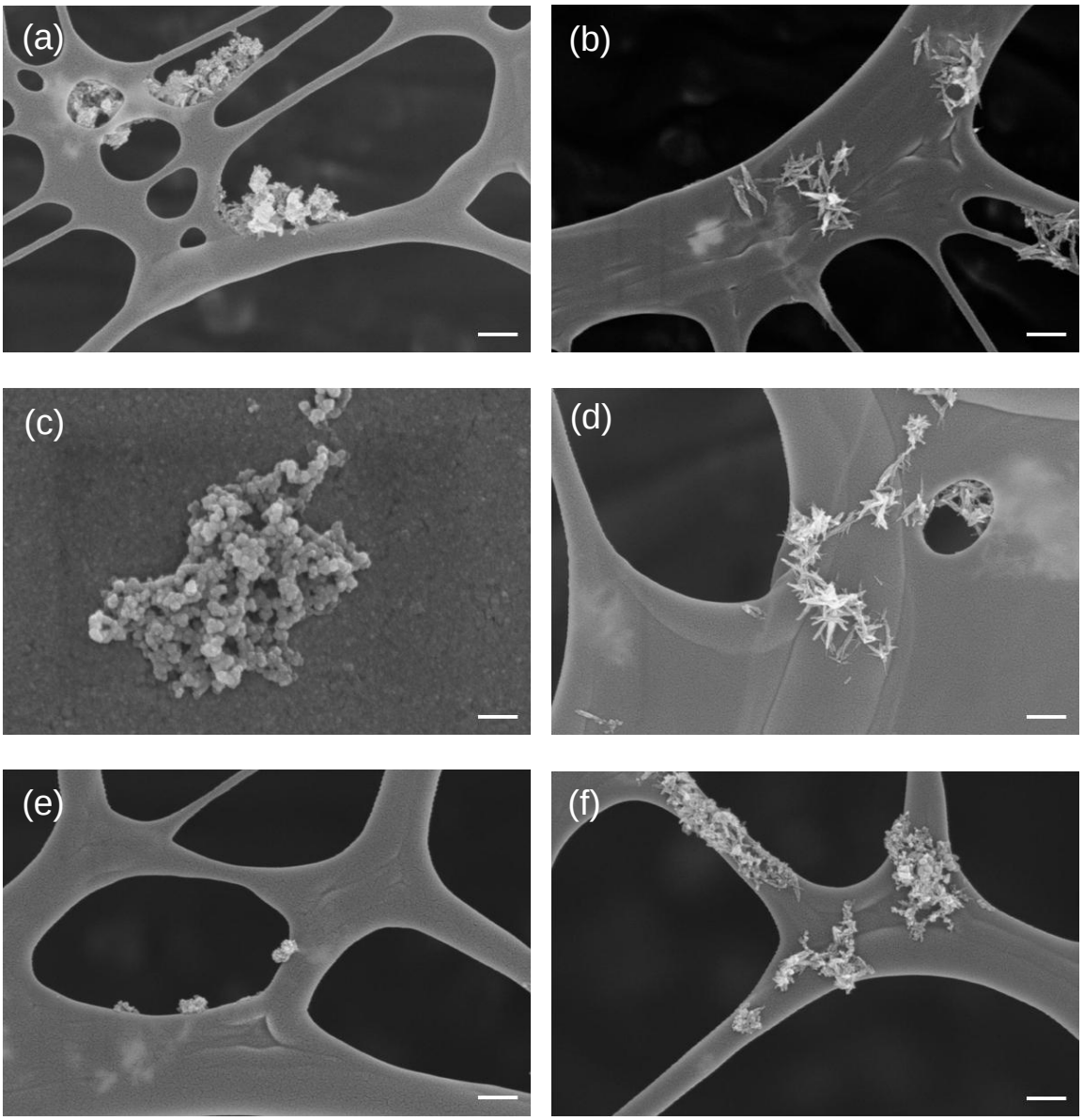

Figure 3.4. SEM micrographs of HAp particles synthesized with PMMA-*b*-PMAA solution concentration at 0.5 mg/mL with 200 µL (a), and 500 µL (b) precursors; PMMA-*b*-PMAA solution concentration at 1 mg/mL with 200 µL (c), and 500 µL (d) precursors; PMMA-*b*-PMAA solution concentration at 2 mg/mL with 200 µL (e), and 500 µL (f) precursors. The scale bars represent 300 nm.

Table 3.4 shows the particle morphologies corresponding to the mole ratio of Ca^{2+}/COO^-. The spherical particle morphology could be observed the mole ratios of Ca^{2+}/COO^- below 4.6 whereas the needle particle was formed at higher Ca^{2+}/COO^- mole ratios above 11.5. Compared with previous our study, the behavior was similar but the value of the mole ratio was increased. In addition, the mixed morphologies which contained with needle and spherical particles could be observed between the mole ratios. This behavior was attributed to the effect of organic solvent (THF). In this study, THF was used for the main reaction medium even though small amount of water was mixed, and the THF might influence somewhat different ionization of PMAA block or precursors. Several studies indicated the resulting particle morphologies were influenced by the degree of ionization of PMMA block [69, 70, 79].

Table 3.4. HAp nanoparticles shapes at different PMMA-*b*-PMAA concentrations and calcium precursors

Calcium precursor (μL)	PMMA-*b*-PMAA concentration (mg/mL)	$n_{Ca^{2+}}/n_{COO^-}$ [a]	Particle shape
200	0.5	9.2	mixed
	1	4.6	sphere
	2	2.3	sphere
500	0.5	22.9	needle
	1	11.5	needle
	2	5.7	mixed

[a] $n_{Ca^{2+}}$ and n_{COO^-} are the moles of Ca^{2+} ions and COO^- groups in PMMA-*b*-PMAA, respectively

In this research, two representative morphologies of HAp nanoparticle were used for further characterization. Figure 3.4 (b) and 3.4 (e) were selected samples for needle and spherical particle, respectively. The amount of block copolymer associated with two different shapes of HAp after recovering the particles from synthesis was measured with TGA, and the weight loss in temperature ranges between 100 and 650 is shown in Table 3.5. The result showed the amount of block copolymer associated with particle surfaces was increased as the block copolymer concentration used in synthesis increased. However, the amount of adsorbed block copolymer did not match with the amount used in synthesis.

Table 3.5. The contents of PMMA-*b*-PMAA on the HAp and the HAp particle size.

Sample	PMMA-*b*-PMAA concentration (mg/mL)	$n_{Ca^{2+}}/n_{COO^-}$	PMMA-*b*-PMAA (wt. %)[a]	Particle size (nm)[b]
HAp PMMA-*b*-PMAA needle	0.5	22.9	11.8	l[c]: 311 ± 36 d[d]: 46 ± 11
HAp PMMA-*b*-PMAA sphere	2.0	2.3	18.8	d[d]: 92 ± 10

[a] The value from TGA

[b] The average value from SEM images by analyzing at least 50 particles

[c] Particle length

[d] Particle diameter

3.3.2.2. Chemical Structure of HAp PMMA-*b*-PMAA nanoparticles

In order to investigate the chemical structure of the HAp nanoparticles, the FT-IR spectroscopy was employed. In Figure 3.5, IR spectra showed the characteristic peaks for the phosphate at 1096, 1035, 961, 603 and 563 cm^{-1}, and hydroxyl absorption band at 3566 cm^{-1} which were similar to standard spectra for HAp [105-108]. The spectra also showed peaks originated from the block copolymer. C-H bands in the block copolymer were observed at 2921 and 1449 cm^{-1}, and carboxylic groups were observed at 1730, 1558, 1390 cm^{-1}. In the block copolymer spectrum, carboxyl group were also observed at 1730 and 1410 cm^{-1}. Following nanoparticle synthesis, the peak at 1558 cm^{-1} newly appeared, and the other peak at 1410 cm^{-1} shifted to 1390 cm^{-1}. This is attributed to the ionization of COOH group in the PMAA block to COO^- group and the association between this ionized group and the calcium precursor ions. In addition, C=O band at 1730 cm^{-1} of block copolymer was broad since this peak was originated from PMMA and PMAA block. However, after particle synthesis, the peak was getting sharp because COOH group in PMAA block ionized into COO- group. Thus, the reaction occurred between the ionized PMAA block and the calcium precursor ions. Overall, the FT-IR results indicated that block copolymer-coated HAp was synthesized by this method.

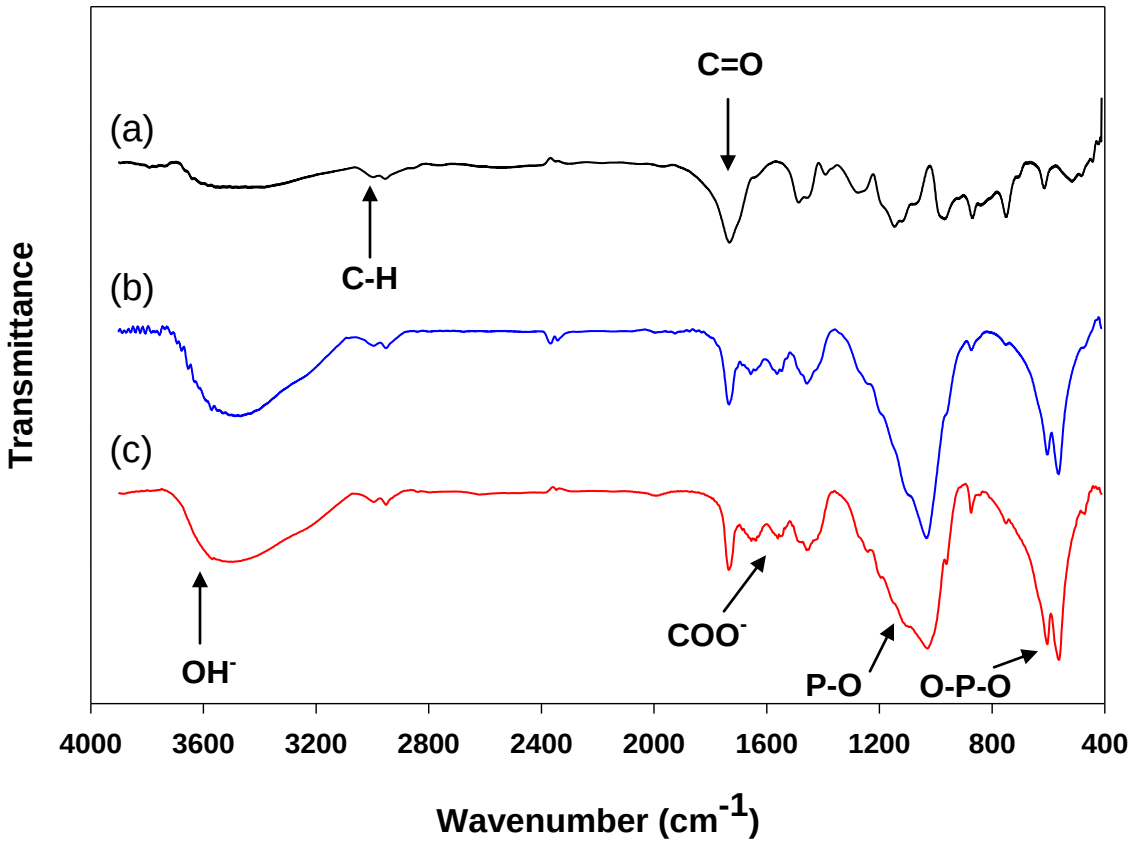

Figure 3.5. FT-IR spectra of the PMMA-*b*-PMAA block copolymer (a), HAp PMMA-*b*-PMAA needle (b), and HAp PMMA-*b*-PMAA sphere (c).

3.3.2.3. Crystal Structure of HAp PMMA-*b*-PMAA nanoparticles

To verify the chemical structure of HAp produced by the synthesis method, powder XRD measurements were carried out. The XRD patterns of two selected HAp particles were shown in Figure 3.6 and the diffraction patterns were the same with the previous section.

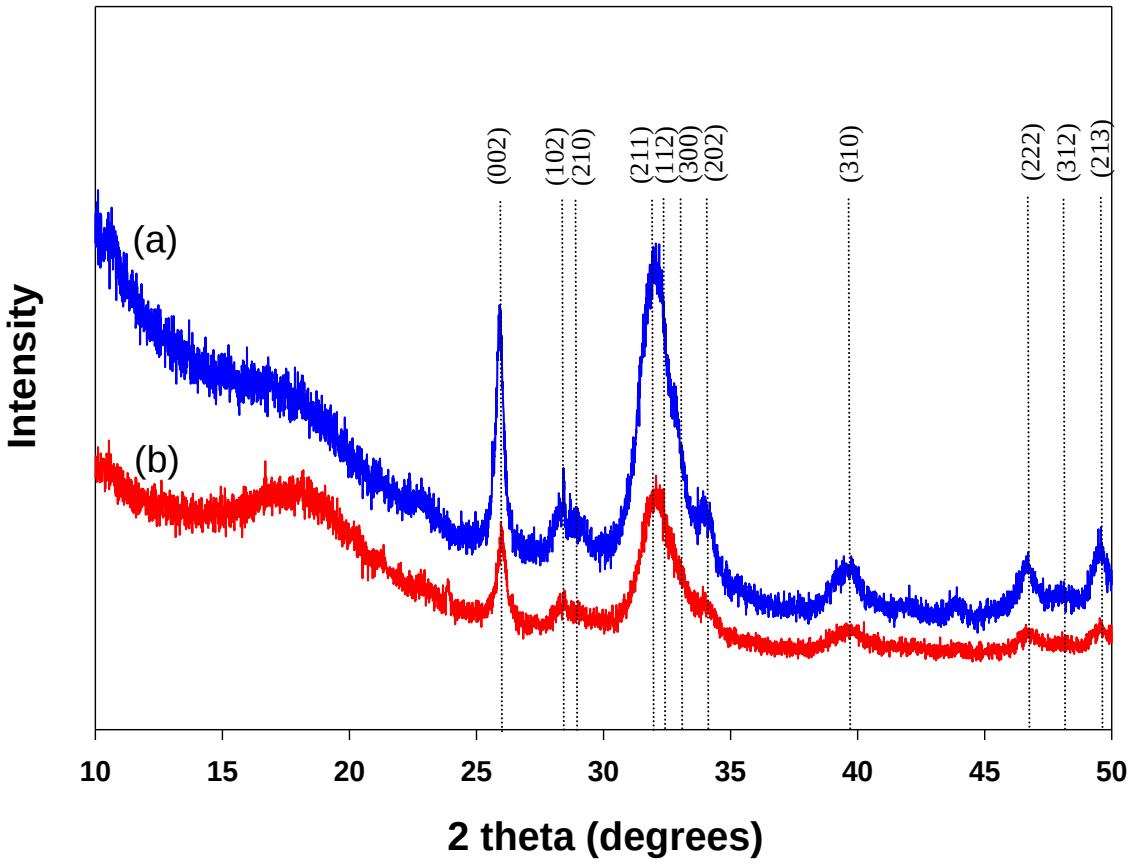

Figure 3.6. X-ray diffraction patterns of HAp PMMA-*b*-PMAA needle (a), and HAp PMMA-*b*-PMAA sphere (b). Lines denote the diffraction peak locations given in A.S.T.M Card no. 9-432 for HAp

In order to evaluate the effect of block copolymer on crystallite size, the crystallite size of two selected particle was calculated using Scherrer's equation. The crystallite size of the (002) and (310) diffraction were calculated and the values were shown in Table 3.6. The D_{002} is related to the mean size along the c-axis whereas D_{310} refers to the mean size along a direction perpendicular to it. The data showed that the increased block copolymer content induced a reduction of the crystallite size. The value of the ratio of D_{002}/D_{310} for the HAp sphere nanoparticle was greater than that of HAp

needle nanoparticles, indicating that the block copolymer appeared more affected along the direction orthogonal to the c-axis. Compared with XRD data from the previous section, the ratio of D_{002}/D_{310} for HAp PMMA-*b*-PMAA nanoparticles was increased. This behavior might be attributed to the effect of THF. As stated before, the THF might influence somewhat different ionization of PMAA block and particle morphologies were influenced by the degree of ionization of PMMA block [69, 70, 79]. However, overall behavior was similar with the previous results, and COO^- group had interaction with particle surface, especially, along the direction orthogonal to the c-axis of the HAp [71, 72, 111].

Table 3.6. Crystallite sizes of HAp nanoparticles in the direction to (002) and to (310) planes.

Sample	D_{002} (nm)	D_{310} (nm)	D_{002}/D_{310}
HAp PMMA-*b*-PMAA needle	25.1	8.0	3.1
HAp PMMA-*b*-PMAA sphere	22.8	6.4	3.6

3.4. Conclusions

In this research, block copolymer templates were used to synthesize HAp nanoparticles with a specific shape and surface treatment for future use in polymer nanocomposites. The results of this study indicated that the morphology of HAp nanoparticles can be directed by block copolymer concentration, specifically, by controlling the mole ratio of the calcium precursor and PMAA block of block copolymer (mole ratio of Ca^{2+}/COO^-) in both block copolymer systems. Compared with both block copolymer systems, overall morphological change behavior was similar, but morphological changes of HAp nanoparticles occurred at different ratios of Ca^{2+}/COO^-. In addition, mixed particle morphology containing spherical and needle particle could observe in PMMA-*b*-PMAA block copolymer system. This behavior was attributed to reaction media. Since water and THF were used as solvents for PEO-*b*-PMMA and PMMA-*b*-PMAA block copolymers respectively, the reaction media might influence different ionizations of PMAA block or precursors. Structural characterization of the nanoparticles showed that HAp was the calcium phosphate phase formed and supported the synthesis mechanism. The block copolymer remained on the nanoparticle surface was also confirmed by TGA analysis. Therefore, it was concluded that the block copolymer formed micelle structures through the reaction between COO^- groups in PMAA and Ca^{2+} ions and anchored on the HAp nanoparticle surface. The mechanism for the nanoparticle shape change of HAp was shown by XRD analysis. The crystallite size along (002) direction for PMMA-*b*-PMAA block copolymer system was greater than that of PEO-*b*-PMAA block copolymer system whereas the crystallite size along (310) direction had

similar values for both block copolymer systems. For both block copolymer systems, however, the crystallite sizes of both directions were reduced as the mole ratio of Ca^{2+}/COO^- decreased in particular the reduction of the crystallite size in (310) direction was greater than that of the (002) direction. Comparing the D_{002}/D_{310} ratio of the sphere and needle particle, the greater ratio value suggested a preferential adsorption of block copolymer on the HAp nanoparticle surfaces parallel to the c-axis. Comparing two block copolymer systems, overall morphological change behavior was related to the mole ratio of Ca^{2+}/COO^- . However, the crystallite size and the mole ratio associated with the transition from spherical to needle shape were slightly different between two systems since HAp PMMA-*b*-PMAA nanoparticles were synthesized in THF. Thus, THF might influence ionization of PMAA block or precursors, and two systems showed somewhat different crystal growth behavior.

CHAPTER 4

INVESTIGATION OF THE EFFECTS OF PARTICLE LOADINGS AND SHAPES ON ISOTROPIC NANOCOMPOSITE PROPERTIES

4.1. Introduction

Polymer nanocomposite materials have been widely studied as functional materials [112-115] as well as materials of fundamental interest [116-118] due to size scale effects on properties and polymer confinement effects. In both of these types of endeavors, the interactions at the nanoparticle-polymer interface play a pivotal role in establishing structure-property relationships. One key parameter investigated in these efforts is nanoparticle dispersion, since the desired spatial arrangement of nanoparticles in the polymer matrix is dependent on the desired nanocomposite property. Higher levels of nanoparticle dispersion are achieved in systems where nanoparticle-nanoparticle attraction is mitigated or nanoparticle-polymer compatibility is enhanced by chemical treatment [119, 120].

One mechanism for increasing the compatibility of the nanoparticle and polymer matrix is to coat the nanoparticles with a polymer following a “grafting from” or “grafting to” methodology. In the grafting from methodology, an initiator is attached to the particle and a polymer is synthesized at the nanoparticle surface by reacting with the attached initiator [121-128]. The grafting to methodology involves attaching an existing polymer chains to a nanoparticle through a chemical reaction between functional moieties

on the polymer and the nanoparticle [129-131]. These routes have been used to produce nanocomposites containing homogeneously dispersed nanoparticles [132-136] and nanocomposites with purposeful inhomogeneous nanoparticle dispersion [137]. The nanoparticle dispersion in a given matrix has been shown to be tied strongly to the ratio of length of the grafted chain to the length of the matrix (free) chain, and when the same polymer is used for the grafted and matrix polymer, the ratio may be simplified to their respective number average molecular weights. Nanoparticle dispersion has been shown to be homogeneous when the grafted chains are longer than the matrix chains. However, other research has shown that homogeneous nanoparticle dispersion may be obtained when the ratio has a value greater than 0.24 [138], and this behavior is attributed to an interfacial zone of different density than the bulk matrix polymer [139]. Other studies have attributed homogeneous nanoparticle dispersion at ratios less than one to kinetic effects [140-142], high nanoparticle surface curvature [143, 144], as well as low grafting densities [140, 145].

The morphology of the polymer can also play a role in the nanoparticle dispersion achieved [20, 146-148]. In semi-crystalline matrices, nanoparticle dispersion behavior is related to the nanoparticle's nucleating ability and the amount of crystallinity in the polymer. If the nanoparticle acts as nucleating agent, it should preferentially locate at the centers of the spherulites, with the surrounding crystal effectively isolating nanoparticles from one another, similar to the interfacial polymer in amorphous matrix nanocomposites. In some cases, this approach has also been shown to preferentially nucleate other polymer phases in matrices such as polypropylene [149, 150], poly(vinylidiene fluoride) [151, 152] and nylon 6 [153, 154]. If the nanoparticle does not nucleate polymer crystallinity, then

the nanoparticles are likely to locate in regions containing amorphous polymer chains. In this case, the amount of polymer crystallinity impacts the nanoparticle dispersion. As polymer crystallinity increases, the quantity of amorphous polymer decreases, resulting in less matrix volume capable of accommodating the nanoparticles. Additionally in matrices which achieve crystallinity levels beyond spherulite impingement, the amorphous polymer regions are arranged differently than in those at lower crystallinity levels, further hindering nanoparticle dispersion.

In this research, polymer-coated nanoparticles were combined with a semi-crystalline matrix to understand the efficacy of a polymer coating in promoting homogeneous nanoparticle dispersion at high loadings in a polymer matrix with relatively high crystallinity (approximately 70%). Specifically, nanoparticles decorated with a PEO coating were combined with a PEO matrix to form nanocomposites, and these materials were characterized for nanoparticle dispersion and nanocomposite properties. The nanoparticles were synthesized using an approach that would most closely follow the grafting to methodology, though with the polymer serving an additional role as a dispersed synthesis template. This system was chosen as a comparison to previous research results from this group where the impact of matrix crystallinity on nanoparticle dispersion and nanocomposite properties has been examined [95, 155-157]. In particular, those results have shown that as polymer crystallinity increases, the maximum nanoparticle loading that may be homogeneously dispersed decreases [95, 155]. However, the results of this research suggested that a kinetically-trapped, dispersed microstructure was achievable with a grafted polymer coating in semi-crystalline matrices. Additionally, sufficiently high nanoparticle loadings affected the crystallite size

and crystallinity of the polymer, indicating this materials design strategy provides opportunities for changing matrix morphology while preserving nanoparticle dispersion.

4.2. Experimental

4.2.1. Materials.

HAp/PEO nanocomposites were prepared using PEO-*b*-PMAA block copolymer-coated nanoparticles synthesized in Chapter 3 and a commercially available polymer. Two particle shapes were used: spherical and needle-shaped. Representative SEM images of spherical and needle-shaped HAp nanoparticles are shown in Figure 4.1. The matrix polymer, polyethylene oxide (PEO) (M_v=300,000 g/mol), was purchased from Aldrich and used as received.

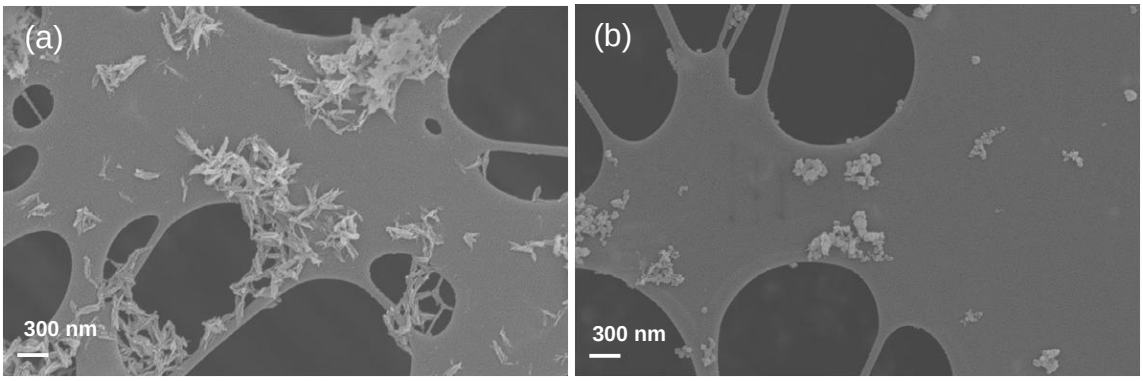

Figure 4.1. SEM micrographs of HAp particles synthesized with a PEO-*b*-PMAA template. (a) needle HAp, and (b) spherical HAp.

4.2.2. Preparation of HAp/PEO Nanocomposite Films

Scheme 4.1 illustrates the procedure for HAp/PEO nanocomposite preparation. Composite films with HAp loadings of 1, 5, and 15 wt. % were prepared by this method. First, the nanocomposite components were combined separately with water. PEO was dissolved in deionized water at 50 ˚C with a magnetic stirrer, and an aqueous suspension

of HAp nanoparticles was prepared using a bath sonicator for 10 min. Then, the PEO solution was mixed with the HAp dispersion to form a nanocomposite suspension using two steps: magnetic stirring for 30 min at room temperature and sonication with a cup horn sonicator at a power 80 W for 3 min. The dispersed mixture was cast into a polystyrene Petri dish and dried in a fume hood for 24 hr and then under vacuum for 4 hr. After casting, the samples were further consolidated with compression molding using a hot press at a force of five tons and at temperature of 80 ˚C for 10 min. The samples were cooled in the mold under pressure at a nominal rate of 15 ˚C min^{-1} using an integrated water cooling system. The resulting films had thickness of 0.1 mm. A neat PEO sample was processed using the same processing conditions for comparison.

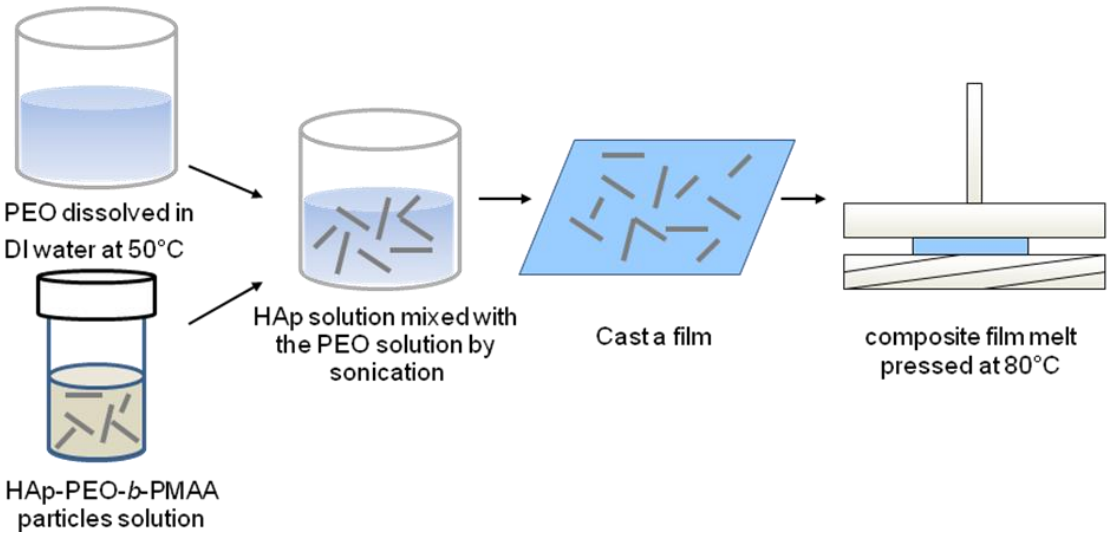

Scheme 4.1. Scheme for preparation of HAp/PEO nanocomposites.

4.2.3. Composite Morphological Characterization

The HAp/PEO nanocomposites were characterized for their particle dispersion and distribution using a LEO 1530 scanning electron microscope (SEM). Surfaces for imaging were prepared by cryo-fracture, and the fractured surfaces were coated with gold prior to imaging to prevent sample charging.

4.2.4. Rheology

The dynamic rheological properties were investigated using a TA AR2000 rheometer. All samples were tested at 90 ˚C. Test specimens with approximately 0.8 mm thickness were prepared by compression molding with the same conditions mentioned above. They were loaded onto 25 mm diameter parallel plates, and the gap was adjusted to 0.7 mm. All measurements were performed in the linear viscoelastic region. Dynamic frequency sweep tests were carried out in the frequency range of 0.02–50 s^{-1} at a strain of 0.1%. Two frequency sweep tests were performed on each material using different samples, and the average values were reported.

4.2.5. X-ray Characterization

The neat PEO and composite samples were characterized for matrix crystallite size using X-ray diffraction. The measurements were performed using a PANalytical X'Pert PRO Alpha-1 with Cu-Kα radiation (λ = 1.54 Å). The diffraction patterns were collected over a 2θ range of 10˚ to 50˚ with a step size of 0.01˚ and time per step of 20 seconds.

4.2.6. Thermal Analysis

The thermal transitions of the matrix were measured using a TA Q200 differential scanning calorimeter (DSC). The specimens were heated from -70 ˚C to 100 ˚C at a rate of 10 ˚C/min under a nitrogen purge. The melting and crystallization temperatures from the first and second runs were measured as the peak maxima. The matrix crystallinity was calculated by dividing the integrated heat of fusion by the heat of fusion of 100% crystalline PEO (H_f = 205 J/g) [158]. The heat of fusion for the composites was calculated considering the polymer mass only. The thermal transitions and the percent crystallinity were reported as the average value obtained from three separate DSC experiments with different samples.

4.2.7. Thermomechanical Analysis

Thermomechanical properties were measured using a Mettler Toledo DMA861^e dynamic mechanical analyzer (DMA). The DMA tests were performed in shear deformation using a double shear sandwich fixture with a stacked film sample. The stacked films were composed of two sample films, and each film was separated by an aluminum disk. The testing configuration used was based on a technical note from the instrument manufacturer [159]. Comparison DMA testing was conducted on the neat PEO in bulk form and stacked film configuration, and the results showed that the moduli were nearly identical for the two samples (APPENDIX A). All DMA tests were carried out in the temperature range from -75 ˚C to 25 ˚C with a heating rate 2 ˚C /min at a frequency of 1 Hz. All measurements were performed in the linear viscoelastic region.

Two temperature scan tests were conducted on each material using different samples, and the average value was reported.

4.3. Results

4.3.1. Dispersion and Distribution of HAp in Nanocomposites

The trends in nanoparticle dispersion and distribution were similar between the two nanoparticle shapes: spherical and needle-shaped. Figure 4.2 shows SEM images of the fracture surfaces from both nanocomposite systems at HAp loadings of 1, 5, and 15 wt.%. At a HAp loading of 1 wt.%, the particles were located in small aggregates in both composite systems, but the overall nanoparticle distribution appeared homogenous with no large scale phase segregation. At particle loadings of 5 and 15 wt.%, both nanocomposite systems appeared to have more homogeneous HAp particle dispersion and distribution in the PEO matrix.

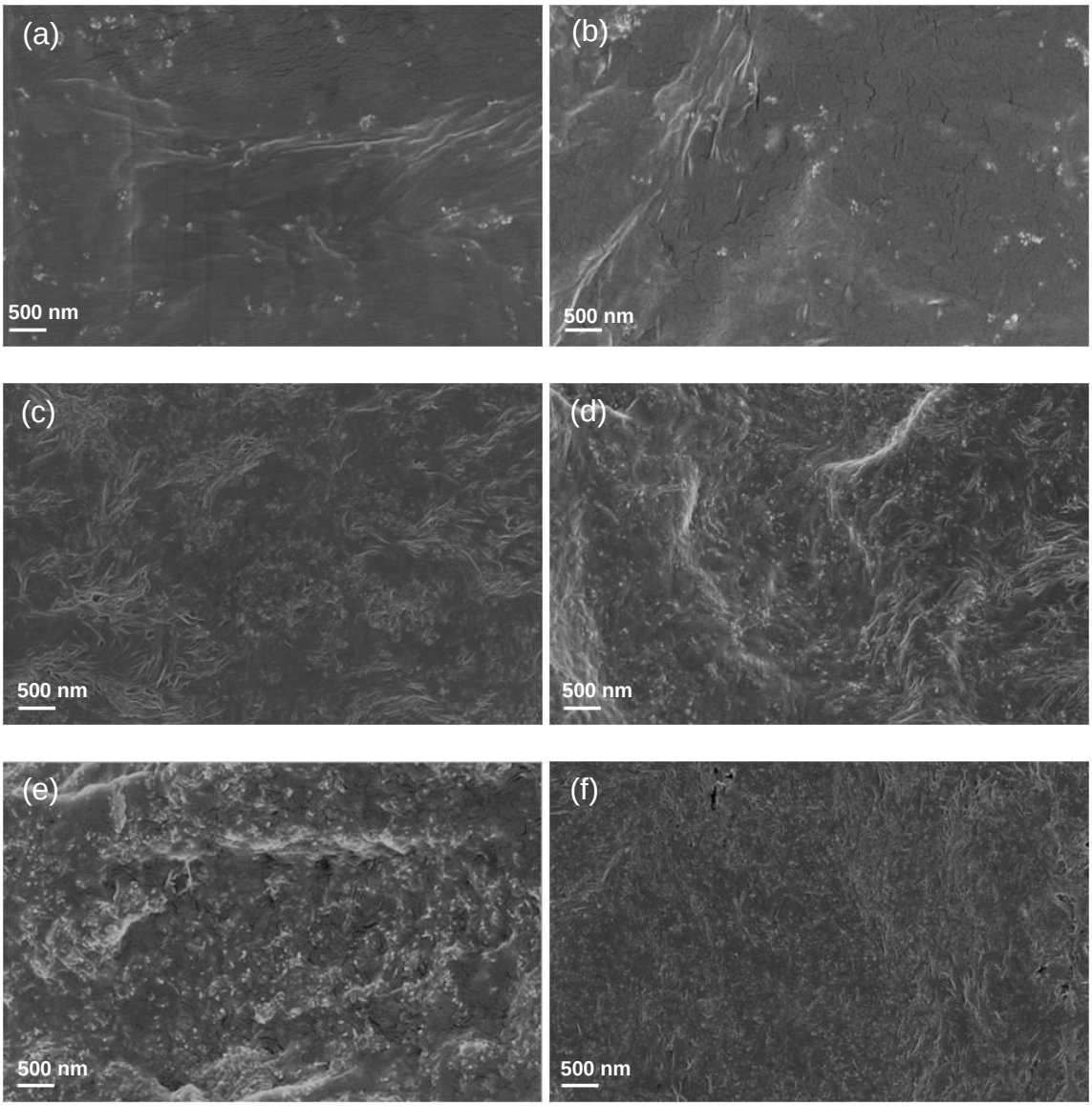

Figure 4.2. SEM micrographs of HAp particle dispersion and distribution. 1 wt. needle (a), 1 wt. % sphere (b), 5 wt. needle (c), 5 wt. % sphere (d), 15 wt. needle (e), and 15 wt. % sphere (f).

4.3.2. Rheology of Nanocomposites

The results of rheological experiments suggested that the nanoparticle arrangement in the PEO melt was similar in both nanocomposite systems at loading of 5 and 15 wt.%. The storage (G') and loss modulus (G") data are shown in Figure 4.3 for the neat PEO and both nanocomposite systems. The G' and G" data were used to evaluate reinforcement from the particles in the absence crystallinity and the transition from liquid-like (G'<G") to solid-like (G'>G") behavior. This transition is represented by the crossover frequency where G' and G" are equal. The neat PEO showed typical trends in G' and G" with terminal behavior at low frequencies and a transition from liquid-like to solid-like behavior at a frequency of 0.22 ± 0.01 Hz. The addition of spherical HAp particles of at a loading of 1 wt.% resulted in only small changes in the values of G' and G" and the crossover frequency increased to 0.32 ± 0.02 Hz. All other nanocomposite samples showed the expected trends in G', G", and crossover frequency. G' and G" were increased with nanoparticle addition and the crossover frequency was decreased. The decreased crossover frequencies in the nanocomposites with respect to the neat PEO were indicative of an increased elastic character due to larger reinforcement to G' than G". The crossover frequencies of the nanocomposites were: 0.08 ± 0.02 Hz for 5 wt.% spherical HAp, 0.16 ± 0.02 Hz for 1 wt.% needle HAp, and 0.04 ± 0.01 Hz for 5 wt.% needle HAp. At an HAp loading of 15 wt.% in both nanocomposite systems, the magnitude of G' was greater than G" at all frequencies tested in these experiments, so no crossover frequency was observed. Additionally, reduced frequency dependence of G' and G" were observed, consistent with solid-like behavior.

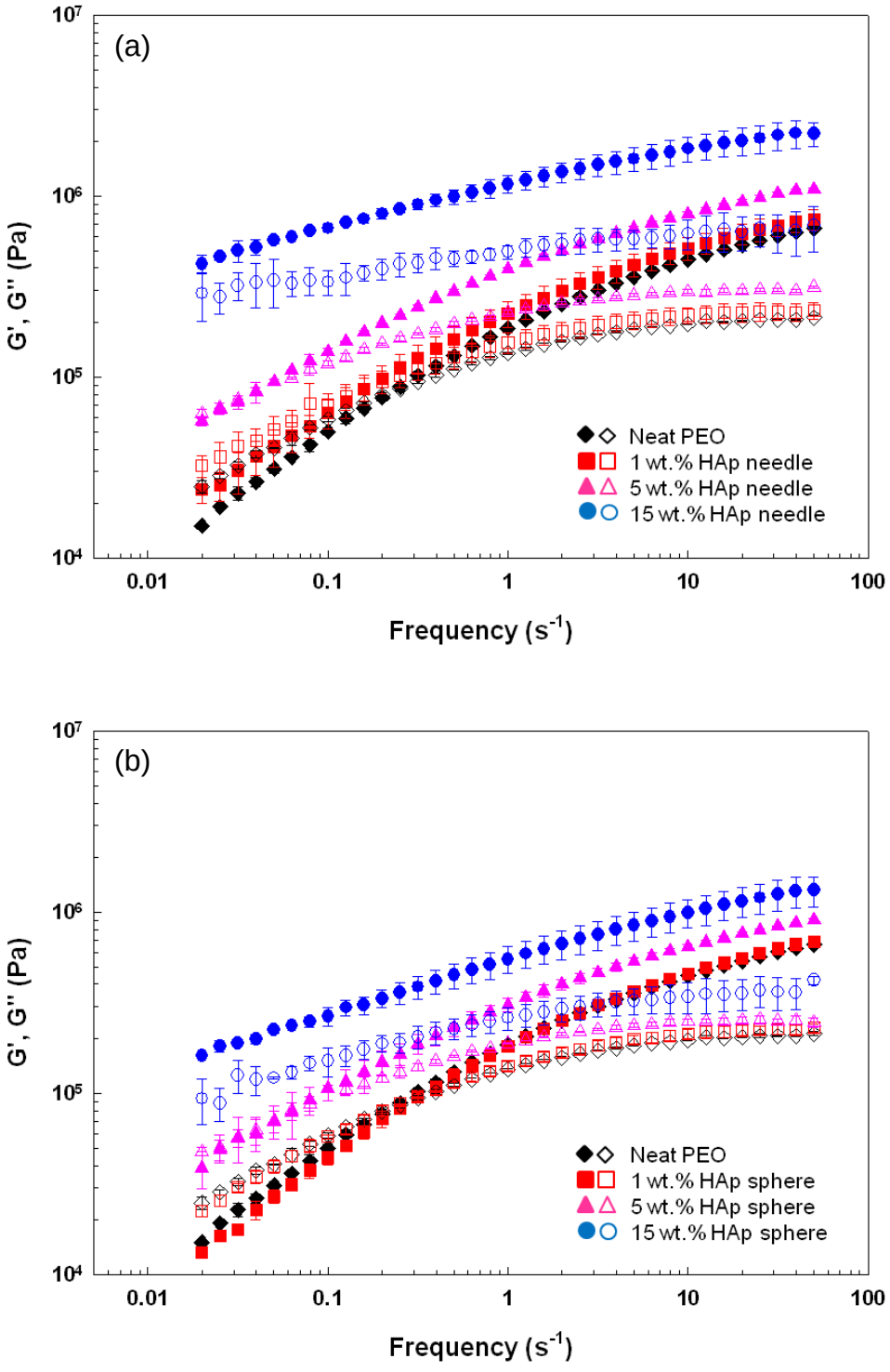

Figure 4.3. Modulus for the needle (a) and the sphere (b) nanocomposites. Filled and open symbols represent G' and G" respectively.

4.3.3. X-ray Diffraction of Nanocomposites

In the solid state, the addition of HAp nanoparticles did not change the crystal structure of PEO as shown by the x-ray diffraction patterns in Figure 4.4. The patterns for all of the nanocomposites and the neat PEO were similar, so only selected spectra are shown in Figure 4.4 for clarity. Four distinct peaks originating from the PEO were observed at 2θ values of 19.2°, 23.1°, 23.3°, and 23.5° corresponding to the (120), (-204), (032), and (-212) planes, respectively. The positions of these four peaks were similar among the samples, and no new peaks were observed. However, the polymer crystallite size was changed. Table 4.1 shows the crystallite sizes of the (120) plane obtained by using Scherrer's formula [160]. The crystallite size of HAp nanocomposites slightly decreased with an increasing HAp loading, indicating inhibition of crystal growth or disorder of crystal structure [161, 162].

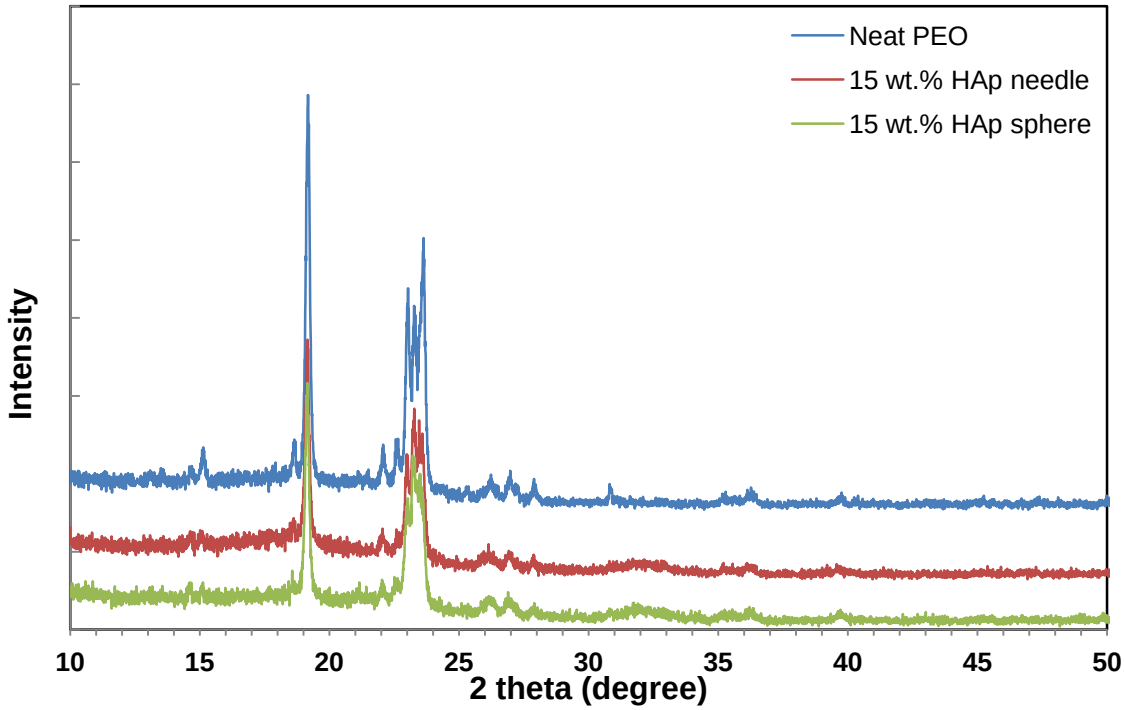

Figure 4.4. Representative X-ray diffraction (XRD) patterns of neat PEO and 15 wt. % HAp nanocomposites.

Table 4.1. Crystallite size of neat PEO and HAp composites of the diffraction (120) plane.

	Crystallite size (nm)
Neat PEO	46.9
1wt% HAp needle	47.1
5wt% HAp needle	46.1
15wt% HAp needle	43.4
1wt% HAp sphere	47.0
5wt% HAp sphere	46.1
15wt% HAp sphere	43.6

4.3.4. Thermal Properties of Nanocomposites

The thermal transition data obtained from DSC measurements agreed qualitatively with the X-ray diffraction data. As shown in Table 4.2, the addition of nanoparticles did not significantly influence the peak melting temperatures during the first and second heating cycle or the onset melting temperature measured during the first heating cycle. The maximum change was approximately -3 °C, but the melting temperatures did exhibit a decreasing trend as nanoparticle loading increased, consistent with the crystallite sizes calculated from the X-ray diffraction data since smaller crystals would melt at lower temperatures. Crystallization temperatures of the nanocomposites were also slightly decreased with a maximum decrease of 4 °C observed in the composites, indicating that these particles did not act as strong nucleating agents to the PEO matrix. The % crystallinity data for the nanocomposites relative to the neat PEO showed different trends. The PEO crystallinity in the needle and spherical particle

composites did not change up to 5 wt. % and 15 wt. %, respectively, but for 15 wt. % of needle particle system the crystallinity value dropped by 6 %. To understand if this decrease in crystallinity was related to the specific nanoparticle system or a more general phenomena associated with surface area or interparticle spacing, an additional nanocomposite containing 20 wt.% spherical HAp nanoparticles was processed and characterized by DSC. The % crystallinity of the PEO matrix in these composites was similar to those of the 15 wt.% needle particle nanocomposite, suggesting that the decrease in crystallinity was associated with a critical value of nanoparticle surface area or interparticle spacing.

Table 4.2. Crystallinity, melting, and crystallization temperature from DSC experiments.

	Crystallinity (%)		T_m (˚C)		T_m (˚C)	T_c (˚C)
	1st Heating	**2nd Heating**	**1st Heating**	**2nd Heating**	**Onset, 1st heating**	**1st heating**
Neat PEO	70	72	66	67	58	47
1wt% HAp needle	69	71	66	68	58	48
5wt% HAp needle	69	68	66	66	57	44
15wt% HAp needle	64	64	64	65	56	44
1wt% HAp sphere	71	72	66	67	57	47
5wt% HAp sphere	71	69	66	67	56	46
15wt% HAp sphere	71	70	65	66	55	43
20 wt% HAp sphere	61	63	63	66	54	42

* The spread in the experimental data was ≤ 1 ˚C for transition temperatures and ≤ 1 % for the crystallinity measurements.

4.3.5. Thermomechanical Properties of Nanocomposites

The DMA data showed the expected trends in G' and G" with nanoparticle addition, and the average DMA results for G' and G" are shown in Figure 4.5 and 4.6. The value of G' increased with HAp loading across the temperature range studies in both composite systems. The reinforcing efficacies of the two systems were similar at the same HAp loadings, and this result was attributed to the low aspect ratios of the nanoparticles used in this study as well as similar levels of particle dispersion and distribution in the two nanocomposite systems. The G" data shown in Figure 4.6 were used to assign T_g. All of the materials tested had a T_g of approximately -47 °C, and the experimental variation was within 1 °C.

In order to compare the reinforcement efficacies of both nanoparticle systems in more detail, the relative storage modulus (G_r') was calculated for the nanocomposite samples as shown in Figure 4.7. G_r' is the ratio of the nanocomposite storage modulus to the neat PEO storage modulus at a given temperature. All of the nanocomposites showed relatively constant G_r' at temperatures lower than T_g. At temperatures above T_g, G_r' showed greater temperature dependence, and the dependence increased as nanoparticle loading increased. The trend was not monotonic with temperature, but rather the G_r' data showed distinct reinforcement trends at different temperature intervals. These intervals were distinguished by changes in slope, indicating a different temperature dependence, and were defined approximately as T_g to -35 °C, -35 to -20 °C, -20 to 15 °C, and 15 to 25 °C. Beyond 25 °C, limited data was gathered in this study, so a temperature range beyond 25 °C is not defined.

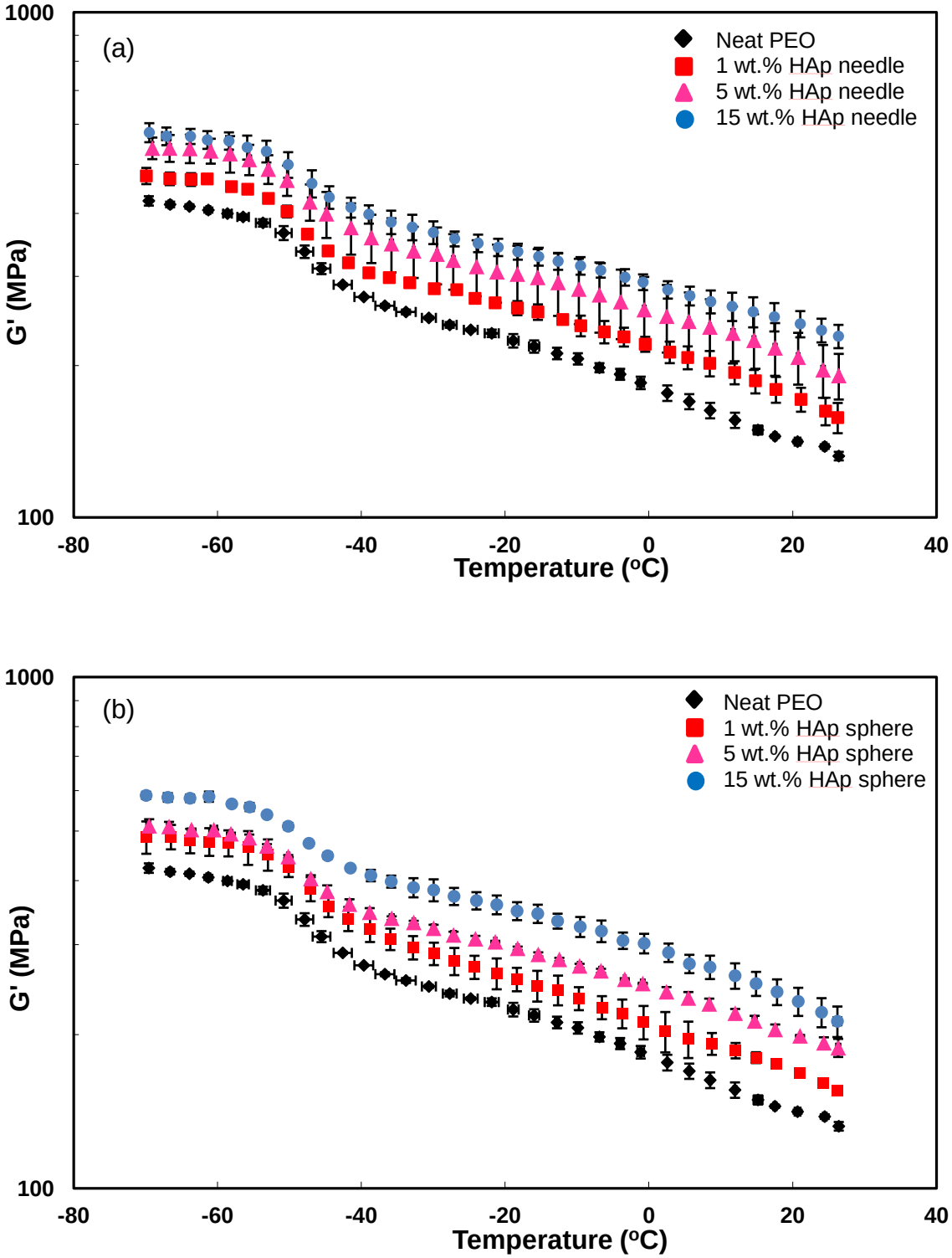

Figure 4.5. Storage modulus (G') for the needle (a) and the sphere (b) nanocomposites,

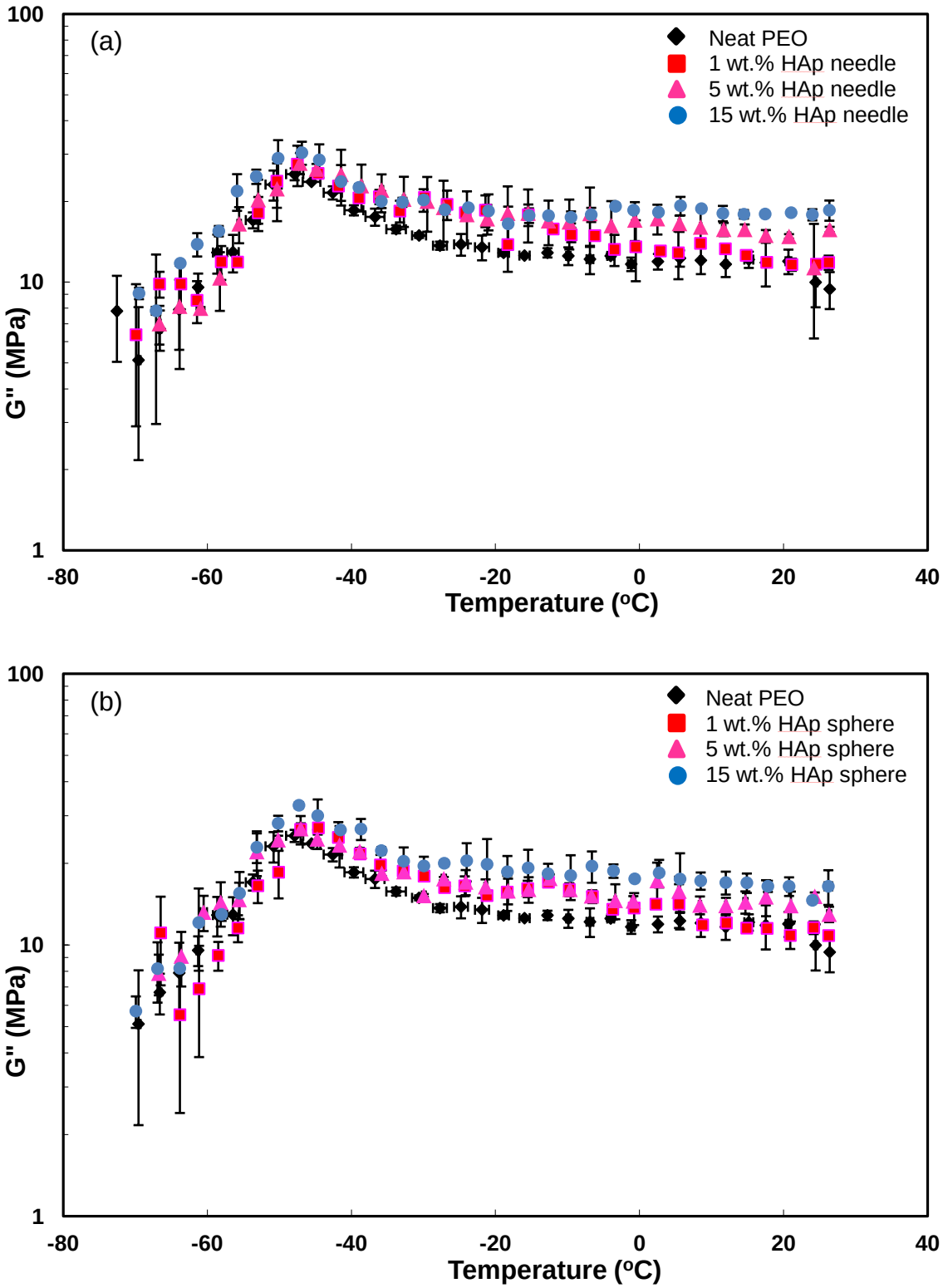

Figure 4.6. Loss modulus (G") for needle (a) and the sphere (b) nanocomposites

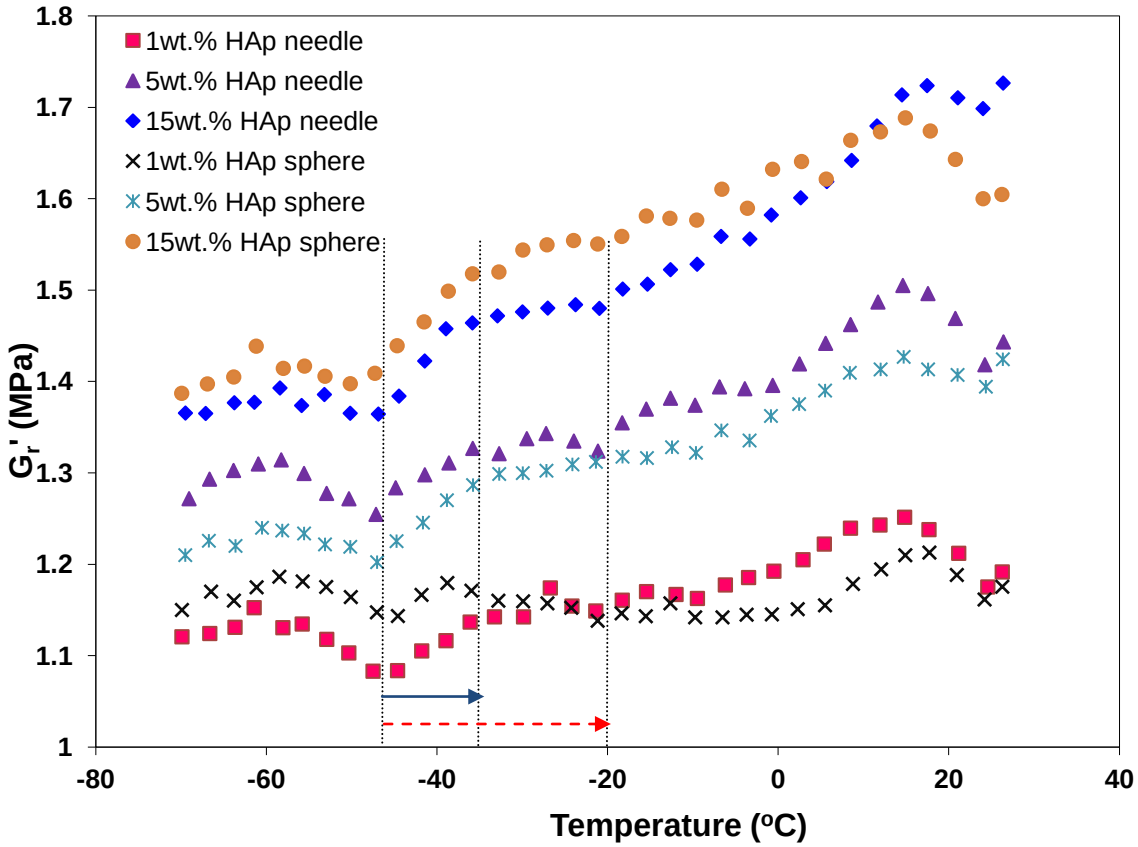

Figure 4.7. Relative modulus (Gr') data for HAp nanocomposites. (Solid line: the breadth (G") of composites, dash line: the breadth (G") of matrix)

4.4. Discussion

Nanoparticles cloaked in a copolymer coating were added to a matrix polymer with the same chemistry as the outer block of the copolymer coating. The coating was used with the goal of enabling homogeneous nanoparticle dispersion beyond low loadings in a matrix with a relatively high level of crystallinity. The ratio of grafted chain molecular weight to matrix chain molecular weight was quite low considering that the M_n of the grafted PEO block was 7,500 g/mol and the M_v of the polymer matrix was 300,000 g/mol. The M_n of the matrix would be lower than its M_v; however it is unlikely that the value of M_n could be low enough to achieve a ratio greater than 0.24. The grafting density of nanoparticles was also low. The values for the needle and spherical particles were 0.12 nm^{-2} and 0.37 nm^{-2}, respectively. For the HAp/PEO nanocomposites in this study, nearly homogeneous nanoparticle dispersion was achieved at loadings of 5 and 15 wt.% in both nanoparticle systems. As a comparison, the dispersion achieved with a nanocomposite containing 15 wt.% uncoated HAp nanoparticles prepared using the same processing method was imaged with SEM. These nanoparticles were prepared by a reverse microemulsion method and were elliptical in shape. The average major and minor diameters were 76 and 34 nm, respectively. Figure 4.7 shows SEM images of the two nanocomposites, and these images indicate that dispersion is improved with the interfacial polymer coating. Therefore, the dispersion trends seen in this research indicated that the copolymer coating was effective at preventing nanoparticle clustering in a matrix with a relatively high level of crystallinity. The differences in the dispersion behavior between the low nanoparticle loadings (1 wt.% of the spherical and needle

particles) and the higher loadings support the explanation that the microstructure was kinetically trapped. The nanocomposites with 1 wt.% HAp showed more aggregation than the higher loadings, and the rheology results indicate that the relative relaxation time of the 1 wt.% nanocomposites was similar to the neat polymer. The higher loadings showed shorter crossover frequencies, or relatively longer relaxation times. These longer times would lead to a persistence of the kinetically trapped condition in the composites with higher nanoparticle loadings. With regard to matrix morphology, the PEO nanocomposites showed decreased matrix crystallinity and crystallite size at high particle loadings. Both nanocomposite systems showed this result, but the decrease in crystallinity occurred at different nanoparticle loadings: 15 wt.% for the needle particles and 20 wt.% for the spherical particles. To understand if a common mechanism is responsible for decreasing crystallinity in the two systems, two general attributes of these composites were calculated and compared. First, the nanoparticle surface area available in both systems was calculated. The results indicated that the 20 wt.% spherical nanoparticle composite and the 15 wt.% needle nanoparticle nanocomposite had 4.1 and 4.3 m^2 of nanoparticle surface area per gram of composite material. These values are approximately equal and likely indistinguishable. Second, the interparticle spacing at these nanoparticle loadings was calculated by constructing a representative volume element as shown in Scheme 4.2 (not shown for the spherical particle system) and Equations 1 and 2.

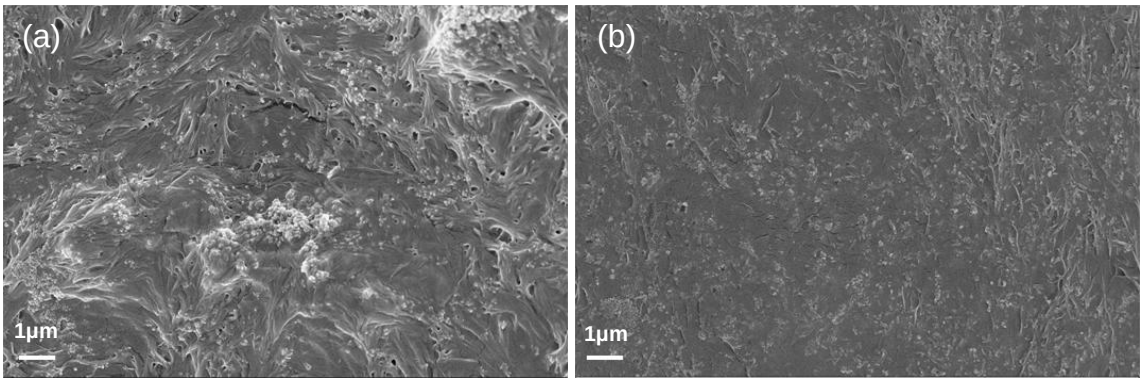

Figure 4.7. SEM micrographs of HAp particle dispersion and distribution. 15 wt. % of HAp uncoated sphere (a) and 15 wt. % of HAp PEO-*b*-PMAA sphere (b)

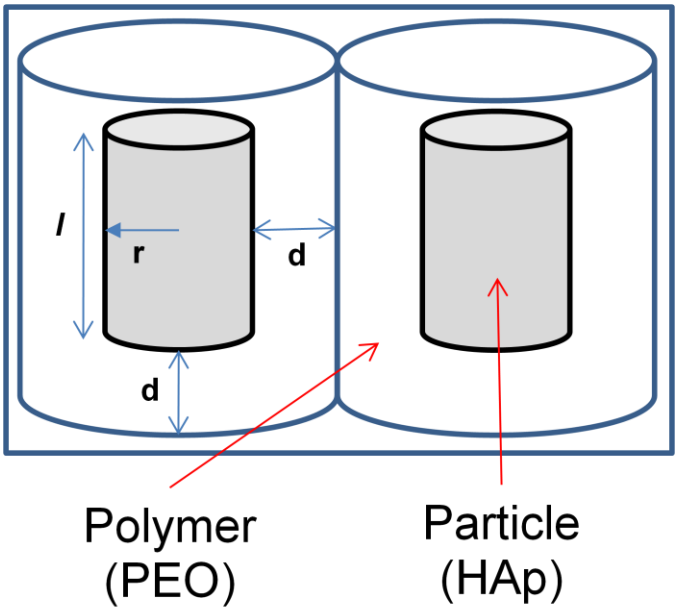

Scheme 4.2. The schematic model of HAp needle nanoparticles dispersion in PEO matrix

$$V_{\mathrm{PEO}} = \lfloor \pi(r+d)^2 \times (l+2d) - \pi r^2 l \rfloor \quad (1)$$

$$V_{\mathrm{PEO}} = \left\lfloor \frac{4}{3}\pi(r+d)^3 - \frac{4}{3}\pi r^3 \right\rfloor \quad (2)$$

Where r and d were the particle diameter of the HAp and PEO matrix thickness, respectively, and l was the particle length of needle particle.

Using these relationships, 2d values were calculated, corresponding to interparticle distances. From Tables 4.3, the matrix crystallinity of both particle systems was decreased and had similar values at an interparticle distance of approximately 120 nm at 15 wt.% needle nanoparticles and 20 wt.% nanoparticles. Therefore, both nanoparticle surface area and interparticle spacing could have influenced the matrix crystallinity.

Table 4.3.Interparticle distances

Particle loadings (wt. %)	Interparticle distance, 2d (nm)	
	Needle	Sphere
1	484	512
5	232	255
15	124	142
20	101	118

Based on the DMA results, the interaction between components was not strongly attractive or repulsive as evidenced by the negligible change in T_g with nanoparticle

addition in all of the composites studied here. This result further supports the claim that changes in polymer crystal structure resulted from the onset of physical confinement caused by decreasing average nanoparticle spacing. In terms of the viscoelastic behavior, the addition of nanoparticles increased G' with respect to the neat polymer. Restricting the analysis to the 5 and 15 wt.% nanocomposites since they showed similar dispersion behavior, the reinforcement levels seen in G' and G" did not scale directly with nanoparticle addition. If the G_r' values were normalized with respect to the nanoparticle loadings, then the reinforcement at 5 wt.% would be more efficient than that at 15 wt.%. However in the case of the needle particles, the matrix crystallinity was decreased with respect to the neat polymer which would also play a role in the mechanical reinforcement.

As mentioned in Results, the G_r' data did not show a continuous trend as a function of temperature. Generally, the reinforcement trends will be different at temperatures below and above T_g since the inherent matrix mobility is different at these temperatures [163-167]. This trend was seen in these nanocomposites, and in addition, the reinforcement above T_g showed four distinct behaviors. The first two were attributable to the difference in the breadth of the G" peaks for the nanocomposites and the neat polymer. As shown in Figure 4.5, the G" curves for all of the composites were similar in magnitude and shape. Above T_g, the loss modulus peaks were not as broad as the neat PEO due to the extra rigidity provided by the nanoparticles. The breadth of the nanocomposite G" peaks on the high temperature side corresponded to the temperature range of T_g to -35 °C. Similarly, the breadth of the neat PEO G" peak on the high temperature side spanned temperatures from T_g to -20 °C. The G_r' data as a function of temperature over the temperature ranges of T_g to -35 °C and -35 to -20 °C showed two

different slopes, consistent with these transitions. The slope between T_g to -35 °C was steeper than that between -35 and -20 °C, indicative of the greater change in polymer mobility in the lower temperature range. Between -20 and 15 °C, the slope increased again, exhibiting a larger temperature dependence. The change was more prominent in the nanocomposites containing needle particles, and above 15 °C, the G_r' data decreased as temperature increased, likely due to destruction of any interfacial zone present in the nanocomposites. These temperatures were quite a bit below the melting temperatures of the materials, so the decrease was not ascribed to onset melting.

Overall, the results of this research indicated that polymer-grafted nanoparticles could be dispersed at relatively high particle loadings in a matrix with 70% crystallinity. Therefore, the polymer coating was effective in preventing non-random clustering of nanoparticles in the amorphous regions of the matrix. The rheological testing and DMA results also suggested that the dispersed microstructure was likely non-equilibrium and an interfacial zone had developed at the grafted polymer/matrix polymer interface, respectively. Additionally, at sufficiently high nanoparticle loadings, the crystallite size and crystallinity of the polymer were affected as opposed to nanoparticle dispersion, indicating that this materials design strategy provides opportunities for changing the semi-crystalline morphology of the matrix.

4.5. Conclusions

In this research, two nanocomposite systems were processed and characterized using SEM, rheology, X-ray diffraction, DSC, and DMA. The nanocomposite systems were chemically similar but differed in nanoparticle shape. The experimental results indicated that the dispersion trends and thermomechanical properties were similar between the two nanoparticle systems due to their low aspect ratios and chemical similarity. However, the concentration of nanoparticles needed to restrict matrix crystallinity and crystallization was different in the two systems, but the behavior was unified through a common particle spacing of approximately 120 nm. Overall, these results further the understanding of general design guidelines in polymer nanocomposites with semi-crystalline matrices. This research indicated that clustering could be prevented up to high particle loadings in a matrix of similar crystallinity by low levels of polymer grafting. Since not all nanocomposite properties are optimized with a single microstructure, understanding materials design principles for these nanocomposites is important for their use in functional and structural applications

CHAPTER 5

CONTRUCTION OF HAp BUILDING BLOCKS INTO THE TENSEGRITY-INSPIRED MICROSTRUCTURES

5.1. Introduction

Polymer nanocomposites typically exhibited significant improvements in material properties over their neat polymer [5]. These improved properties were significantly related to surface area of nanoparticles, and much of the research has focused on controlling the particle dispersion into polymer matrices to increase interfacial area between nanoparticle and polymer matrix [9, 168-171]. Beyond fully dispersed particle morphology, research concerning a nanocomposites microstructure by controlling the particle arrangement has been studied to obtain the optimum material performance. For CNT nanocomposites, the alignment of CNTs in various matrices could be reinforced and enhanced the resulting composite properties of the desired nanocomposites [172, 173]. Some research have reported aligned CNT morphology could form a structural frame and electrical conducting path and achieve good load transfer the matrix to the CNTs as well as increase the electrical conductivity [174-176]. In addition, computational modeling studies have shown that nanoparticle arrangements can lead to greater increased in mechanical properties. [177, 178]

Several methods have been introduced to control particle arrangement in the polymer matrix including electrospinning, [179, 180] magnetic fields, [176, 181] shear flow, [28-31] block copolymer templating, [32, 34, 182] mechanical drawing [35-38]

and so on. Among them, the mechanical drawing process has been widely used to achieve aligned particle morphology.

In this research, the particle arrangement in polymer matrix was controlled by mechanical drawing process to construct tensegrity inspired microstructures comprised of nanoscale building blocks. Tensegrity structure was first introduced by Richard Buckminster Fuller. The meaning of tensegrity structure is synergistic structures consisting of isolated compression members that are connected by a tensile web [183]. Since the compression members were not directly connected each other and the structure has the ability to maintain an equilibrium state responsive to external mechanical stresses, the structure can be used to design light-weight and strong materials for applications such as antenna, sensors, and space telescope [44, 51, 52]. In order to create tensegrity-inspired structures in nanocomposites, the structure will be constructed through manipulation of the nanoparticles, interphase material and polymer matrix as shown in Figure 2.8 (Chapter 2). In this structure, the material containing the nanoparticles and the interphase material will be considered building block and the polymer matrix will be the tensile web for the tensegrity-inspired structure.

In Chapter 3, HAp nanoparticles were synthesized using block copolymer templates. Since these particles were coated with polymer blocks which were same chains as the matrix polymers, the decorated polymer blocks were considered as the interphase material which would be used to prestress the HAp nanoparticles and could facilitate particle dispersion in the matrix, and act as the building blocks for constructing tensegrity-inspired microstructure. The arrangement of the HAp nanoparticles was controlled by a mechanical drawing process. Specifically, the composite films were

drawn along two different directions in sequential steps. In this research, semicrystalline and amorphous polymer matrices were used for nanocomposite preparations and how nanoparticles interact with semicrystalline and amorphous polymer matrices was investigated. First, how the drawing process on influenced the particle arrangement in the both the semicrystalline and amorphous polymer was investigated. And then, the effect of particle arrangement on the nanocomposite properties was evaluated.

5.2. Experimental

5.2.1. Materials.

HAp nanocomposites were prepared using block copolymer-coated needle-shaped nanoparticles synthesized in Chapter 3. The matrix polymers, polyethylene oxide (PEO) (M_v=300,000 g/mol) and polymethyl methacrylate (PMMA) (M_w=120,000 g/mol), were purchased from Aldrich and used as received.

5.2.2. Preparation of HAp Nanocomposite Films.

The neat PEO and composite films with HAp loading 15 wt. % were prepared by Scheme 4.1 in Chapter 4. In order to arrange HAp nanoparticles in PEO matrix, the prepared films were drawn along two different directions in sequential steps as shown in Scheme 5.1. Film drawing was carried out at room temperature using Instron and TA Q800 dynamic mechanical analyzer (DMA). For the first drawing of film, a compressed film of 25 mm x 30 mm (width x length) was prepared and then drawn using Instron with crosshead speed at10 mm/min up to 30 % strain. After that, the sample was drawn in the perpendicular direction with respect to the first drawing direction using the DMA with crosshead speed at 10 mm/min up to 15 % strain. Those strains values were selected to prevent film failure.

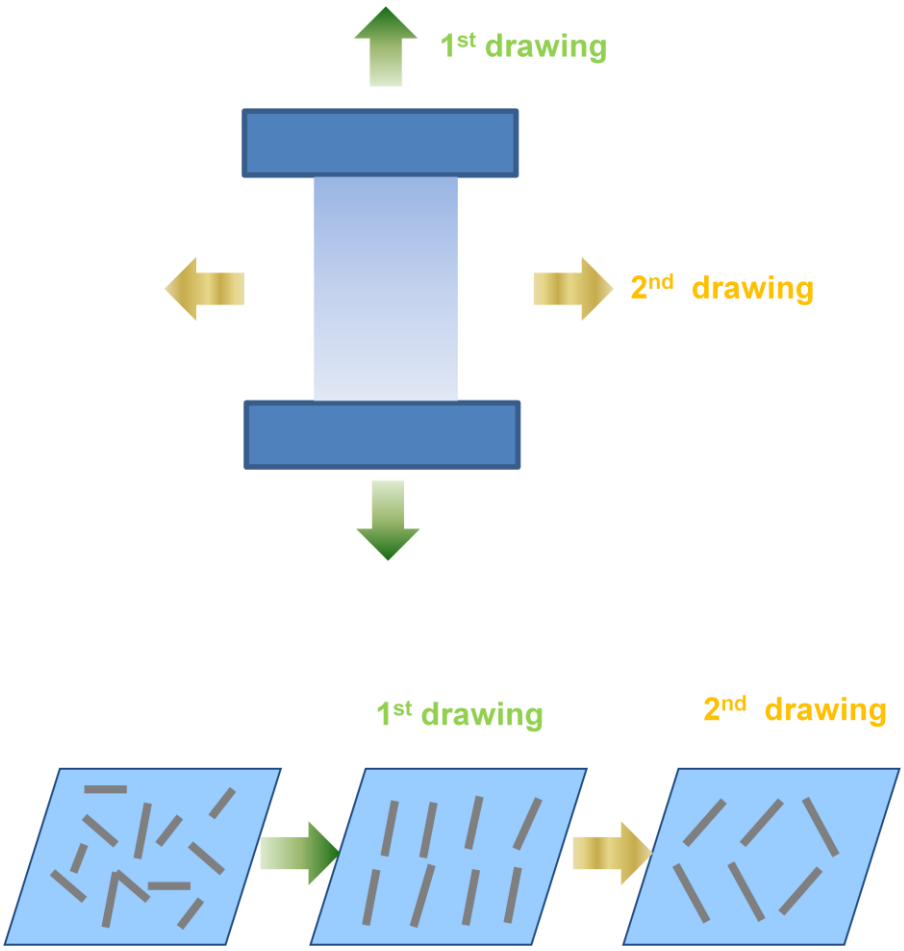

Scheme 5.1. Scheme of Mechanical drawing process.

In order to compare matrix morphology effects with semicrystalline polymer matrix nanocomposites, amorphous polymer matrix nanocomposite was prepared by Scheme 5.2. For preparing HAp/PMMA nanocomposite, a solution of matrix polymethyl methacrylate (PMMA) was prepared by dissolving in tetrahydrofuran (THF) at room temperature with a magnetic stirrer. Prior to mixing with PMMA solution, the HAp solution in THF was sonicated for 10 min using a bath sonicator. The HAp solution was mixed with the PMMA solution and prepared mixture with HAp loading of 15 wt. %. The mixture was dispersed with a magnetic stirrer for 30 min at room temperature and

then further dispersed using a cup horn sonicator with a power 80 W for 15 min to form the nanocomposite suspension. The suspension was then cast into a PTFE Petri dish which was partially covered with Al foil and left in a fume hood for 24 hr for the solvent to evaporate. The film was further dried using vacuum oven for 4 hr at 50 ˚C. The film sample for characterizations was molded using a hot press. The film sample was formed with a force of five tons and at temperature of 180 ˚C for 10 min. The press was then turned off and the film sample was cooled in the mold under pressure to room temperature. Prior to characterizing, the film sample was annealed under vacuum for 24 hr at 145 ˚C and then slowly cooled to room temperature to remove thermal history. The resulting film had thickness of 0.1 mm. A neat PMMA sample was processed using the same processing conditions for comparison. The drawn sample films (neat PMMA and 15 wt. % composite sample) were prepared using the same method with the PEO nanocomposite system except for the drawing temperature (for this system, the temperature was 120 ° C).

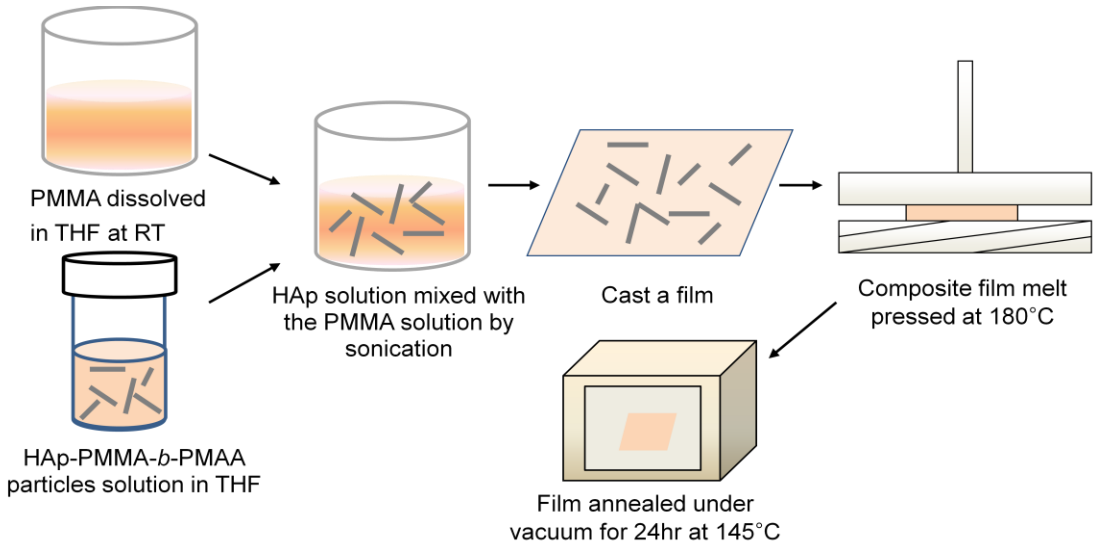

Scheme 5.2. Scheme for preparation of HAp/PMMA nanocomposites.

5.2.3. Composite Morphological Characterization.

The particle arrangements in the HAp nanocomposites for both systems were characterized using a Nova Nanolab 200 focused ion beam (FIB)/scanning electron microscope (SEM). The focused ion beam technique is able to remove materials by the physical sputtering action of ion bombardment. Thus, it has been widely used for the process of the sample surface and observation of processed sample surfaces [184, 185]. Prior to milling the samples, composite samples were coated with gold to avoid charging. A focused Ga^+ ion beam implantation of the samples was performed with a beam current of 0.3 nA for HAp/PMMA nanocomposites and 0.1 nA for HAp/PEO nanocomposites. After that, the milled surfaces were imaged using SEM.

5.2.4. X-ray Characterization.

The composite samples before and after drawing were characterized for HAp particle orientation using X-ray diffraction (XRD). For HAp/PEO nanocomposites, azimuthal scans were performed using a X'Pert MRD with Cu-Kα radiation (λ = 1.54Å). The diffraction patterns were collected azimuthal angles β = 0˚ to 360˚ at 32.9˚ (300) for HAp with a step size 0.05˚ and time per step of 10 seconds. For HAp/PMMA nanocomposites, X-ray diffraction measurements were conducted on a Rigaku R-AXIS IV equipped with an image plate. The Cu-Kα radiation (λ = 1.54Å) monochromatized by a confocal optics system was used and the diffraction patterns were collected β = 90˚ to 360˚ at 25.9 ° (002) for HAp. The sample setup for XRD measurement was shown in Scheme 5.3.

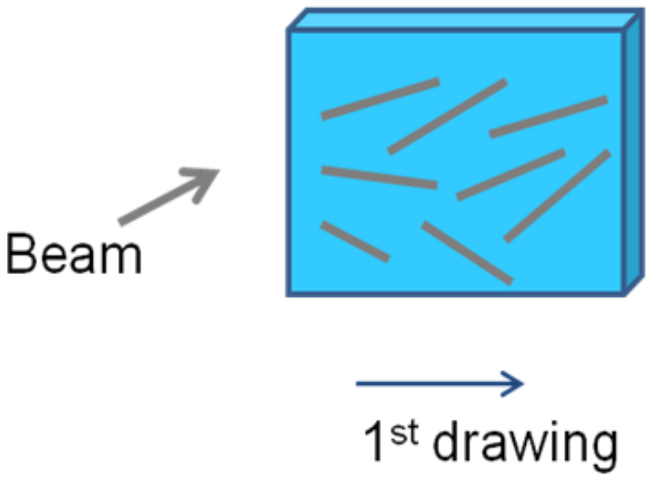

Scheme 5.3. Schematic representation of the sample preparation for wide angle X-ray diffraction (WAXD) measurement.

5.2.5. Thermal Analysis.

The thermal transitions were measured using a TA Q200 differential scanning calorimeter (DSC). The sample films for HAp/PEO nanocomposites were heated at a rate of 10 ˚C/min in the range from -70 ˚C to 100 ˚C under nitrogen gas flow. The melting and crystallization temperatures from the first and second runs were reported as the peak maxima. The crystallinity X_c of polymer was calculated from the following equation.

$$X_c = \Delta H_f / (w \Delta H_f^o) \quad (1)$$

where w is the weight fraction of PEO and ΔH_f^o is the heat of fusion of 100% crystalline PEO (205 J/g) [158].

The heat of fusion (ΔH_f) for the composite was obtained from integrating the melting peak of the heating cycle. The thermal transitions and the percent crystallinity were reported as the average value obtained from two separate DSC experiments with different samples.

5.2.6. Thermomechanical Analysis.

Thermomechanical properties were measured using a Mettler Toledo DMA861^{e} dynamic mechanical analyzer (DMA). All tests were performed in shear using a double shear sandwich fixture with a stacked film sample. The stacked films were composed of two sample films, and each film was separated by an aluminum disk. The stacked films were prepared with the same method described in Chapter 4. The tests for HAp/PEO nanocomposite system were performed in the temperature range from -75 ˚C to 25 ˚C and HAp/PMMA nanocomposite system was carried out in temperature range from 30 ˚C to 150 ˚C with a heating rate 2 ˚C /min at a frequency of 1 Hz. All measurements were carried out in the linear viscoelastic region with a limiting force and displacement amplitude condition. The average data was reported from two separate DMA tests using different samples of the same composition.

5.3. Results and Discussion

5.3.1. Morphological Characterization of Post-processed Nanocomposites.

To prepare HAp/PEO nanocomposites with controlled particle structures, the samples were stretched using Instron and DMA as shown in Scheme 5.1. Before drawing samples, the HAp nanoparticle loading was chosen based on the desired thickness of the PEO matrix polymer layer surrounding the HAp nanoparticle. The possible particle loadings were calculated according to the Equation (1) in Chapter 4. Table 5.1 shows the needle shaped HAp particle loading as a function of desired PEO matrix layer thickness. From this calculation, we selected 15 wt. % of HAp loading (interfacial thickness ≈ 60 nm) for nanocomposites preparation based on the radius of gyration of PEO matrix ($R_g \approx$ 30 nm) [186]. For HAp/PMMA nanocomposites system, the same particle loading was selected and nanocomposite sample was prepared to compare with HAp/PEO nanocomposites system.

A focus ion beam (FIB) technique was used for characterizing the arrangement and dispersion of HAp nanoparticles in polymer matrix. Figure 5.1 shows images of ion beam milled surfaces of nanocomposites with the isotropic, the first and second drawing. Using FIB, 100 x 100 x 1 μm^3 of volume was cut from composite samples and images were captured by SEM. The images show that the HAp nanoparticle had needle shape and well dispersed in the polymer matrix.

Table 5.1. The number of particle and weight percentage of HAp in PEO matrix

Interfacial thickness, d (nm)	**No. of particles, N**	**Wt. % of HAp**	**Interparticle distance, 2d (nm)**
10	5.42×10^{14}	71.1	20
20	2.25×10^{14}	50.5	40
30	1.26×10^{14}	36.5	60
40	8.13×10^{13}	27.0	80
50	5.64×10^{13}	20.4	100
60	4.12×10^{13}	15.8	120
70	3.12×10^{13}	12.4	140
80	2.43×10^{13}	9.9	160

For the isotropic samples, the images show that HAp nanoparticles had no preferential orientation, indicating randomly dispersed particle morphology. However, aligned particle morphologies could be observed in the drawn samples, especially, higher particle orientation was achieved in the first drawn HAp/PEO nanocomposite sample. The second drawing process did not significantly influence the particle arrangement, but the image shows some particles tilted toward the second drawing direction and lost the particle orientation. However, it is difficult to determine the particle arrangement from SEM images, so the alignment of HAp nanoparticles in the polymer matrix was further characterized using X-ray diffraction (XRD).

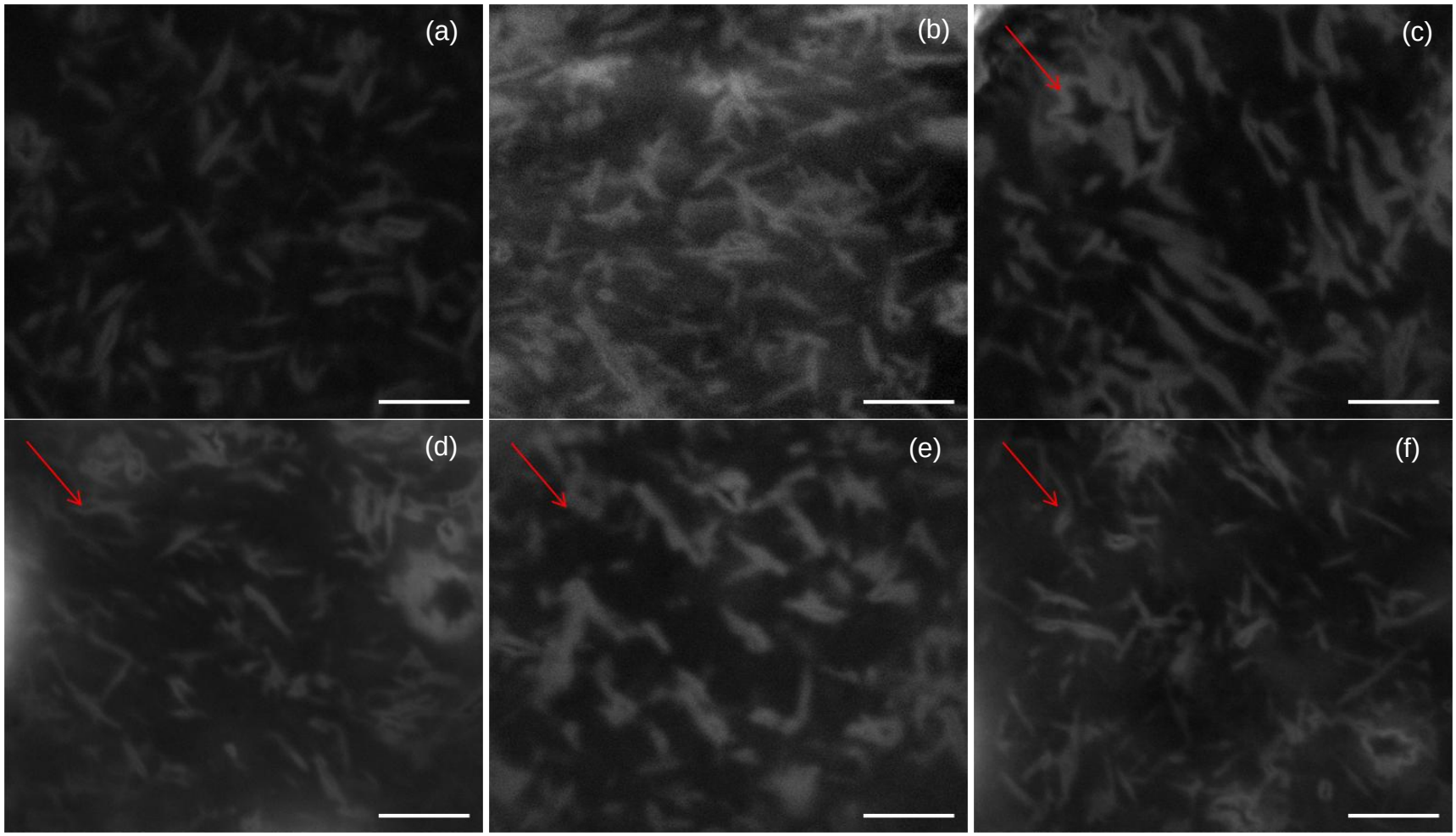

Figure 5.1. SEM micrographs. Isotropic HAp/PEO (a), HAp/PMMA (b), 1st drawn HAp/PEO (c), HAp/PMMA (d), 2nd drawn HAp/PEO (e), HAp/PMMA (f). The scale bar: 300 nm. The arrows indicated the first drawing direction.

5.3.2. X-ray Characterization of Post-processed Nanocomposites.

The X-ray diffraction (XRD) measurements were performed to evaluate the degree of orientation for HAp particles in polymer matrix. For HAp/PEO nanocomposites system, the diffraction angle of 32.9° corresponding to the (300) plane was selected to perform the azimuthal scan because diffraction pattern from HAp at 25.9° was overlapped with that from PEO. In order to evaluate the degree of orientation for HAp nanoparticles in PEO matrix, Herman's orientation function was employed using the HAp (300) plane. The orientation between the c-axis of HAp (parallel to the (300) plane) and the first film drawing direction was evaluated using azimuthal scan data of the HAp (300) plane according to Herman's orientation function [187]. Herman's orientation function is used for evaluating the degree of orientation for HAp nanoparticles, and the HAp nanoparticles are perfectly aligned when *f* is 1. For HAp/PMMA nanocomposites system, diffraction angle of 25.9° corresponding to the (002) was used to evaluate the degree of orientation for HAp nanoparticle in PMMA matrix.

$$f = \frac{3<\cos^2\theta>-1}{2} \tag{2}$$

where <θ> was the average angle between the c-axis of HAp and the first film drawing direction.

Figure 5.2 shows the results of the azimuthal scan of (300) diffraction plane for HAp/PEO nanocomposites. For the isotropic composite sample, no diffraction peak was observed from the azimuthal scan, indicating that the HAp nanoparticles had no preferential orientation. The (300) diffraction, which indicates the direction of the a-axis

of the HAp crystallites, for both drawing samples showed two distinct peaks at around 90° and 270°, and this result indicated long axis (c-axis) of HAp nanoparticles were preferentially oriented along the first drawing direction. The degree of orientation values, *f*, for the first and second drawing composite samples were 0.66 (FWHM: 27°) and 0.55 (FWHM: 34°), respectively. For the HAp/PMMA nanocomposites system, the results of the azimuthal scan of (002) diffraction plane were shown in Figure 5.3. The (002) diffraction plane indicated c-axis of HAp crystallite and the azimuthal scan showed two distinct peaks at 0° and 180°. The degree of orientation values were 0.15 (FWHM: 47°) and 0.1 (FWHM: 50°) for the first and second drawing, respectively. This result indicated the first drawn composite samples had higher orientation of HAp nanoparticles than second drawing samples. In addition, HAp/PEO nanocomposites system showed higher particle orientation from the drawing process. This behavior was attributed to matrix properties. The semicrystalline polymer matrix could induce the polymer chain alignment from drawing process. Under deformation particles located in the polymer matrix obtained a preferential orientation parallel to the drawing direction [36, 38]. Overall, compared with SEM images obtained from FIB-SEM, we presumed drawing process could facilitate particle arrangement.

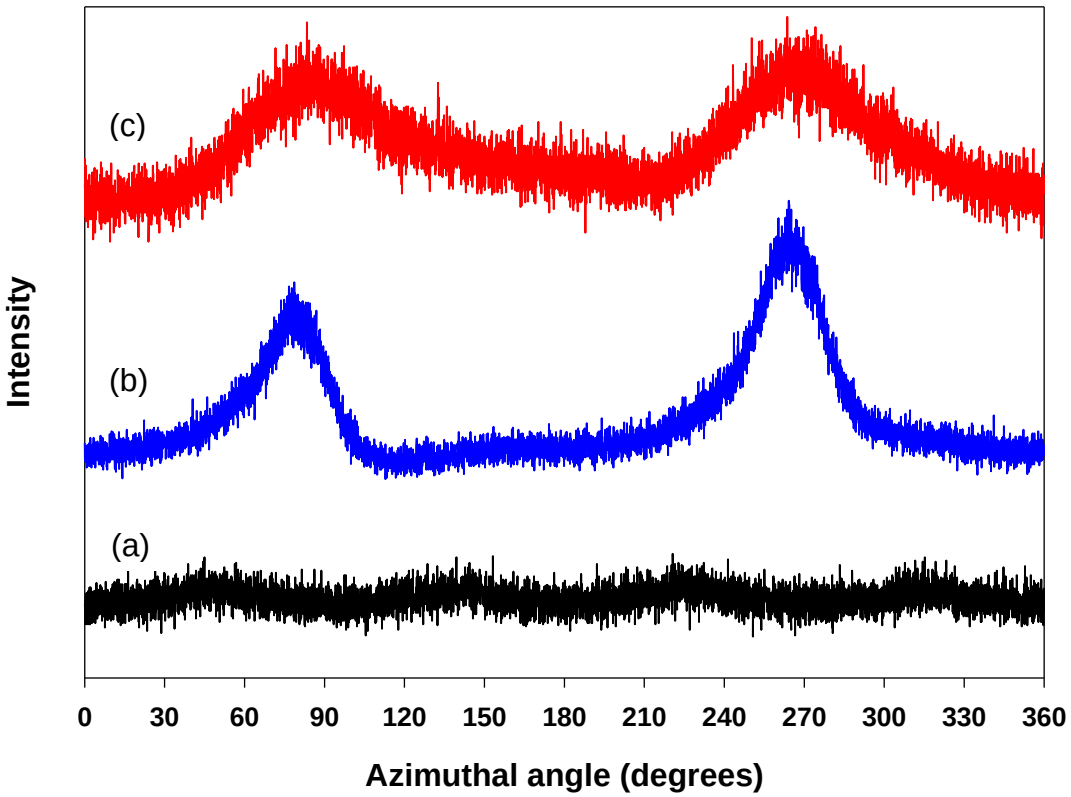

Figure 5.2. Azimuthal scan of (300) diffraction from isotropic (a), the first (b), and second (c) drawing HAp /PEO composites.

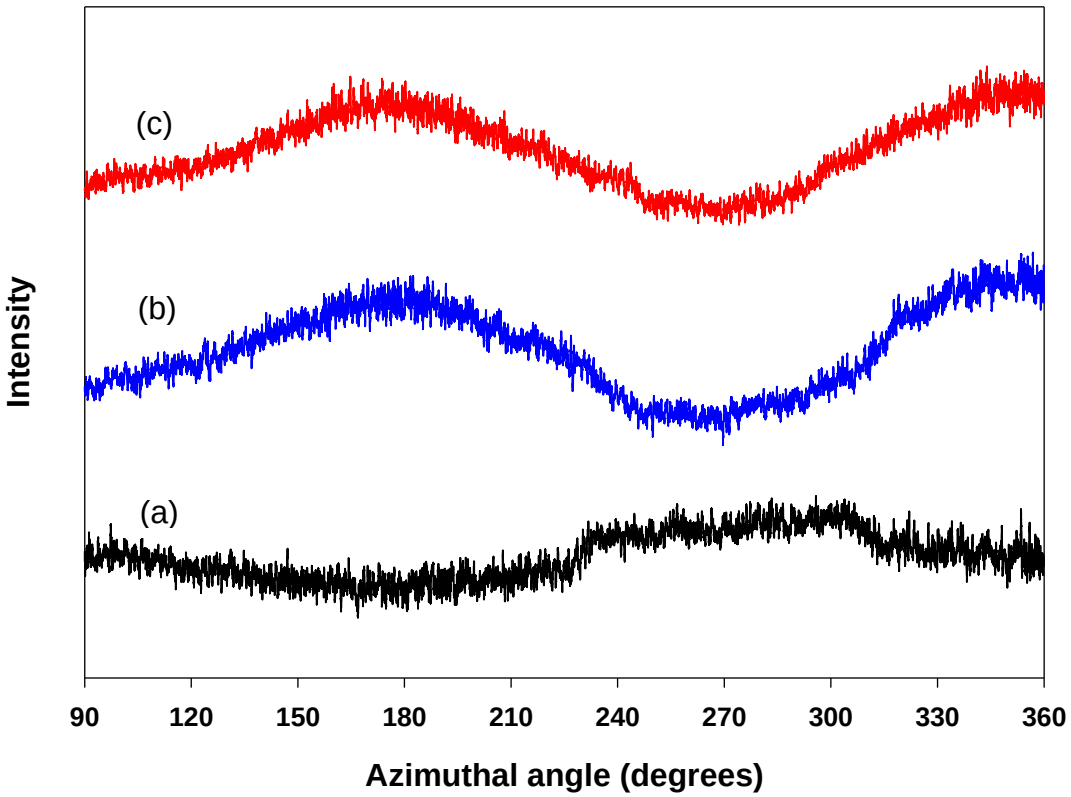

Figure 5.3. Azimuthal scan of (002) diffraction from isotropic (a), the first (b), and second (c) drawing HAp/PMMA composites.

5.3.3. Thermal analysis of Post-processed Nanocomposites.

Thermal transitions and crystallization behaviors for isotropic and drawn samples for neat PEO and HAp/PEO nanocomposites were measured using DSC. Table 5.2 shows thermal transition temperatures and crystallinity of isotropic and anisotropic HAp/PEO nanocomposites. The drawing process for neat PEO and HAp nanocomposites did not significantly influence the peak crystallization and melting temperatures during the first and second cycle. The change was approximately within 2 °C. For the neat PEO, the polymer crystallinity slightly increased during the first cycle. Some research has reported drawing process could be induced structural change of polymer matrix and influence thermal properties [188, 189]. This behavior was attributed to the stress-induced crystallization. In this study, we could observe only 2 % of crystallinity change. It might be associated with experimental error or the drawing process only influenced crystalline structure but not overall matrix crystallinity. However, for the HAp nanocomposite, the polymer crystallinity was increased after first drawing process. The effect of the second drawing process was negligible. The isotropic HAp nanocomposite sample had lower crystallinity than neat PEO and more available amorphous fraction which could convert crystalline fraction after drawing. Thus, for the HAp nanocomposite the stress-induced crystallization could be explained the increase polymer crystallinity. The effect of stress-induced crystallization was vanished during the second heating cycle and crystallinity for isotropic and anisotropic composite samples had similar value.

Table 5.2. The thermal transition temperatures and crystallinity of isotropic and anisotropic samples

	Crystallinity(%)		T_c (˚C)		T_m (˚C)	
	1st Heating	**2nd Heating**	**1st Heating**	**2nd Heating**	**1st Heating**	**2nd Heating**
Neat PEO	70 (0.6)	72 (0.5)	47 (0.3)	47 (0.4)	66 (0.3)	67 (0.1)
Neat PEO 1st	73 (1.7)	72 (1.3)	45 (1.1)	45 (1.0)	65 (1.3)	65 (0.4)
Neat PEO 2nd	73 (1.5)	71 (1.3)	46 (0.5)	46 (0.5)	65 (0.1)	65 (0.3)
15wt% HAp	64 (0.3)	64 (0.4)	44 (0.4)	44 (0.7)	64 (0.4)	65 (0.4)
15wt% HAp 1st	71 (2.0)	65 (3.3)	46 (0.1)	46 (0.0)	65 (0.0)	64 (0.1)
15wt% HAp 2nd	72 (2.1)	64 (2.3)	47(0.2)	46 (0.3)	65 (0.2)	64 (0.3)

5.3.4. Thermomechanical Properties of Post-processed Nanocomposites

In order to evaluate the effect of drawing process on the properties of neat polymer and HAp nanocomposite, the thermomechanical properties of samples were measured. The storage modulus (G') and loss modulus (G") of neat PEO and HAp nanocomposite as a function of temperature are shown in Figure 5.4. G' increased after drawing processes at all temperature ranges for both neat PEO and HAp nanocomposites. In order to compare the reinforcement efficacies, relative storage modulus (G_r') was calculated as shown in Figure 5.6. For neat PEO, the first and second drawn samples showed only small changes of G' at - 60 °C with respect to the isotropic neat PEO. For HAp/PEO composites, the modulus increased in the first and second drawn samples by 46% and 65%, respectively. In the rubbery region, the effect of reinforcement was more prominent than the glassy region for both systems. The first and second drawn samples for neat PEO showed 26% and 55% increase in G' at 15 °C, respectively, whereas the reinforcement for the first and second drawn HAp/PEO nanocomposites with respect to the neat PEO showed 239 % and 252%, respectively.

The G' and G" of neat PMMA and HAp/PMMA nanocomposite are shown in Figure 5.5. Comparing with HAp/PEO nanocomposite system, the drawing process on the neat PMMA did not significant influence the value of G'. As shown in Figure 5.6, the reinforcement efficacies increased in the first and second drawn HAp/PMMA nanocomposites with respect to the neat PMMA by 47 % and 57 % at 60 °C, respectively, whereas the reinforcement for the first and second drawn samples were 308 % and 240 % at 140 °C, respectively.

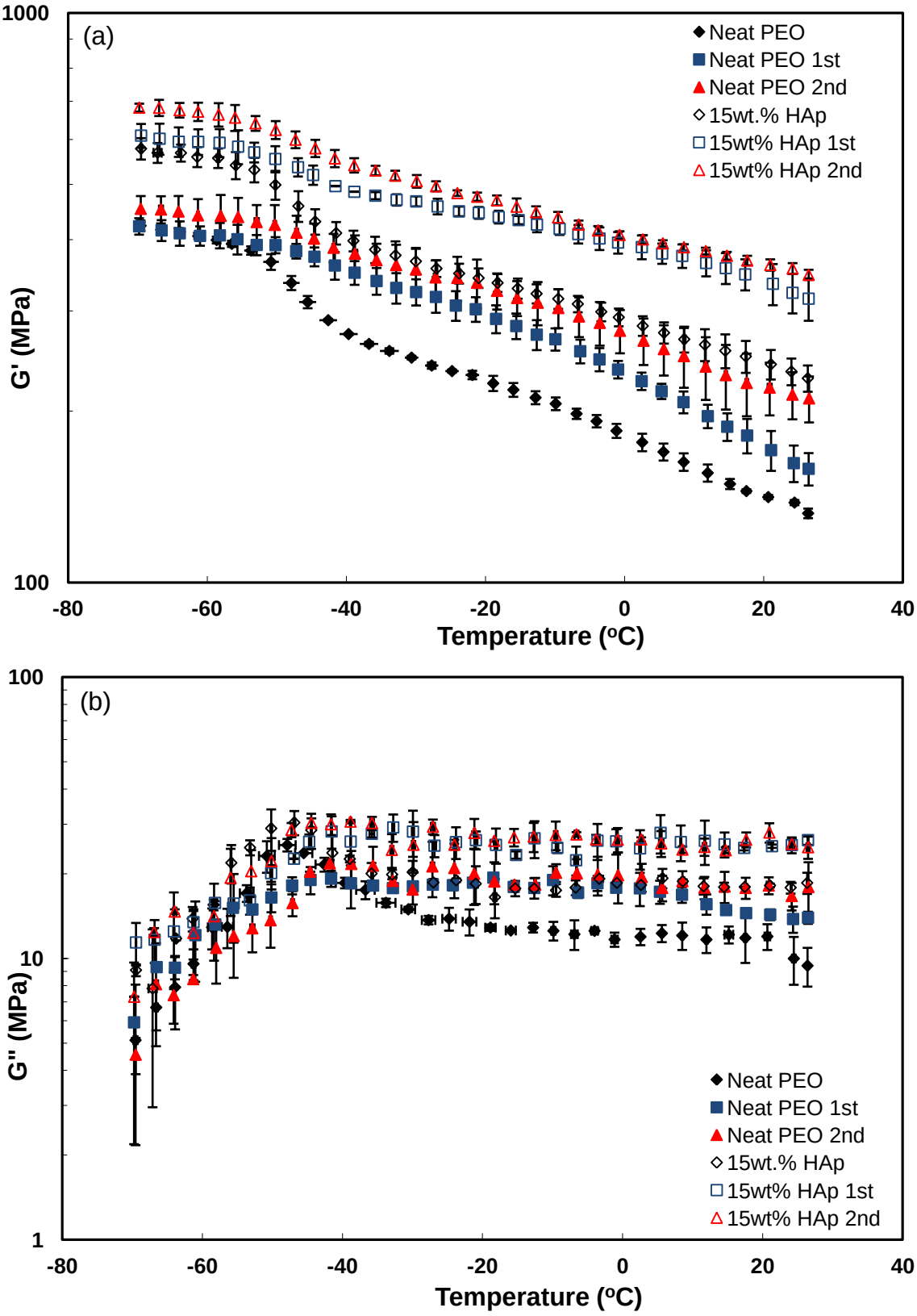

Figure 5.4. Storage modulus (a) and loss modulus (b) for neat PEO and HAp nanocomposite.

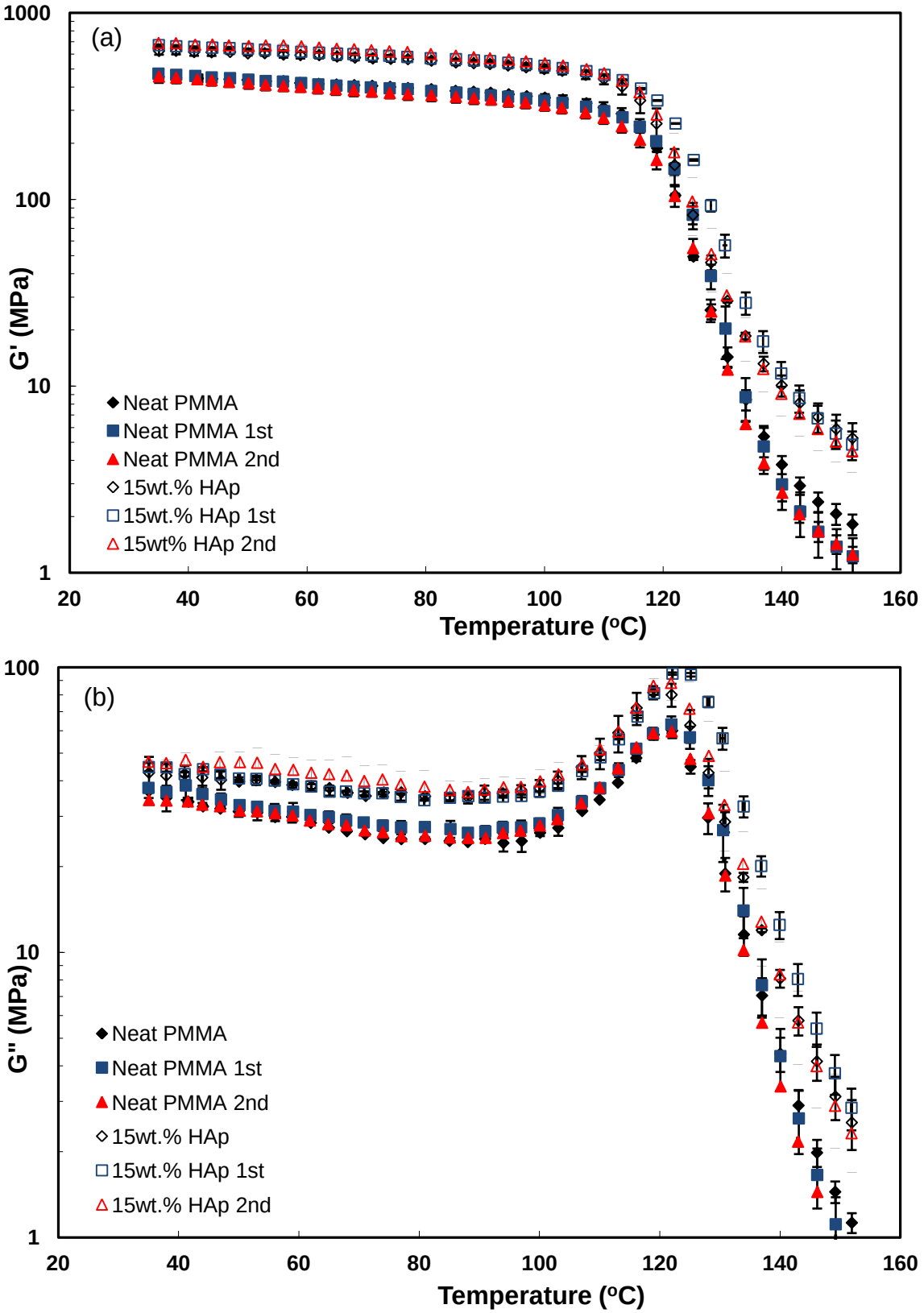

Figure 5.5. Storage modulus (a) and loss modulus (b) for neat PMMA and HAp nanocomposite

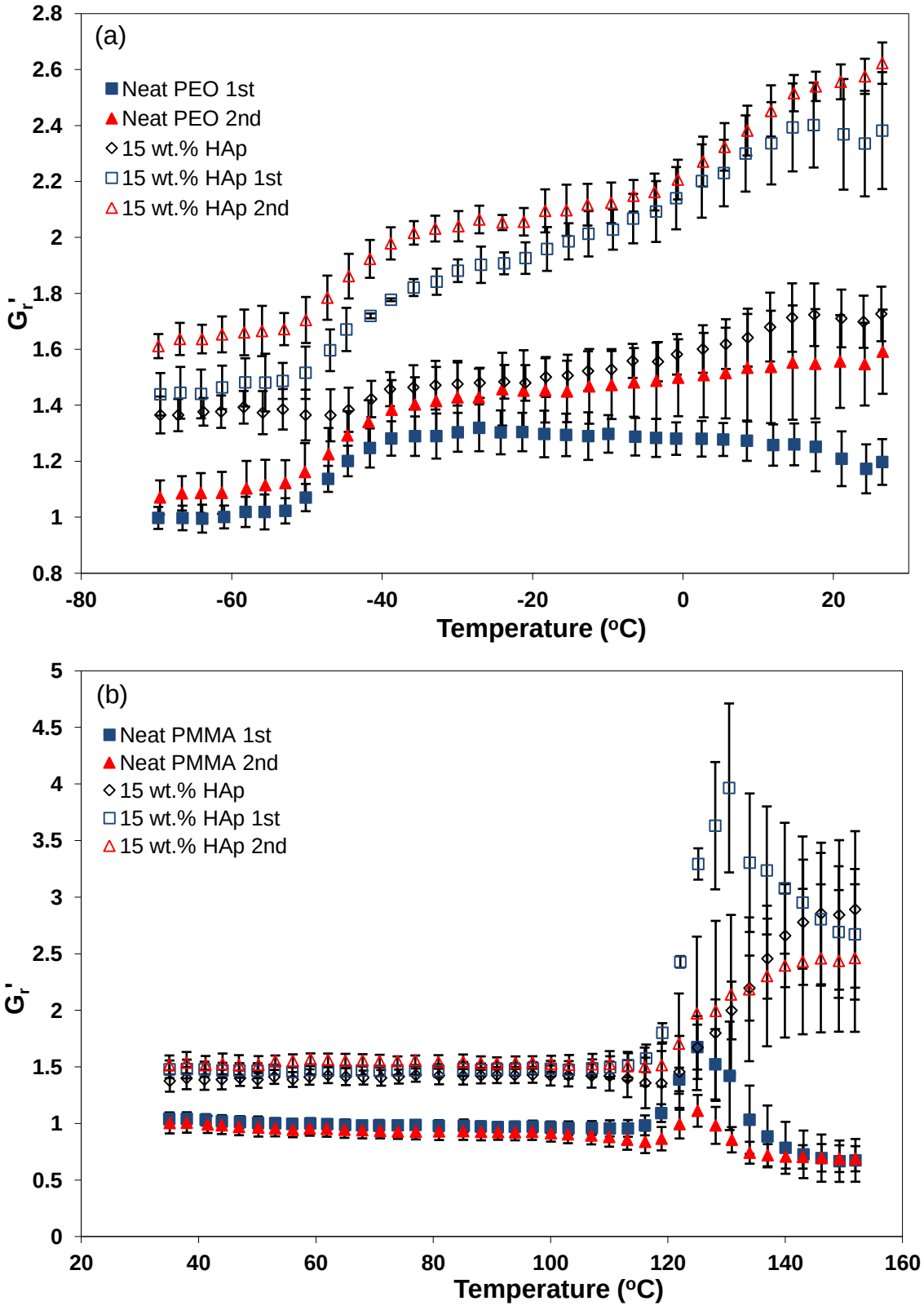

Figure 5.6. Relative modulus (Gr') data for HAp/PEO nanocomposites (a) and HAp/PMMA nanocomposites (b)

Both composite systems showed similar reinforcement trends in the glassy region. However, there were different reinforcement trends between neat PEO and PMMA. This different reinforcement trend could be explained by the structural change of polymer matrix due to the drawing process. In neat PEO, the crystalline structure could be altered by drawing process and influence the mechanical properties. The drawing process influenced the local motions of molecular chains in the rubbery region and DMA data showed drawn samples (- 41 °C) had increased T_g compared to neat PEO (- 47 °C), and this effect was contributed to the enhancement of the mechanical properties [188, 190]. In neat PMMA, on other hand, there was no significant change of modulus, indicating that drawing process could not influence polymer structure. This result agrees with the data obtained from DSC measurements which could not observe melting behavior from the structure change of PMMA matrix as well as no change of T_g from DMA data. In composite systems, the mechanical behavior was much more complicated because a couple of factors were involved for overall reinforcement in G'. For HAp/PEO nanocomposite, the overall reinforcement could be divided in three contributions: the structural changes in the polymer matrix (polymer crystallinity change), the effect of HAp nanoparticle addition, and the arrangement of HAp nanoparticles. The reinforcement for HAp/PMMA nanocomposites could be divided into two contributions which were the effect of HAp nanoparticle addition and the arrangement of HAp nanoparticle in polymer matrix since there was no significant contribution from the structure change of PMMA matrix. Thus, in order to investigate the effect of the particle arrangement in polymer matrix, we need to separate the relative contributions, which is discussed more detail below.

In order to evaluate the effect of the drawing process on the matrix dynamics, the G" data were used to evaluate the T_g. Using the peak maxima of G" to assign T_g, the value for isotropic neat PEO and HAp/PEO nanocomposite had approximately - 47 °C. For the drawn samples, the T_g was increased and the value was approximately - 41 °C ± 1 °C. For the HAp/PMMA nanocomposite system, T_g for all samples was approximately 122 °C. Thus, the drawing process did not impact matrix mobility in the PMMA based materials. Compared with the results for both systems, the addition of HAp nanoparticles into polymer matrices did not change matrix dynamics whereas drawing process made somewhat different effects on the T_g behavior. As mentioned before, the drawing process could alter the local motions of molecular chains on the semicrystalline polymer matrix, and this effect could contribute to change of T_g on neat PEO and HAp/PEO nanocomposite observed through DMA results.

In order to understand how the arrangement of HAp nanoparticles in polymer matrix influences the properties on nanocomposite, the relative contribution of the nanoparticles arrangement for enhanced mechanical properties needed to be separate. We presumed the contribution of the nanoparticles arrangement could be obtained the following relationship.

For contribution of HAp nanoparticle addition with respect to neat polymer matrix,

$\Delta G'$ (HAp nanoparticle addition) = G' (isotropic composite) – G' (isotropic neat polymer matrix) (3)

For contribution of HAp nanoparticle arrangement and addition,

$\Delta G'$ (HAp nanoparticle arrangement and addition) = G' (composite after drawing process) – G' (neat polymer matrix after drawing process) (4)

Figure 5.7 shows the changes of reinforcement for both nanocomposite systems on the storage modulus obtained from above the equations. In the glassy region, both nanocomposite system showed similar reinforcement trends which was relatively constant ΔG' and limited temperature dependency. The HAp/PEO system showed an increased ΔG' after the drawing processes but it is difficult to distinguish the change between the ΔG' for HAp nanoparticle addition and ΔG' for HAp nanoparticle arrangement and addition from the first drawn sample based on propagated experimental error. As stated above, this behavior was attributed to the structural change of PEO matrix. In the first drawing process for PEO composite system, the reinforcement was associated with the effect of crystallinity change as well as particle addition into matrix. Even though both neat PEO and PEO composite of the first drawn samples had similar level of crystallinity, the amounts of crystallinity change from the drawing process were different. This complicated contribution made it difficult to distinguish the reinforcement. On the other hand, both neat PEO and PEO composite of the second drawn samples had similar level of crystallinity and the amounts of crystallinity change from the process. Thus, the modulus change between ΔG' for HAp nanoparticle addition and ΔG' for HAp nanoparticle arrangement and addition from the second drawn sample was attributed to the contribution of particle arrangement. In HAp/PMMA system, since there was no effect of structural changes in the PMMA matrix, the modulus change between ΔG' for HAp nanoparticle addition and ΔG' for HAp nanoparticle arrangement and addition could be the contribution of particle arrangement. They showed an increased ΔG' for HAp nanoparticle arrangement from the first drawing process and further increased for the second drawing process. Compared with the second drawn samples for both systems,

the particle arrangement from the second drawing process enhanced overall reinforcement, indicating that composite microstructures were formed from a mechanical drawing process. However, the modulus changes in both systems were similar and small compared to overall reinforcements. Thus, the difference mechanical property with respect to the degree of orientation was difficult to distinguish between two matrix systems in the glassy region.

In the rubbery region, the ΔG' for drawn HAp/PEO samples began to gradually increase with respect to ΔG' for HAp nanoparticle addition whereas the ΔG' for HAp/PMMA showed no reinforcement effect and temperature dependency. For the HAp/PEO system, the particle arrangement, the effect of restricting the chain mobility or both effects might influence the overall reinforcement above T_g. However, HAp/PMMA nanocomposite system had very low storage modulus because it was an amorphous polymer. Thus, no significant modulus difference could be observed.

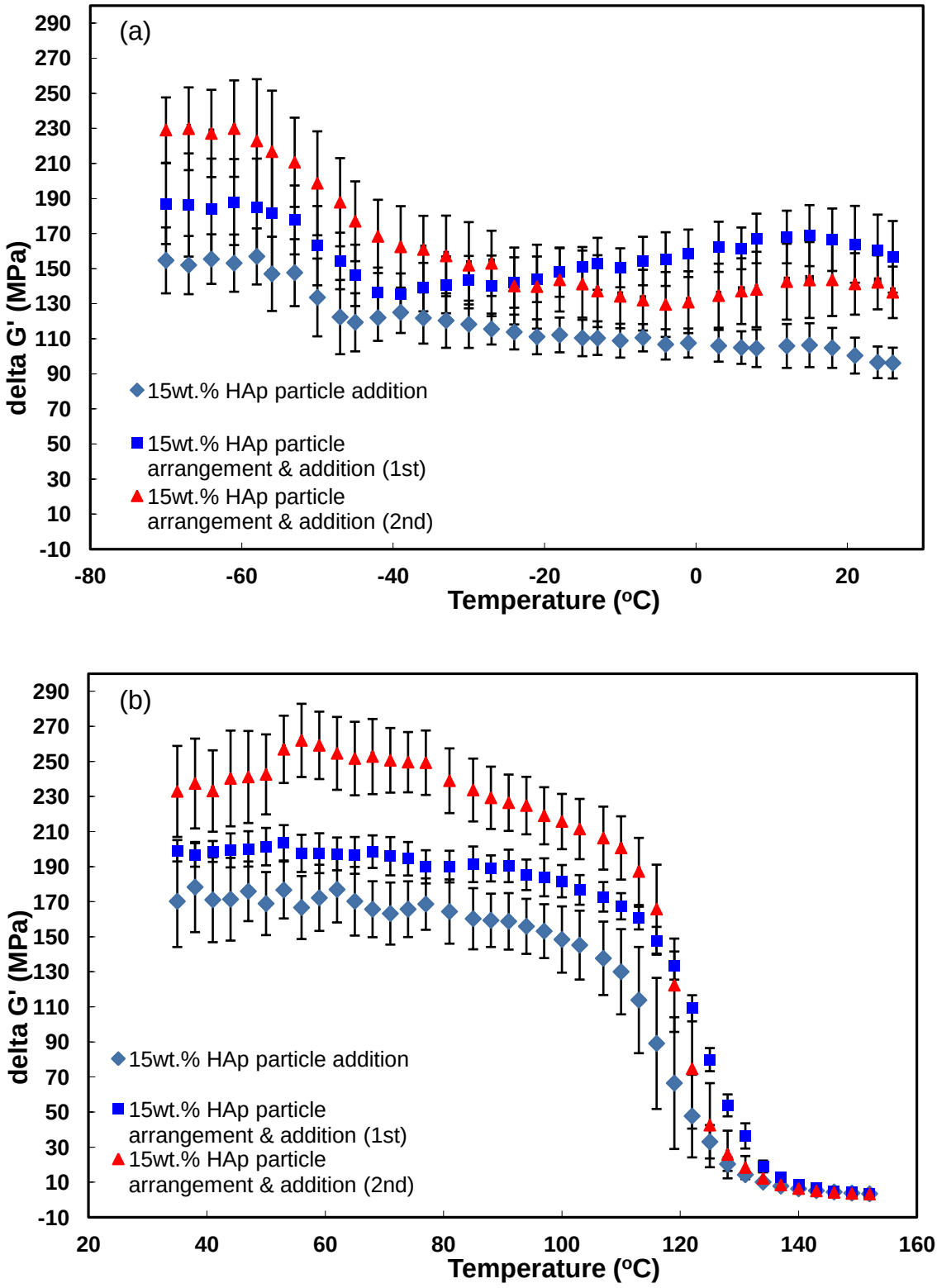

Figure 5.7. The ΔG' from the contribution of HAp addition and arrangement for HAp/PEO nanocomposites (a) and HAp/PMMA nanocomposites (b).

5.4. Conclusions

In this research, the effect of particle arrangement in polymer matrices with different matrix morphologies on the nanocomposite properties was investigated. The polymer nanocomposites were prepared by dispersing block copolymer decorated HAp nanoparticles in both semicrystalline and amorphous polymer matrices where chemistry of exposed polymer block and the matrix were the same. The polymer coating on the HAp nanoparticles prevented particle aggregation at 15 wt.% of HAp loading and enabled microstructure construction with drawing process. SEM images for both HAp/PEO and HAp/PMMA systems showed that HAp nanoparticles in polymer matrix had preferential orientation along the first drawing direction whereas the second drawing process only had small change on particle orientation. The degree of orientation value (*f*) obtained from XRD measurements indicated that particle orientation could be correlated with matrix properties. From these experiments, better particle orientation could be achieved in semicrystalline polymer matrix (PEO) since this drawing process could alter polymer crystalline structure and the induced crystalline structure could make particles better aligned along the drawing direction. The structural changes occurring during the drawing in the PEO matrix system was investigated by thermal analysis. From DSC measurements, it was shown that the polymer crystallinity of HAp/PEO nanocomposites increased after the first drawing process. In order to understand the effect of particle arrangement on the mechanical properties, the relative contributions were separated from the overall reinforcement. For HAp/PEO nanocomposite system, the contribution of reinforcement from structural change of matrix from drawing process was involved and

significantly influenced on the overall reinforcement. On other hand, this contribution could not be observed in HAp/PMMA nanocomposite system. The experimental results indicated that particle arrangement for both matrix systems from the second drawing process influenced overall reinforcement, indicating that composite microstructures were formed from a mechanical drawing process. Overall, the drawing process influenced particle arrangements, and better particle orientation could be achieved in semicrystalline polymer matrix due to induced crystalline structure. Thus, particle arrangement was related to the matrix morphology. These results will be used to refine the drawing process parameters to achieve composite microstructures with triangulated arrangement of nanoparticles.

CHAPTER 6

CONCLUSIONS AND FUTURE WORK

6.1. Conclusions

This research showed a strategy for constructing tensegrity-inspired microstructures. Since the polymer coating on the HAp surface would be used to establish the interphase material, HAp nanoparticle synthesis using block copolymer templates was an effective method to preparing the building blocks for tensegrity-inspired microstructure. The particle arrangement could be manipulated by a mechanical drawing process, and the experimental results showed the resulting particle arrangement was significantly influenced by matrix morphology. These results will be used to design microstructured composites.

A summary of the conclusions for the studies presented in the following section.

6.1.1. Synthesis of HAp nanoparticles of controlled shapes using block copolymer templates (Chapter 3)

- HAp nanoparticles were synthesized using PEO-*b*-PMMA and PMMA-*b*-PMMA block copolymer templates.
- Two different shapes of HAp nanoparticles were synthesized and the morphology of particles can be controlled by the mole ratio of the calcium precursor and PMMA block of block copolymer (mole ratio of Ca^{2+}/COO^{-}).

SEM images showed that the morphology of HAp nanoparticles changed from sphere to needle as mole ratio of Ca^{2+}/COO^- increased.

- Chemical structure analysis from FT-IR indicated that the reaction was occurred between COO^- groups in PMMA block and Ca^{2+} ions and the block copolymer was anchored on the HAp nanoparticle surface. The block copolymer remained on the particle surface was also confirmed by TGA analysis.
- The mechanism for the particle shape change was investigate using XRD, and the experimental results showed the crystallite sizes along (002) and (310) direction were reduced as the mole ratio of Ca^{2+}/COO^- decreased. Comparing the D_{002}/D_{310} ratio of the sphere and needle particle, the greater ratio value suggested a preferential adsorption of block copolymer on the HAp nanoparticle surfaces parallel to the c-axis.
- Comparing PEO-*b*-PMMA and PMMA-*b*-PMMA systems, general morphological change behavior was independent of reaction media used in the synthesis. However, the crystal growth behavior showed differences between two block copolymer systems. This behavior might be attributed to the difference of ionization of block copolymers or precursors in different reaction media.

6.1.2. Investigation of the effect of particle loadings and shapes on isotropic nanocomposite properties (Chapter 4)

- Two different shapes of HAp nanoparticles decorated with PEO were dispersed in a PEO matrix to form nanocomposites and these materials were characterized

for particle dispersion. The dispersion trends above 5 wt.% of HAp loadings indicated that the polymer coating on the particle was effective at preventing nanoparticle clustering in a matrix with a relatively high level of crystallinity.

- The nanocomposites with 1 wt.% HAp showed more aggregation than the higher loading. The rheology results indicated the relative relaxation time of 1 wt.% HAp nanocomposite was similar to the neat PEO whereas the higher particle loadings showed relatively longer relaxation time. Thus, the longer times would lead to a persistence of the kinetically trapped condition in the nanocomposites with the higher particle loadings.
- Both nanoparticle composite systems showed the decreased matrix crystallinity at a critical particle loading, but the decrease in crystallinity occurred at different particle loadings: 15 wt.% for the needle particles and 20 wt.% for the spherical particles. Considering the nanoparticle surface area and the interparticle spacing, those values are approximately equal at these nanoparticle loadings. Thus, both factors could have influenced the matrix crystallinity.
- The experimental results indicated that the thermomechaincal properties were similar between two particle systems due to their low aspect ratios. At temperatures above T_g, however, relative storage modulus (G_r') showed greater temperature dependence, and the dependence increased as nanoparticle loading increased. The temperature dependence was more prominent in the needle particle nanocomposite system.

6.1.3. Construction of HAp building blocks into the tensegrity-inspired microstructure (Chapter 5)

- Block copolymer decorated needle-shaped HAp nanoparticles were dispersed into two different matrix polymers, and the particle arrangement was manipulated using a mechanical drawing process. The experimental results indicated that both matrix nanocomposite systems showed preferential particle orientation along the first drawing direction, and higher particle orientation could be achieved in semicrystalline matrix system (PEO). This behavior was attributed to the induced crystalline structure through the drawing process.
- The matrix crystallinity and the storage modulus of PEO nanocomposites were increased after the first drawing process. The expected results indicated that the drawing process could influence the structural change of PEO matrix system.
- In order to understand the effect of particle arrangement on the thermomechanical properties in different matrix systems, the relative reinforcement contribution was separated from the overall reinforcement. At temperature below T_g, both systems showed similar reinforcement levels, and the relatively constant temperature dependence. At temperature above T_g, however, PEO nanocomposite system showed increased reinforcement efficacies whereas PMMA nanocomposite system showed no reinforcement changes.
- The changes of thermomechanical properties with respect to the degree of particle orientation were difficult to distinguish because of experimental error.

6.2. Recommendations for Future Work

In this research, two different shapes of HAp nanoparticles were synthesized and their mechanical properties compared in nanocomposites. In Chapter 4, nanocomposites prepared with spherical and needle particles showed similar reinforcement trends. In addition, the contribution of particle arrangement in semicrystalline and amorphous polymer matrices in Chapter 5 showed similar reinforcement, even though they had different particle orientations. We presumed this behavior was attributed to the use of low aspect ratio particles. Thus, higher aspect ratio nanoparticles should be synthesized and their nanocomposite properties investigated since higher aspect ratio particles should allow effective load transfer between the matrix and particle. In order to control aspect ratio of HAp nanoparticles, various synthesis conditions should be examined, such as pH, molecular weight of block copolymer, and temperature. Since the pH of the block copolymer solution could influence the ionization of PMAA block and the crystallite growth was more restricted when greater amount of COO^- reacted with calcium ions, higher aspect ratio HAp nanoparticles might be synthesized with lower ionization of carboxyl acid group in PMAA block at lower pH. At lower pH, only partially ionized COO- could interact with calcium precursors and the effect of crystallite growth restriction might be reduced. Additionally, experimental results in this research showed particle dimensions for both block copolymer systems were slightly different because particles were synthesized using block copolymers with different molecular weights of PMAA block polymer. Thus, the effect of molecular weight of PMAA block copolymer on the particle synthesis should be also examined. If the particle aspect ratio could be

controlled from these synthesis parameters, and nanocomposites could be prepared using higher aspect ratio HAp nanoparticles, enhanced mechanical properties could be achieved at a relatively lower nanoparticle concentration.

The mechanical drawing process was employed in order to manipulate the particle orientation. However, this technique could not precisely control the particle arrangement. In the future, alternative techniques for controlling the particle arrangement should be investigated such as block copolymer assembly, LBL, and so on. This result will provide increased understanding material design principles for the nanocomposites.

APPENDIX A

Comparison DMA Tests for Sheet Form and Stacked Film Configuration

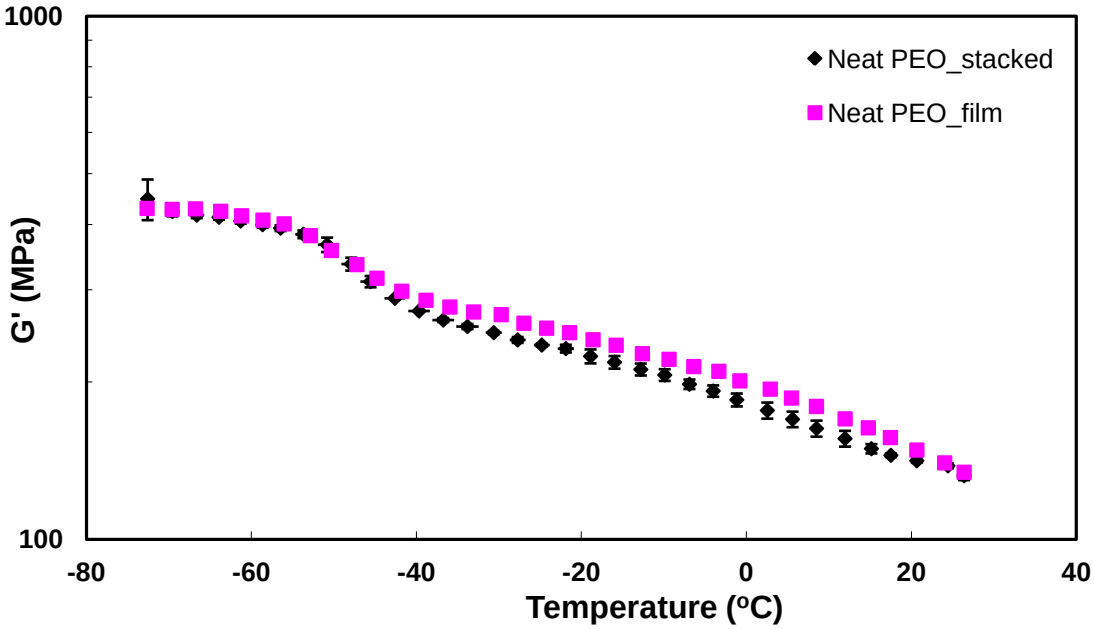

Figure A.1. DMA testing for the neat PEO in bulk form and stacked film configuration

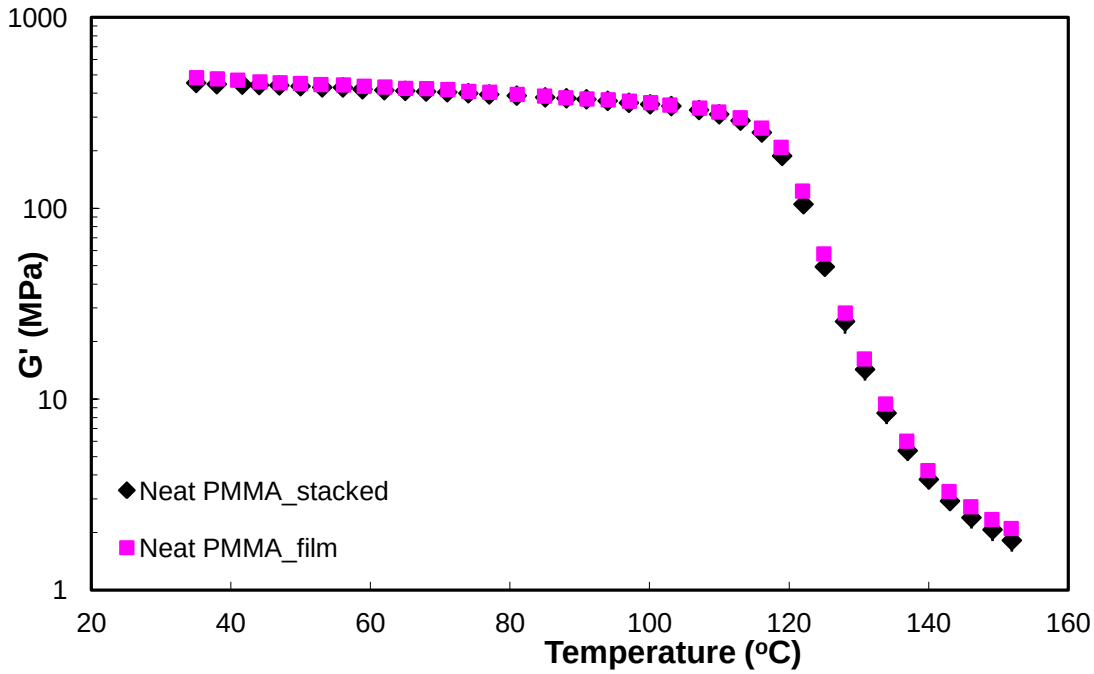

Figure A.2. DMA testing for the neat PMMA in bulk form and stacked film configuration

APPENDIX B

The Effect of Sonication Time on the HAp Chemical Structure

In order to investigate the effect of sonication on the particle surface, the chemical structure was characterized using FT-IR with respect to sonication times. The result indicated no significant change of chemical structure was observed. Thus, the sonication time up to15 min only dispersed the particles without changing them.

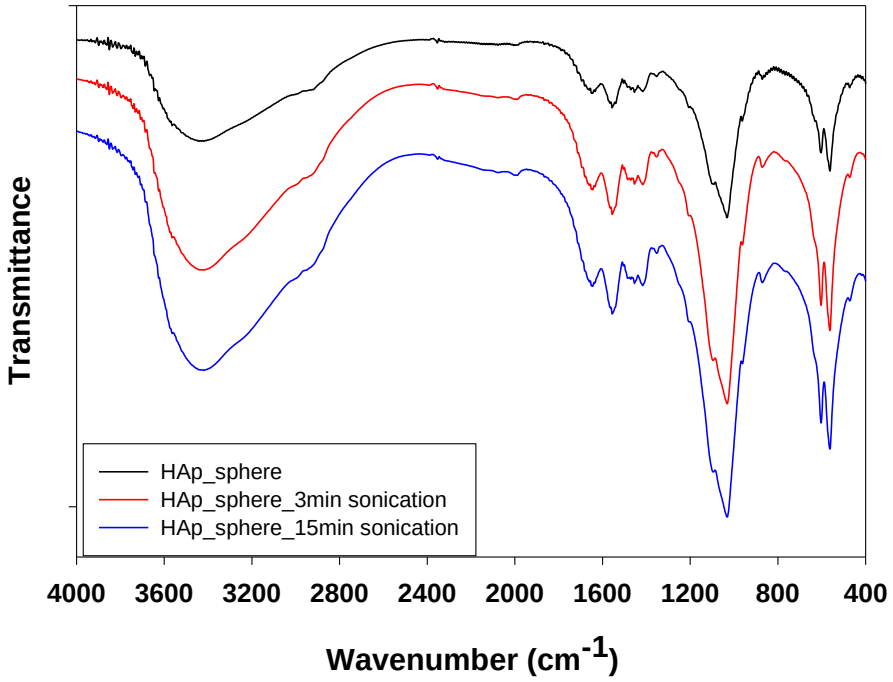

Figure B.1. FT-IR spectra of sonicated HAp nanoparticles

APPENDIX C

Characterization of Isotropic HAp/PMMA Nanocomposites.

In order to compare matrix morphology effects with isotropic semicrystalline polymer matrix composites, isotropic HAp/PMMA nanocomposites were prepared and characterized their morphological and thermomechanical properties.

Following synthesis of HAp nanoparticle using PMMA-*b*-PMAA block copolymer, HAp/PMMA nanocomposites were prepared using needle-shaped HAp nanoparticle according to the process procedure described in Chapter 5, and the resulting nanocomposites were observed using SEM. Figure C.1 shows SEM images of HAp nanocomposite samples with particle loadings of 1, 5, and 15 wt.%. The images show no significant particle aggregations. In this study, the PMMA block polymer decorating the HAp particles was compatible with PMMA matrix polymer, and it could be facilitated particle dispersion into the PMMA matrix. Thus, this result was attributed that the PMMA block on the HAp compatibilized the nanocomposite components.

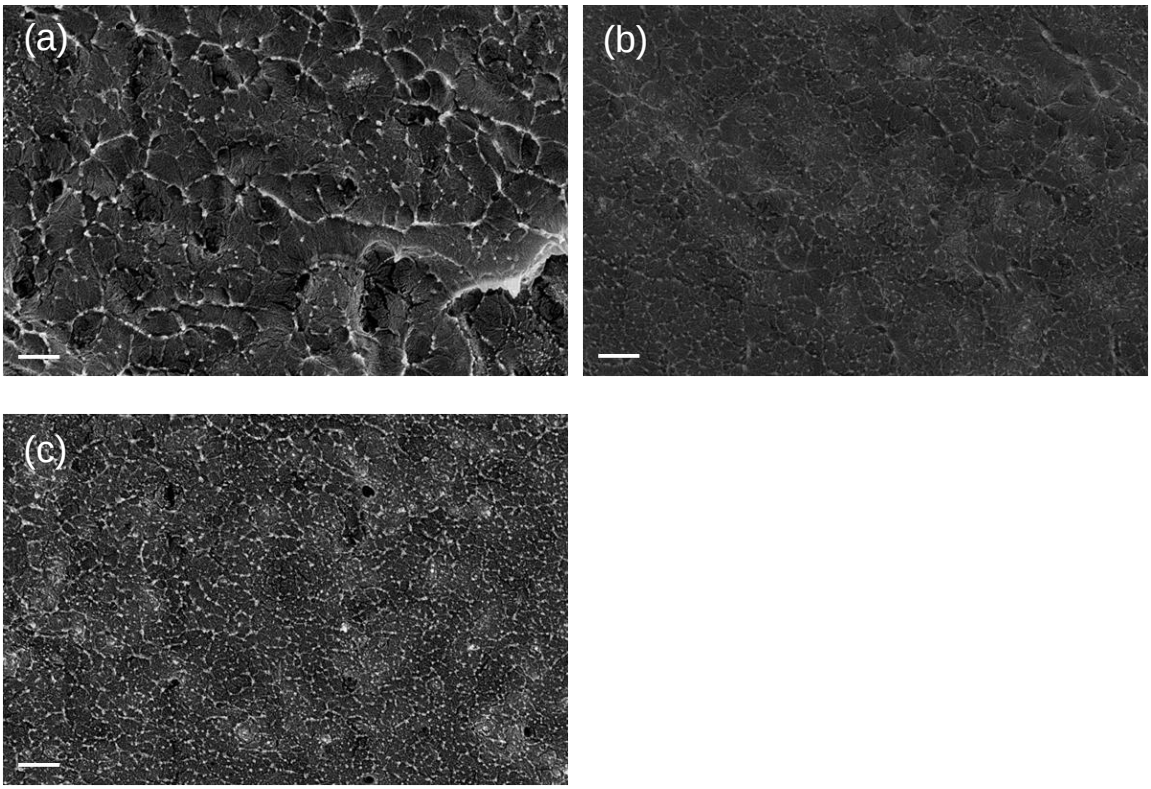

Figure C.1. SEM micrographs of HAp particle dispersion and distribution in the PMMA matrix. 1 wt. needle (a), 5 wt. needle (b), 15 wt. needle (c). (Scale bar: 500nm)

In order to determine the effect of the HAp nanoparticle on the mechanical properties, DMA measurements were performed using a Mettler Toledo DMA861[e] dynamic mechanical analyzer (DMA). The storage modulus (G') and loss modulus (G") data are shown in Figure C.2. In the glassy region, the G' increased as the HAp nanoparticle loading increased. The level of reinforcement of 15 wt. % particle loading at 50 ˚C was 39 %. This enhanced reinforcement was attributed to relatively well dispersed and distributed nanoparticles in the PMMA matrix. In the rubbery region, there was no significant enhancement upto 5 wt. % loading of HAp, but 15 wt. % of HAp nanocomposite showed enhanced G'. The G" data were used to evaluate the T_g. T_g was obtained from the peak maxima of G", and all values had approximately 120 ˚C and the errors were within 1 ˚C. T_gs were also measured using a TA Q200 differential scanning

calorimeter (DSC). The values were approximately 117 ˚C and the errors were within 1 ˚C. Compared with T_g obtained from DSC and DMA, the addition of HAp nanoparticles did not significantly influence matrix dynamics. Overall, the addition of HAp nanoparticles influenced the mechanical properties on nanocomposites, and the tethered polymer block on HAp surface could facilitate the particle dispersion and distribution which affected the overall reinforcement.

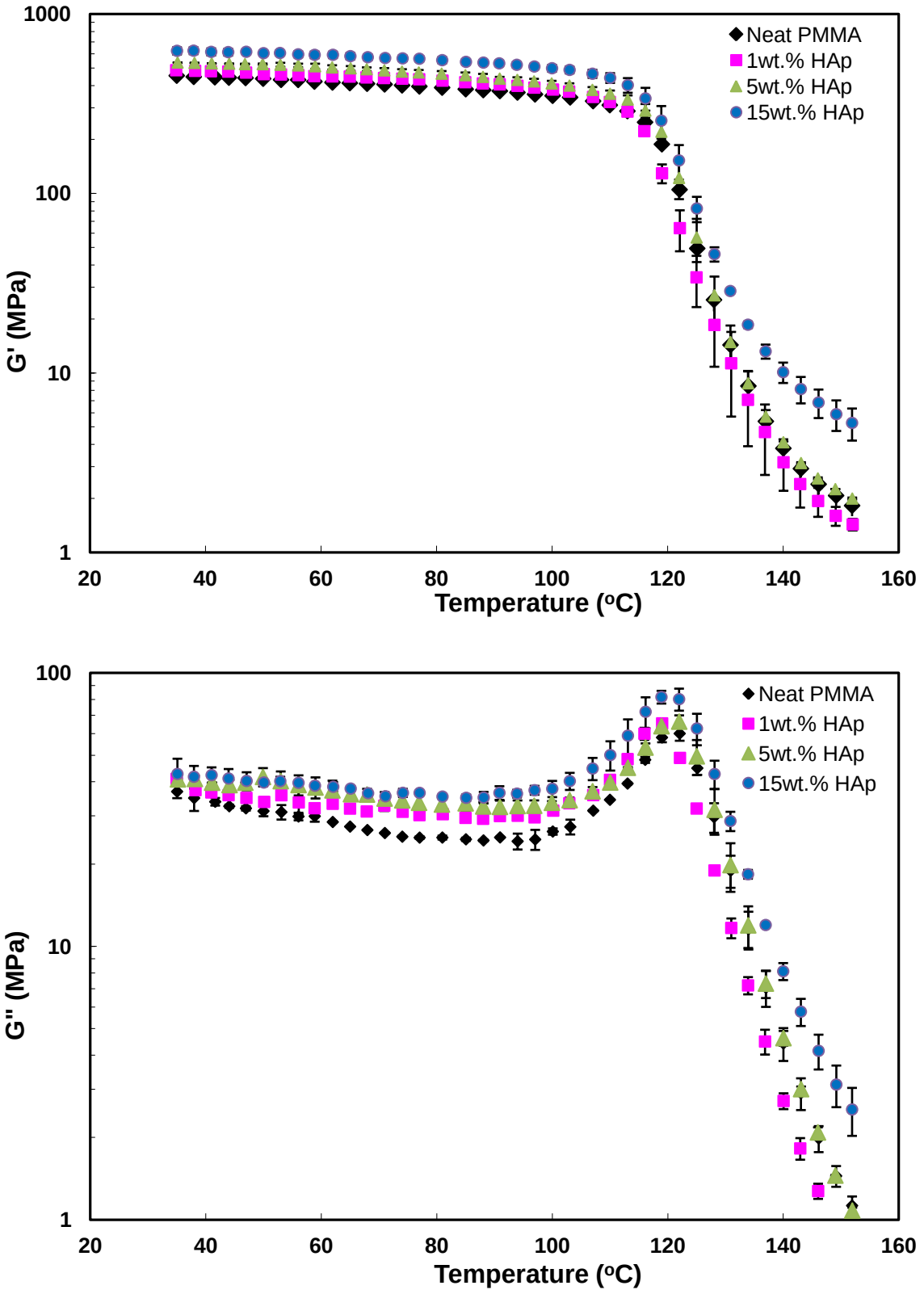

Figure C.2. Storage modulus and loss modulus for neat PMMA and HAp nanocomposites.

REFERENCES

1. Fukushima, Y. and S. Inagaki, *Synthesis of an intercalated compound of montmorillonite and 6-polyamide.* Journal of Inclusion Phenomena, 1987. **5**(4): p. 473-482.
2. Fukushima, Y., et al., *Swelling behavior of montmorillonite by poly-6-amide.* Clay Minerals, 1988. **23**(1): p. 27-34.
3. Kojima, Y., et al., *Mechanical properties of nylon-6 clay hybrid.* Journal of Materials Research, 1993. **8**(5): p. 1185-1189.
4. Usuki, A., et al., *Synthesis of nylon 6-clay hybrid.* Journal of Materials Research, 1993. **8**(5): p. 1179-1184.
5. Vaia, R.A. and J.F. Maguire, *Polymer nanocomposites with prescribed morphology: Going beyond nanoparticle-filled polymers.* Chemistry of Materials, 2007. **19**(11): p. 2736-2751.
6. Kalfus, J. and J. Jancar, *Relaxation processes in PVAc-HA nanocomposites.* Journal of Polymer Science Part B: Polymer Physics, 2007. **45**(11): p. 1380-1388.
7. Favier, V., et al., *Nanocomposite materials from latex and cellulose whiskers.* Polymers for Advanced Technologies, 1995. **6**(5): p. 351-355.
8. Avella, M., et al., *Poly(ε-caprolactone)-based nanocomposites: Influence of compatibilization on properties of poly(ε-caprolactone)–silica nanocomposites.* Composites Science and Technology, 2006. **66**(7-8): p. 886-894.
9. K. I. Winey, R.A.V., *Polymer Nanocomposites.* MRS Bulletin, 2007. **32**: p. 314-322.
10. Jordan, J., et al., *Experimental trends in polymer nanocomposites—a review.* Materials Science and Engineering: A, 2005. **393**(1-2): p. 1-11.
11. Herrera, N.N., et al., *Silylation of laponite clay particles with monofunctional and trifunctional vinyl alkoxysilanes.* Journal of Materials Chemistry, 2005. **15**(8): p. 863.

12. Herrera, N., et al., *Aqueous dispersions of silane-functionalized laponite clay platelets. A first step toward the elaboration of water-based polymer/clay nanocomposites.* Langmuir, 2004. **20**: p. 1564-1571.
13. Carrado, K., et al., *Use of organo-and alkoxysilanes in the synthesis of grafted and pristine clays.* Chemistry of Materials, 2001. **13**: p. 3766-3773.
14. Wheeler, P., et al., *Synthesis and characterization of covalently functionalized laponite clay.* Chemistry of materials, 2005. **17**: p. 3012-3018.
15. Hong, Z., et al., *Nano-composite of poly(L-lactide) and surface grafted hydroxyapatite: mechanical properties and biocompatibility.* Biomaterials, 2005. **26**(32): p. 6296-304.
16. Moll, J.F., et al., *Mechanical Reinforcement in Polymer Melts Filled with Polymer Grafted Nanoparticles.* Macromolecules, 2011: p. 110824072716001.
17. Akcora, P., et al., *Segmental Dynamics in PMMA-Grafted Nanoparticle Composites.* Macromolecules, 2010. **43**(19): p. 8275-8281.
18. Akcora, P., et al., *"Gel-like" Mechanical Reinforcement in Polymer Nanocomposite Melts.* Macromolecules, 2010. **43**(2): p. 1003-1010.
19. Akcora, P., et al., *Anisotropic self-assembly of spherical polymer-grafted nanoparticles.* Nature materials, 2009. **8**(4): p. 354-359.
20. Khan, J., et al., *Polymer Crystallization in Nanocomposites: Spatial Reorganization of Nanoparticles.* Macromolecules, 2009. **42**(15): p. 5741-5744.
21. Yezek, L., et al., *Influence of hair density and hair length on interparticle interactions of spherical polymer brushes in a homopolymer matrix.* Macromolecules, 2003. **36**(11): p. 4226-4235.
22. Gohr, K. and W. Schartl, *Dynamics of copolymer micelles in a homopolymer melt: Influence of the matrix molecular weight.* Macromolecules, 2000. **33**(6): p. 2129-2135.
23. Chevigny, C., et al., *"Wet-to-Dry" Conformational Transition of Polymer Layers Grafted to Nanoparticles in Nanocomposite.* Macromolecules, 2010. **43**(11): p. 4833-4837.

24. La, Y.-H., et al., *Directed assembly of cylinder-forming block copolymer films and thermochemically induced cylinder to sphere transition: a hierarchical route to linear arrays of nanodots.* Nano letters, 2005. **5**(7): p. 1379-1384.
25. Bockstaller, M.R., et al., *Size-selective organization of enthalpic compatibilized nanocrystals in ternary block copolymer/particle mixtures.* Journal of the American Chemical Society, 2003. **125**(18): p. 5276-5277.
26. Gusev, A. and M. Rozman, *Numerical search for morphologies providing ultra high elastic stiffness in filled rubbers.* Computational and Theoretical Polymer Science, 1999. **9**: p. 335-337.
27. Lee, J.Y., et al., *Effect of nanoscopic particles on the mesophase structure of diblock copolymers.* Macromolecules, 2002. **35**(13): p. 4855–4858.
28. Gaharwar, A.K., et al., *Highly Extensible Bio-Nanocomposite Films with Direction-Dependent Properties.* Advanced Functional Materials, 2010. **20**(3): p. 429-436.
29. Dundigalla, A., et al., *Unusual Multilayered Structures in Poly(ethylene oxide)/Laponite Nanocomposite Films.* Macromolecular Rapid Communications, 2005. **26**(3): p. 143-149.
30. Stefanescu, E., et al., *Structure and thermal properties of multilayered Laponite/PEO nanocomposite films.* Polymer, 2006. **47**(21): p. 7339-7348.
31. Loizou, E., et al., *Large scale structures in nanocomposite hydrogels.* macromolecules, 2005. **38**(6): p. 2047-2049.
32. Jeon, S.-J., et al., *Hierarchically Structured Colloids of Diblock Copolymers and Au Nanoparticles.* Chemistry of Materials, 2009. **21**(16): p. 3739-3741.
33. Kim, B.J., et al., *Effect of Areal Chain Density on the Location of Polymer-Modified Gold Nanoparticles in a Block Copolymer Template.* macromolecules, 2006. **39**(12): p. 4108-4114.
34. Kim, B.J., et al., *Tailoring Core−Shell Polymer-Coated Nanoparticles as Block Copolymer Surfactants.* Macromolecules, 2009. **42**(16): p. 6193-6201.
35. Haggenmueller, R., et al., *Aligned single-wall carbon nanotubes in composites by melt processing methods.* Chemical Physics Letters, 2000. **330**(3): p. 219–225.

36. Bigi, a., S. Panzavolta, and N. Roveri, *Hydroxyapatite-gelatin films: a structural and mechanical characterization.* Biomaterials, 1998. **19**: p. 739-744.
37. Park, S.-Y., Y.-H. Cho, and R.a. Vaia, *Three-Dimensional Structure of the Zone-Drawn Film of the Nylon-6/Layered Silicate Nanocomposites.* Macromolecules, 2005. **38**(5): p. 1729-1735.
38. Kaneko, T., et al., *Mechanically Drawn Hydrogels Uniaxially Orient Hydroxyapatite Crystals and Cell Extension.* Chemistry of Materials, 2004. **16**(26): p. 5596-5601.
39. Koerner, H., et al., *Generating Triaxial Reinforced Epoxy / Montmorillonite Nanocomposites with Uniaxial Magnetic Fields.* Chemistry of Materials, 2005. **17**(8): p. 1990-1996.
40. Koganemaru, a., et al., *Composites of Polyacrylonitrile and Multiwalled Carbon Nanotubes Prepared by Gelation/Crystallization from Solution.* Advanced Functional Materials, 2004. **14**(9): p. 842-850.
41. Steinert, B. and D. Dean, *Magnetic field alignment and electrical properties of solution cast PET–carbon nanotube composite films.* Polymer, 2009. **50**(3): p. 898-904.
42. Ye, H., et al., *Reinforcement and rupture behavior of carbon nanotubes–polymer nanofibers.* Applied Physics Letters, 2004. **85**(10): p. 1775.
43. Fuller, B. Protfolio Artnews Ann., 1961, 4, 112-127
44. Djouadi, B.S., R.M.J.C. Pons, and B. Crosnier, *Active control of tensegrity systems.* Journal of aerospace engineering, 1998. **11**(2): p. 37-44.
45. Ingber, D.E., *From Cellular Mechanotransduction to Biologically Inspired Engineering.* Annals of Biomedical Engineering, 2010. **38**(3): p. 1148-1161.
46. Stamenović, D. and D.E. Ingber, *Tensegrity-guided self assembly: from molecules to living cells.* Soft Matter, 2009. **5**(6): p. 1137.
47. Luo, Y., et al., *A multi-modular tensegrity model of an actin stress fiber.* Journal of Biomechanics, 2008. **41**(11): p. 2379-2387.
48. Wang, N. and D.E. Ingber, *Control of cytoskeletal mechanics by extracellular matrix, cell shape, and mechanical tension.* Biophysical journal, 1994. **66**(6): p. 2181-2189.

49. Sultan, C., D. Stamenović, and D.E. Ingber, *A computational tensegrity model predicts dynamic rheological behaviors in living cells.* Annals of biomedical engineering, 2004. **32**(4): p. 520-530.
50. Liedl, T., et al., *Self-assembly of three-dimensional prestressed tensegrity structures from DNA.* Nature nanotechnology, 2010. **5**(7): p. 520-524.
51. Sultan, C., *Force and torque smart tensegrity sensor.* Proceedings of SPIE, 1998. **3323**: p. 357-368.
52. Sultan, C., *Peak-to-peak control of an adaptive tensegrity space telescope.* Proceedings of SPIE, 1999. **3667**: p. 190-201.
53. Joris, S. and C. Amberg, *Nature of deficiency in nonstoichiometric hydroxyapatites. II. Spectroscopic studies of calcium and strontium hydroxyapatites.* The Journal of Physical Chemistry 1971. **75**(20): p. 3172-3178.
54. Christoffersen, J., et al., *Regeneration by surface-coating of bone char used for defluoridation of water.* Water research, 1991. **25**(2): p. 227-229.
55. Walsh, W. and N. Guzelsu, *Compressive properties of cortical bone: mineral-organic interfacial bonding.* Biomaterials, 1994. **15**(2): p. 137-145.
56. Murugan, R. and S. Ramakrishna, *Development of nanocomposites for bone grafting.* Composites Science and Technology, 2005. **65**(15-16): p. 2385-2406.
57. http://www.matweb.com/search/SpecificMaterial.asp?bassnum=BBIOC00.
58. Kaur, J., Properties of biologically relevant nanocomposites: effects of calcium phosphate nanoparticle attributes and biodegradable polymer morphology, Ph.D. Dissertation, 2010
59. Dalas, E. and P.G. Koutsoukos, C*rystallization of hydroxyapatite from aqueous solutions in the presence of cadmium.* Journal of the Chemical Society, Faraday Transactions 1, 1989. 8**5(**10): p. 3159.
60. Koutsopoulos, S., et al., I*nhibition of hydroxyapatite formation by zirconocenes.* Langmuir, 1995. 1**1:** p. 1831-1834.
61. Webster, T., et al., E*nhanced functions of osteoblasts on nanophase ceramics.* Biomaterials, 2000. 2**1(**17): p. 1803-1810.
62. Ota, Y., et al., N*ovel preparation method of hydroxyapatite fibers.* Journal of the American Ceramic Society, 1998. 8**1(**6): p. 1665-1668.

63. Murugan, R. and S. Ramakrishna, B*ioresorbable composite bone paste using polysaccharide based nano hydroxyapatite.* Biomaterials, 2004. 2**5(**17): p. 3829-3835.
64. Murugan, R. and S. Ramakrishna, A*queous mediated synthesis of bioresorbable nanocrystalline hydroxyapatite.* Journal of Crystal Growth, 2005. 2**74(**1-2): p. 209-213.
65. Liu, Q., J. de Wijn, and C. van Blitterswijk, N*ano-apatite/polymer composites: mechanical and physicochemical characteristics.* Biomaterials, 1997. 1**8(**19): p. 1263-1270.
66. Zhang, S. and K. Gonsalves, P*reparation and characterization of thermally stable nanohydroxyapatite.* Journal of materials science. Materials in medicine, 1997. 8**(**1): p. 25-28.
67. Lin, K., et al., H*ydrothermal microemulsion synthesis of stoichiometric single crystal hydroxyapatite nanorods with mono-dispersion and narrow-size distribution.* Materials Letters, 2007. 6**1(**8-9): p. 1683-1687.
68. Zhou, W.Y., et al., S*ynthesis of carbonated hydroxyapatite nanospheres through nanoemulsion.* Journal of Materials Science: Materials in Medicine, 2007. 1**9(**1): p. 103-110.
69. Antonietti, M., et al., I*norganic/Organic Mesostructures with Complex Architectures: Precipitation of Calcium Phosphate in the Presence of Double-Hydrophilic Block Copolymers.* Chemistry - A European Journal, 1998. 4**(**12): p. 2493-2500.
70. Tjandra, W., et al., N*anotemplating of Calcium Phosphate Using a Double-Hydrophilic Block Copolymer.* Chemistry of Materials, 2005. 1**7(**19): p. 4865-4872.
71. Marentette, J., et al., C*rystallization of CaCO3 in the presence of PEO-block-PMAA copolymers.* Advanced Materials, 1997. 9**(**8): p. 647-651.
72. Öner, M., et al., C*ontrol of ZnO Crystallization by a PEO- b -PMAA Diblock Copolymer*. Chemistry of Materials, 1998. 1**0(**2): p. 460-463.

73. Lee, J.H., et al., S*ynthesis of polymer-decorated hydroxyapatite nanoparticles with a dispersed copolymer template.* Journal of Materials Chemistry, 2012. 2**2(**23): p. 11556.
74. Guragain, S., B.P. Bastakoti, and K. Nakashima, S*chizophrenic micellization of poly(ethylene oxide-b-methacrylic acid) induced by phosphate and calcium ions.* Journal of Colloid and Interface Science, 2010. 3**50(**1): p. 63-68.
75. Mandel M, L.J., Stadhoud MG, T*he Conformational Transition of Poly(methacrylic acid) in Solution.* Journal of Physical Chemistry, 1967. 7**1(**3): p. 603-612.
76. Kakizawa, Y., et al., O*rganic–inorganic hybrid-nanocarrier of siRNA constructing through the self-assembly of calcium phosphate and PEG-based block aniomer.* Journal of Controlled Release, 2006. 1**11(**3): p. 368-370.
77. Kakizawa, Y. and K. Kataoka, B*lock Copolymer Self-Assembly into Monodispersive Nanoparticles with Hybrid Core of Antisense DNA and Calcium Phosphate.* Langmuir, 2002. 1**8(**12): p. 4539-4543.
78. Kakizawa, Y., et al., S*ize-Controlled Formation of a Calcium Phosphate-Based Organic-Inorganic Hybrid Vector for Gene Delivery Using Poly(ethylene glycol)-block-poly(aspartic acid).* Advanced Materials, 2004. 1**6(**8): p. 699-702.
79. Tjandra, W., et al., S*ynthesis of hollow spherical calcium phosphate nanoparticles using polymeric nanotemplates.* Nanotechnology, 2006. 1**7(**24**)**: p. 5988-5994.
80. Oshika, T. and T. Nagata, A*dhesion of lens capsule to intraocular lenses of polymethylmethacrylate, silicone, and acrylic foldable materials: an experimental study.* British journal of ophthalmology, 1998. 8**2:** p. 549-553.
81. Zhou, S., X. Deng, and H. Yang, B*iodegradable poly(ε-caprolactone)-poly(ethylene glycol) block copolymers: characterization and their use as drug carriers for a controlled delivery system.* Biomaterials, 2003. 2**4(**20): p. 3563-3570.
82. He, C., et al., S*tudy of the synthesis, crystallization, and morphology of poly(ethylene glycol)-poly(epsilon-caprolactone) diblock copolymers.* Biomacromolecules, 2004. 5**(**5): p. 2042-2047.

83. Smith, D.C., L*UTES, GLUES, CEMENTS AND ADHESIVES IN MEDICINE AND DENTISTRY*. Biomedical Engineering, 1973. 8**(**3): p. 108-&.
84. Charnley, J., A*NCHORAGE OF THE FEMORAL HEAD PROSTHESIS TO THE SHAFT OF THE FEMUR.* Journal of Bone and Joint Surgery-British Volume, 1960. 4**2(**1): p. 28-30.
85. Moursi, A.M., et al., E*nhanced osteoblast response to a polymethylmethacrylate-hydroxyapatite composite.* Biomaterials, 2002. 2**3(**1): p. 133-144.
86. Kim, S.B., et al., T*he characteristics of a hydroxyapatite-chitosan-PMMA bone cement.* Biomaterials, 2004. 2**5(**26): p. 5715-23.
87. Deng, X.M., J.Y. Hao, and C.S. Wang, P*reparation and mechanical properties of nanocomposites of poly(D,L-lactide) with Ca-deficient hydroxyapatite nanocrystals.* Biomaterials, 2001. 2**2(**21): p. 2867-2873.
88. Lee, J.H., et al., T*hermal and mechanical characteristics of poly(l-lactic acid) nanocomposite scaffold.* Biomaterials, 2003. 2**4(**16): p. 2773-2778.
89. Kim, S.S., et al., P*oly(lactide-co-glycolide)/hydroxyapatite composite scaffolds for bone tissue engineering.* Biomaterials, 2006. 2**7(**8): p. 1399-409.
90. Hu, Q., P*reparation and characterization of biodegradable chitosan/hydroxyapatite nanocomposite rods via in situ hybridization: a potential material as internal fixation of bone fracture.* Biomaterials, 2004. 2**5(**5): p. 779-785.
91. Kikuchi, M., et al., S*elf-organization mechanism in a bone-like hydroxyapatite/collagen nanocomposite synthesized in vitro and its biological reaction in vivo.* Biomaterials, 2001. 2**2(**13): p. 1705-1711.
92. Chang, M.C. and J. Tanaka, F*T-IR study for hydroxyapatite/collagen nanocomposite cross-linked by glutaraldehyde.* Biomaterials, 2002. 2**3(**24): p. 4811-4818.
93. Chang, M.C., C.-C. Ko, and W.H. Douglas, P*reparation of hydroxyapatite-gelatin nanocomposite.* Biomaterials, 2003. 2**4(**17): p. 2853-2862.
94. Chang, M.C., C.-C. Ko, and W.H. Douglas, C*onformational change of hydroxyapatite/gelatin nanocomposite by glutaraldehyde.* Biomaterials, 2003. 2**4(**18): p. 3087-3094.

95. Kaur, J., J.H. Lee, and M.L. Shofner, I*nfluence of polymer matrix crystallinity on nanocomposite morphology and properties.* Polymer, 2011. 5**2(**19): p. 4337-4344.
96. Lee, H., et al., T*he effect of surface-modified nano-hydroxyapatite on biocompatibility of poly(ε-caprolactone)/hydroxyapatite nanocomposites.* European Polymer Journal, 2007. 4**3(**5): p. 1602-1608.
97. Katti, K.S., D.R. Katti, and R. Dash, S*ynthesis and characterization of a novel chitosan/montmorillonite/hydroxyapatite nanocomposite for bone tissue engineering.* Biomedical Materials, 2008. 3**(**3): p. 034122.
98. Wang, M., et al., M*anufacture and evaluation of bioactive and biodegradable materials and scaffolds for tissue engineering.* Journal of materials science. Materials in medicine, 2001. 1**2(**10-12): p. 855-860.
99. Fujii, S., et al., H*ydroxyapatite Nanoparticles as Particulate Emulsifier: Fabrication of Hydroxyapatite-Coated Biodegradable Microspheres.* Langmuir, 2009. 2**5(**17): p. 9759-9766.
100. Zhang, X., et al., T*hermal and crystallization studies of nano-hydroxyapatite reinforced polyamide 66 biocomposites.* Polymer Degradation and Stability, 2006. 9**1(**5): p. 1202-1207.
101. Kaur, J. and M.L. Shofner, S*urface Area Effects in Hydroxyapatite/Poly(ε-caprolactone) Nanocomposites.* Macromolecular Chemistry and Physics, 2009. 2**10(**8): p. 677-688.
102. Yoshimura, M., H. Suda, and K. Okamoto, H*ydrothermal synthesis of biocompatible whiskers.* Journal of materials science, 1994. 2**9:** p. 3399-3402.
103. Hong Z, Q.X., Sun J, Deng M, Chen X, Jing X, G*rafting polymerization of L-lactide on the surface of hydroxyapatite nano-crystals.* Polymer, 2004. 4**5:** p. 6699-6706.
104. Li, Y., F. Kong, and W. Weng, P*reparation and characterization of novel biphasic calcium phosphate powders (α-TCP/HA) derived from carbonated amorphous calcium phosphates.* Journal of Biomedical Materials Research Part B: Applied Biomaterials, 2009. 8**9B(**2): p. 508-517.
105. Moharram, M.A. and M.A. Allam, A*pplication of Fourier transform infrared spectroscopy to study the interactions of poly(acrylic acid) and mixtures of*

poly(acrylic acid) and polyacrylamide with bone powders and hydroxyapatites. Journal of Applied Polymer Science, 2007. 1**05(**6): p. 3228-3234.

106. Koutsopoulos, S., S*ynthesis and characterization of hydroxyapatite crystals: a review study on the analytical methods.* Journal of Biomedical Materials Research Part B: Applied Biomaterials, 2002. 6**2(**4): p. 600-612.
107. Konradi, R. and J. Rühe, I*nteraction of Poly(methacrylic acid) Brushes with Metal Ions: An Infrared Investigation.* Macromolecules, 2004. 3**7(**18): p. 6954-6961.
108. Wang, X.M., et al., I*n Situ Synthesis of PVA-PAA-HA Interpenetrating Composite Hydrogel.* Key Engineering Materials, 2006. 3**09-311:** p. 1165-1168.
109. A.S.T.M. card file No.9-432
110. Cullity, B. D.; Stock, S.R. Elements of X-ray Diffraction. Prentice Hall. 2001
111. Bigi, A., et al., M*icrostructural investigation of hydroxyapatite?polyelectrolyte composites.* Journal of Materials Chemistry, 2004. 1**4(**2): p. 274.
112. Beecroft, L.L. and C.K. Ober, N*anocomposite materials for optical applications.* Chemistry of Materials, 1997. 9**(**6): p. 1302-1317.
113. Bockstaller, M.R., R.A. Mickiewicz, and E.L. Thomas, B*lock copolymer nanocomposites: Perspectives for tailored functional materials.* Advanced Materials, 2005. 1**7(**11): p. 1331-1349.
114. Gangopadhyay, R. and A. De, C*onducting polymer nanocomposites: A brief overview.* Chemistry of Materials, 2000. 1**2(**3): p. 608-622.
115. Hammond, P.T., F*orm and function in multilayer assembly: New applications at the nanoscale.* Advanced Materials, 2004. 1**6(**15): p. 1271-1293.
116. Rittigstein, P., et al., M*odel polymer nanocomposites provide an understanding of confinement effects in real nanocomposites.* Nature Materials, 2007. 6**(**4): p. 278-282.
117. Schmidt, G. and M.M. Malwitz, P*roperties of polymer-nanoparticle composites.* Current Opinion in Colloid & Interface Science, 2003. 8**(**1): p. 103-108.
118. Crosby, A.J. and J.Y. Lee, P*olymer nanocomposites: The "nano" effect on mechanical properties.* Polymer Reviews, 2007. 4**7(**2): p. 217-229.

119. Xie, X.L., Y.W. Mai, and X.P. Zhou, D*ispersion and alignment of carbon nanotubes in polymer matrix: A review.* Materials Science & Engineering R-Reports, 2005. 4**9(**4): p. 89-112.

120. Zanetti, M., S. Lomakin, and G. Camino, P*olymer layered silicate nanocomposites.* Macromolecular Materials and Engineering, 2000. 2**79(**6): p. 1-9.

121. Bartholome, C., et al., N*itroxide-mediated polymerizations from silica nanoparticle surfaces: "Graft from" polymerization of styrene using a triethoxysilyl-terminated alkoxyamine initiator.* Macromolecules, 2003. 3**6(**21): p. 7946-7952.

122. Burke, N.A.D., H.D.H. Stover, and F.P. Dawson, M*agnetic nanocomposites: Preparation and characterization of polymer-coated iron nanoparticles.* Chemistry of Materials, 2002. 1**4(**11): p. 4752-4761.

123. Carrot, G., et al., S*urface-initiated ring-opening polymerization: A versatile method for nanoparticle ordering.* Macromolecules, 2002. 3**5(**22): p. 8400-8404.

124. Kong, H., C. Gao, and D.Y. Yan, F*unctionalization of multiwalled carbon nanotubes by atom transfer radical polymerization and defunctionalization of the products.* Macromolecules, 2004. 3**7(**11): p. 4022-4030.

125. Li, C., et al., A *versatile method to prepare RAFT agent anchored substrates and the preparation of PMMA grafted nanoparticles.* Macromolecules, 2006. 3**9(**9): p. 3175-3183.

126. Li, C.Z. and B.C. Benicewicz, S*ynthesis of well-defined polymer brushes grafted onto silica nanoparticles via surface reversible addition-fragmentation chain transfer polymerization.* Macromolecules, 2005. 3**8(**14): p. 5929-5936.

127. Qin, S.H., et al., P*olymer brushes on single-walled carbon nanotubes by atom transfer radical polymerization of n-butyl methacrylate.* Journal of the American Chemical Society, 2004. 1**26(**1): p. 170-176.

128. Raula, J., et al., S*ynthesis of gold nanoparticles grafted with a thermoresponsive polymer by surface-induced reversible-addition-fragmentation chain-transfer polymerization.* Langmuir, 2003. 1**9(**8): p. 3499-3504.

129. Shan, J., et al., A*mphiphilic gold nanoparticles grafted with poly(N-isopropylacrylamide) and polystyrene.* Macromolecules, 2005. 3**8(**7): p. 2918-2926.

130. Tchoul, M.N., et al., A*ssemblies of Titanium Dioxide-Polystyrene Hybrid Nanoparticles for Dielectric Applications.* Chemistry of Materials, 2010. 2**2(**5): p. 1749-1759.

131. Chen, G.X., et al., C*ontrolled functionalization of multiwalled carbon nanotubes with various molecular-weight poly(L-lactic acid).* Journal of Physical Chemistry B, 2005. 1**09(**47): p. 22237-22243.

132. Liu, X.H. and Q.J. Wu, P*P/clay nanocomposites prepared by grafting-melt intercalation.* Polymer, 2001. 4**2(**25): p. 10013-10019.

133. Yang, B.X., et al., M*echanical reinforcement of polyethylene using polyethylene-grafted multiwalled carbon nanotubes.* Advanced Functional Materials, 2007. 1**7(**13): p. 2062-2069.

134. Kim, H.S., et al., T*hermal and electrical properties of poly(L-lactide)-graft-multiwalled carbon nanotube composites.* European Polymer Journal, 2007. 4**3(**5): p. 1729-1735.

135. Lee, H.J., et al., T*he effect of surface-modified nano-hydroxyapatite on biocompatibility of poly(epsilon-caprolactone)/hydroxyapatite nanocomposites.* European Polymer Journal, 2007. 4**3(**5): p. 1602-1608.

136. Goffin, A.L., et al., P*oly(epsilon-caprolactone) based nanocomposites reinforced by surface-grafted cellulose nanowhiskers via extrusion processing: Morphology, rheology, and thermo-mechanical properties.* Polymer, 2011. 5**2(**7): p. 1532-1538.

137. Akcora, P., et al., A*nisotropic self-assembly of spherical polymer-grafted nanoparticles.* Nature Materials, 2009. 8**(**4): p. 354-U121.

138. Chevigny, C., et al., P*olymer-Grafted-Nanoparticles Nanocomposites: Dispersion, Grafted Chain Conformation, and Rheological Behavior.* Macromolecules, 2011. 4**4(**1): p. 122-133.

139. Geoghegan, M., et al., A *neutron reflectometry study of polystyrene network interfaces.* European Physical Journal B, 1998. 3**(**1): p. 83-96.

140. Corbierre, M.K., et al., G*old nanoparticle/polymer nanocomposites: Dispersion of nanoparticles as a function of capping agent molecular weight and grafting density.* Langmuir, 2005. 2**1(**13): p. 6063-6072.

141. Lan, Q., L.F. Francis, and F.S. Bates, S*ilica nanoparticle dispersions in homopolymer versus block copolymer.* Journal of Polymer Science Part B-Polymer Physics, 2007. 4**5(**16): p. 2284-2299.

142. Xu, C., et al., D*ispersion of polymer-grafted magnetic nanoparticles in homopolymers and block copolymers.* Polymer, 2008. 4**9(**16): p. 3568-3577.

143. Xu, J.J., et al., M*orphology and interactions of polymer brush-coated spheres in a polymer matrix.* Journal of Polymer Science Part B-Polymer Physics, 2006. 4**4(**19): p. 2811-2820.

144. Srivastava, S., P. Agarwal, and L.A. Archer, T*ethered Nanoparticle-Polymer Composites: Phase Stability and Curvature.* Langmuir, 2012. 2**8(**15): p. 6276-6281.

145. Smith, G.D. and D. Bedrov, D*ispersing Nanoparticles in a Polymer Matrix: Are Long, Dense Polymer Tethers Really Necessary?* Langmuir, 2009. 2**5(**19): p. 11239-11243.

146. Jeon, K., et al., R*ole of Matrix Crystallinity in Carbon Nanotube Dispersion and Electrical Conductivity of iPP-Based Nanocomposites.* Journal of Polymer Science Part B-Polymer Physics, 2010. 4**8(**19): p. 2084-2096.

147. Tjong, S.C., G.D. Liang, and S.P. Bao, E*ffects of crystallization on dispersion of carbon nanofibers and electrical properties of polymer nanocomposites.* Polymer Engineering & Science, 2008. 4**8(**1): p. 177-183.

148. Morin, A. and A. Dufresne, N*anocomposites of chitin whiskers from Riftia tubes and poly(caprolactone).* Macromolecules, 2002. 3**5(**6): p. 2190-2199.

149. Grady, B.P., et al., N*ucleation of polypropylene crystallization by single-walled carbon nanotubes.* Journal of Physical Chemistry B, 2002. 1**06(**23): p. 5852-5858.

150. Kalaitzidou, K., et al., T*he nucleating effect of exfoliated graphite nanoplatelets and their influence on the crystal structure and electrical conductivity of polypropylene nanocomposites.* Journal of Materials Science, 2008. 4**3(**8): p. 2895-2907.

151. Priya, L. and J.P. Jog, P*olymorphism in intercalated poly(vinylidene fluoride)/clay nanocomposites.* Journal of Applied Polymer Science, 2003. 8**9(**8): p. 2036-2040.
152. Peng, Q.Y., et al., T*he preparation of PVDF/clay nanocomposites and the investigation of their tribological properties.* Wear, 2009. 2**66(**7-8): p. 713-720.
153. Zheng, J.R., R.W. Siegel, and C.G. Toney, P*olymer crystalline structure and morphology changes in nylon-6/ZnO nanocomposites.* Journal of Polymer Science Part B-Polymer Physics, 2003. 4**1(**10): p. 1033-1050.
154. Swain, S.K. and A.I. Isayev, P*A6/clay nanocomposites by continuous sonication process.* Journal of Applied Polymer Science, 2009. 1**14(**4): p. 2378-2387.
155. Kaur, J. and M.L. Shofner, S*urface area effects in hydroxyapatite/poly(e-caprolactone) nanocomposites.* Macromolecular Chemistry and Physics, 2009. 2**10(**8): p. 677-688.
156. Hu, X.L., et al., T*he effect of matrix morphology on nanocomposite properties.* Polymer, 2010. 5**1(**3): p. 748-754.
157. Kaur, J., et al., E*nabling Nanoparticle Networking in Semi-Crystalline Polymer Matrices.* submitted.
158. Vidotto, G., D. Levy, and A.J. Kovacs, C*RYSTALLIZATION AND FUSION OF SELF-SEEDING POLYMERS .I. POLY-1-BUTENE POLYETHYLENE AND POLYOXYETHYLENE OF HIGH MOLECULAR WEIGHT.* Kolloid-Zeitschrift and Zeitschrift Fur Polymere, 1969. 2**30(**2): p. 289-&.
159. Schubnell, M., "Measurement of Thin Films in Shear by DMA", Mettler Toledo Thermal Analysis User Com, 2009, 29. (available online at http://us.mt.com/us/en/home/supportive_content/matchar_apps/MatChar_UC293.html)
160. Cullity, B. D.; Stock, S.R. Elements of X-ray Diffraction. Prentice Hall. 2001
161. Strawhecker, K.E. and E. Manias, C*rystallization Behavior of Poly(ethylene oxide) in the Presence of Na + Montmorillonite Fillers.* Chemistry of Materials, 2003. 1**5(**4): p. 844-849.
162. Chatterjee, T., A.T. Lorenzo, and R. Krishnamoorti, P*oly(ethylene oxide) crystallization in single walled carbon nanotube based nanocomposites: Kinetics and structural consequences.* Polymer, 2011. 5**2(**21): p. 4938-4946.

163. Zhang, X. and L.S. Loo, S*tudy of Glass Transition and Reinforcement Mechanism in Polymer/Layered Silicate Nanocomposites.* Macromolecules, 2009. 4**2(**14): p. 5196-5207.
164. Rao and J.M. Pochan, M*echanics of Polymer−Clay Nanocomposites.* Macromolecules, 2006. 4**0(**2): p. 290-296.
165. Lu, J., T. Wang, and L.T. Drzal, P*reparation and properties of microfibrillated cellulose polyvinyl alcohol composite materials.* Composites Part a-Applied Science and Manufacturing, 2008. 3**9(**5): p. 738-746.
166. Shanmuganathan, K., et al., B*io-inspired mechanically-adaptive nanocomposites derived from cotton cellulose whiskers.* Journal of Materials Chemistry, 2010. 2**0(**1): p. 180-186.
167. Soon, K., et al., M*orphology, barrier, and mechanical properties of biaxially deformed poly(ethylene terephthalate)-mica nanocomposites.* Polymer Engineering and Science, 2012. 5**2(**3): p. 532-548.
168. Krishnamoorti, R., S*trategies for dispersing nanoparticles in polymers.* MRS bulletin, 2007. 3**2:** p. 341-347.
169. Lagaly, G., I*ntroduction: from clay mineral-polymer interactions to clay mineral-polymer nanocomposites.* Applied Clay Science, 1999. 1**5:** p. 1-9.
170. Giannelis, E., P*olymer layered silicate nanocomposites.* Advanced materials, 1996. 8**(**1): p. 29-35.
171. Sinha Ray, S. and M. Okamoto, P*olymer/layered silicate nanocomposites: a review from preparation to processing.* Progress in Polymer Science, 2003. 2**8(**11): p. 1539-1641.
172. Kimura, T., et al., P*olymer composites of carbon nanotubes aligned by a magnetic field.* Advanced Materials, 2002. 1**4(**19): p. 1380-1383.
173. Garmestani, H., et al., P*olymer-Mediated Alignment of Carbon Nanotubes under High Magnetic Fields.* Advanced Materials, 2003. 1**5(**22): p. 1918-1921.
174. Xie, X., Y. Mai, and X. Zhou, D*ispersion and alignment of carbon nanotubes in polymer matrix: A review.* Materials Science and Engineering: R: Reports, 2005. 4**9(**4): p. 89-112.

175. Breuer, O. and U. Sundararaj, B*ig returns from small fibers: A review of polymer/carbon nanotube composites.* Polymer Composites, 2004. 2**5(**6): p. 630-645.

176. Kim, I.T., A. Tannenbaum, and R. Tannenbaum, A*nisotropic conductivity of magnetic carbon nanotubes embedded in epoxy matrices.* Carbon, 2011. 4**9(**1): p. 54-61.

177. Gusev, A.A. and M.G. Rozman, N*umerical search for morphologies providing ultra high elastic stiffness in filled rubbers.* Computational and Theoretical Polymer Science, 1999. 9**(**3-4): p. 335-337.

178. Sheng, N., et al., M*ultiscale micromechanical modeling of polymer/clay nanocomposites and the effective clay particle.* Polymer, 2004. 4**5(**2): p. 487-506.

179. Sen, R., et al., P*reparation of Single-Walled Carbon Nanotube Reinforced Polystyrene and Polyurethane Nanofibers and Membranes by Electrospinning.* Nano Letters, 2004. 4**(**3): p. 459-464.

180. Ko, F., et al., E*lectrospinning of Continuous Carbon Nanotube-Filled Nanofiber Yarns.* Advanced Materials, 2003. 1**5(**14): p. 1161-1165.

181. Choi, E.S., et al., E*nhancement of thermal and electrical properties of carbon nanotube polymer composites by magnetic field processing.* Journal of Applied Physics, 2003. 9**4(**9): p. 6034.

182. Ha, Y.-H., et al., A*n Orientationally Ordered Hierarchical Exfoliated Clay−Block Copolymer Nanocomposite.* Macromolecules, 2005. 3**8(**12): p. 5170-5179.

183. Motro R "Tensegrity Structure Systems For The Future" Kogan Page Science, London, 2003

184. Lasagni, F., et al., N*ano-characterization of Cast Structures by FIB-Tomography.* Advanced Engineering Materials, 2008. 1**0(**1-2): p. 62-66.

185. McGrouther, D. and P.R. Munroe, I*maging and analysis of 3-D structure using a dual beam FIB.* Microsc Res Tech, 2007. 7**0(**3): p. 186-94.

186. Kawaguchi, S., et al., A*queous solution properties of oligo-and poly (ethylene oxide) by static light scattering and intrinsic viscosity.* Polymer, 1997. 3**9(**12): p. 2885-2891.

187. Samuels, R. J. "Structured Polymer Properties: The Identification, Interpretation, and Application of Crystalline Polymer Structure" John Wiley & Sons, New York, 1974.

188. Zhao, X. and L. Ye, S*tructure and properties of highly oriented polyoxymethylene produced by hot stretching.* Materials Science and Engineering: A, 2011. 5**28(**13-14): p. 4585-4591.

189. Taraiya, A.K., et al., P*roduction and properties of highly oriented polyoxymethylene by die-drawing.* Journal of Applied Polymer Science, 2003. 8**8(**5): p. 1268-1278.

190. Kelarakis, A., et al., R*elationship between structure and dynamic mechanical properties of a carbon nanofiber reinforced elastomeric nanocomposite.* Polymer, 2006. 4**7(**19): p. 6797-6807.